Non-Destructively Detecting Spinodal Decomposition at a Distance

Towards Developing Gigahertz Ultrasonics for In-Vessel Inspection

by

Saleem AbdulFattah Ahmed Al Dajani

S.B. in Physics and in Chemical-Biological Engineering, MIT (2019)

Submitted to the Department of Nuclear Science and Engineering
in partial fulfillment of the requirements for the degree of

Master of Science in Nuclear Science and Engineering

at the

MASSACHUSETTS INSTITUTE OF TECHNOLOGY

February 2020

© Massachusetts Institute of Technology 2020. All rights reserved.

Author . . . . **Signature redacted** . . . .
Department of Nuclear Science and Engineering
October 23, 2019

Certified by . . . . **Signature redacted** . . . .
Michael P. Short
Class of '42 Associate Professor of Nuclear Science and Engineering
Thesis Supervisor

Certified by . . . . **Signature redacted** . . . .
C. Cem Tasan
Associate Professor of Metallurgy
Thesis Reader

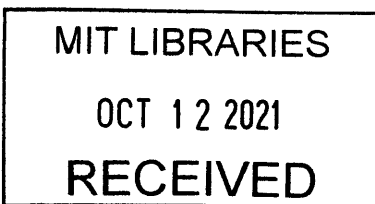Accepted by . . . . . . **Signature redacted** . . . .
Ju Li
Battelle Energy Alliance Professor of Nuclear Science and Engineering
and Professor of Materials Science and Engineering
Chair, Department Committee on Graduate Students

Non-Destructively Detecting Spinodal Decomposition at a Distance

Towards Developing Gigahertz Ultrasonics for In-Vessel Inspection

by

Saleem AbdulFattah Ahmed Al Dajani
Submitted to the Department of Nuclear Science and Engineering
on October 23, 2019, in partial fulfillment of the
requirements for the degree of
Master of Science in Nuclear Science and Engineering

Abstract

Given the existential climate crisis faced by mankind and the world, the lifetime and sustainability of nuclear reactors as a carbon-free source of renewable energy depend on the susceptibility of their structural components to environmental degradation. In particular, critical components for light water reactors (LWRs) evolve over decades in service, losing ductility and toughness due to thermal and irradiation aging. Techniques to monitor their health cannot be easily applied in the field due to their destructive, expensive, or immobile nature. Thus, non-destructive evaluation (NDE) methods are sought to monitor and evaluate the health of major LWR components such as core barrels, steam generator tubes, or primary coolant pipes and are often required by policy, such as NRC policy 10-CFR-50.65. Here we demonstrate the use of gigahertz, non-contact ultrasonics to gauge the state of cast austenitic stainless steels (CASS), used in some of the largest components in LWR primary systems. We do so by linking changes in their surface acoustic wave (SAW) characteristics using transient grating spectroscopy (TGS) to transmission electron microscopy (TEM)-verified evidence of spinodal decomposition and G-phase precipitation. In this thesis, thermal aging is shown to induce SAW peak splitting in spinodally decomposed CASS alloys, correlated strongly with lowered toughness and decreased ductility. Furthermore, statistical testing on the number of SAW peak splits observed show that the second SAW peak significantly appears more frequently and is significantly different in frequency in comparison to counts and frequencies measured in unaged specimens. The ability of this technique to non-destructively detect microstructural degradation at a distance in a predictive manner in the case of CASS motivates extending gigahertz ultrasonics to detect other LWR material degradation modes as an in-vessel inspection technique, such as reactor pressure vessel (RPV) embrittlement. This allows for the greater use of NDE techniques for confident monitoring of LWR structural material health to 80 years and beyond, saving costs by minimizing structural replacements until needed and maximizing energy production by preventing early decommission until necessary.

Thesis Supervisor: Michael P. Short
Title: Class of '42 Associate Professor of Nuclear Science and Engineering

Thesis Reader: C. Cem Tasan
Title: Associate Professor of Metallurgy

Acknowledgments

I always wondered what Einstein meant by standing on the shoulder of giants. Here is a snapshot of what that looked like in my humble experience:

I write this with tears in my eyes, the good kind and the not-so-good kind. Science can be hard. Definitely harder than I ever thought, even when studying hard-ness, haha. Mike, thank you for empowering me when I needed that echo of belief in myself—your support, your mentorship, your leading-by-example, I could not have had such a wonderful experience doing this weird five year thing (never fully understood how it worked out and what my student status was throughout or what my transcript will look like). I was once given advice on what it takes to become a professor, and my friend Wael was telling me about this famous topology professor at MIT who embodied and became "topology" throughout his career. From my experience, you have definitely become "nuclear materials" at such an early stage in your career (for example, by revolutionizing the core of nuclear materials characterization!) and I

5

hope your kindness and compassion only and always come in handy moving forward. Cem, thanks for offering your time and support throughout this thesis, and thanks for pushing me to my limit like that one time you put me on the spot and I didn't know the answer. Our interactions really allowed me to grow as a scientist and for that I will always be grateful. Cody, you stuck it out for us all whenever we needed anything at all, even when you were defending your thesis and moving, and I hope you always know this project would not have been possible without your effort over the years in general and, although we only overlapped for one year, your effort with me as well in particular. You have a unique ability to constructively add to any scientific discussion I've witnessed you partake in—what a role model for me to have observed and worked with early in my scientific career. Ben, I definitely learned a lot from working with you whether that was running experiments in the lab, TGS Tuesdays with Mike (and Cody sometimes!), or even when we were writing that paper together. Sara, thanks for helping me with that grant and your input in general on my group meeting presentation, which was really the core of my thesis amidst digestion—our discussions on the T back from Raj's class at MGH were definitely good times and I really learned a lot from you! I would be really happy if any of us are yet to work together in the future, you are all super smart and nice people and, sincerely, I am *so* lucky to have had the opportunity to learn from you all during this Short time. (pun intended) Brandy and Heather, you get a special one, thank you for making NSE feel like home. Thank you Marina and the NSE Comm Lab fellows. :-)

Taiteh Mariam, that blood transfusion took you away from us too early for me to ever meet you. It is difficult for me to get over that. I hope you know that I am now advancing our understanding of the most fundamental units of life: cells and nuclei. What motivates me everyday to do so is the fact that this kind of understanding could have saved your life, could have given me the opportunity to learn from your experiences in life, your experiences picking oranges out of that beautiful orange orchard in Bayt Dajan. I plan to one day grow my own orchard of oranges in your name as a running charity and please hold me to it when we next cross paths. I know you never got over losing Ammo Omar when he was just twenty and Baba tells me

about how much of an awesome older brother to him he was. He tells me about how routine that medical procedure was and that by the time that he got to the US for his treatment, it was too late. Omar fulfilled that self-fulling prophecy by becoming that Omar to me as your eldest son was to my father. I know this does not reduce your devastation but I know if you were alive it may have made it easier for you to deal with it. Some things in life are just so difficult to accept. They say a mother's prayers go a long way, and I just know your prayers were heard somewhere, somehow and came together as who we all are now—please keep me in your prayers, because some things in life are just timeless and eternal—just like your presence in my mind, heart, and soul.

Taiteh Waleedah, you witnessed my birth in Wheat Ridge, Colorado. I wish you were around to witness my graduation walk. You never had the chance to have a college education due to the dispora and your early marriage. I wish you knew where I ended up. When you saw my tiny legs as an infant, you reassured my mother that I would one day roam the Earth saying "La tsheeli ham yumma rah yohotelik hal eqal wa yehki ya ard eshtadi ma hada addi (Literal Translation: Don't worry my daughter, one day he will put on his camel rope and tell the Earth to strengthen itself because nobody can take on my size.) Satirically, I officially grew up to be the shortest of my siblings, but the height of my accomplishments, thus far, speak on their own. Onwards and upwards, Grandma. When you were on your deathbed, I vividly remember being lucky enough to fly in from the US that dark night in '01. I recited Surat Al-Balad (The City) to you and I often think about its rich meanings. In particular, the fact that humans came to be in continuous ardor and adversity, but we need to fight through it anyway with all of our senses and blessings. I hope you are watching upon me as you rest in peace. I hope you are proud of what I have become and will be.

Jeddo Saleem, the only reason I am opting into the option of walking again this year for the masters degree is the hope of seeing you there. You inspire me everyday and I would be nothing without you. When I told you about my experience with spaceships, rockets, and launch pads at SpaceX, you asked me *one* question that

always makes me ponder: "do they trust you?"—reminding me the importance of establishing trust and gaining the respect of my colleagues throughout my academic career. Your mantras have also taught me to be grateful to whoever educates me, starting from learning a single letter. These lessons and the plethora that I have learned from interacting with you or through my mother's stories about her upbringing with you had been proven to me valuable while writing this thesis as well as in my everyday life. I know any acknowledgement cannot do you justice for everything that I am blessed with thanks to you, but I hope you get to know that the entirety of this work is dedicated to you. When you attended my birth in the US as a dual citizen, you named me "Abu Ra'ad," meaning the Father of Thunder. I hope to be fitting of that label one day and always speak up let my actions speaker louder than my words towards what (I believe) is right, and to have the right people to correct my course when I may go astray.

Jeddo Ahmed, I was never lucky enough to meet you. I did see your picture and can imagine your smile. In third grade, I was once lying on my side and have my soup and my brother told me that you used to sit like that. I guess it runs in our blood. I know it was tough for you to find a new home after what you went through, but I also hope you know that your sacrifices throughout taught my father how to live happily. I always think about hard it was for my father to lose you in his early twenties, but you a hell of a job in making a great man. It really makes us tough for me to fill the big shoes you raised and I will always strive to become that and beyond. I know it was tough for you to find a new after what you went through, but you made it possible for me to find multiple wherever I go. And as the old fart in Naruto taught me very early on in my life: 'home is where people are thinking of you.' I hope you always find me in your best thoughts and you just watch. I will create that lasting home for us whether they like or not, we belong. We belong. We belong.

Mama, Baba, I know I have been far away from you for so long and it can be tough for me too. First and foremost, I hope you believe in the decisions that I had to take myself and have faith that I will be able to make the right decisions in the future. I want you to know that although the road may have been bumpy, I have truly found

myself at home here at MIT thanks to your infinite support. Since I was young, I would get perfect scores at school and you would always tell me that perfect scores are not sufficient; that I needed to go beyond what I learned in the classroom. Little did I know that the habits that you instilled in me throughout my life would end me up at MIT for a journey of my own back where it all started. When I was in second grade and they made me do third grade work while I worked my up to six grade level reading, you taught me the value of not rushing things by skipping grades and, more importantly, how to take my time, do things right, and not skip any steps along the way. I hope I always have the strength to be patient enough for good things yet to come, and your support along every step of the way has been monumental to my overall growth as a human above all, and as a scientist and young professional. After my first day of classes here, I came home in tears and seriously opened a common app for transfer applications, feeling out of place in a new daunting world. Prevailing over the many obstacles that I was faced with would have been null without your belief in my ability to bounce back every single time I came close to losing balance, and I hope you can take at a look at me now and take pride in your parenthood for empowering me throughout my journey of completing my third consecutive degree program at MIT.

Mama, You are really a role model in everything you do and I will always appreciate that no matter where I end up in the natural lottery of life. I know you always wanted me to become a neurosurgeon, but because of my shaky hands I always knew that not the right profession for me. That is what got me into radiation oncology and working with Raj because what is cooler than neurosurgery is radiation therapy. Why intervene if you could just blast that stuff with protons. In some ways, my plans for studies do and will always satisfy your wishes after all as I will not let them go otherwise. I will always make you proud to be my mother, seeing you smile and send me all those weird emojis on WhatsApp are really what make it all worth it, haha, you get what I mean. Or even when we do our kindergarden secret even at 25, or when you blow me those plushy kisses through the phone. I wish you can see that now and in the future. I love you and miss you more every single day that

I am away from you. I am blessed to be your son, and more blessed to have been raised in your lap and between your arms. I think I called you before almost every test at MIT, and your prayers and support have always empowered through this hard stuff—I never want to lose that. Baba, often it is about how hard you can get hit and keep moving forward indeed, but also about how hard you can hit. Attending your doctoral ceremony at MIT in '02 and my vivid memory of taking pictures with the MIT seal in lobby 7 often recurs to me in my thoughts. I wonder if that is the reason that I was attracted to this place. I do question whether that warrants that I fit in, that I belong to this place. I do want to tell you at the very it gives me a sense of belonging at home and relatable experience that I can rely on when I think about you now and in the future. I don't say this as often as I should, but I love you Baba. I love you more than you will ever know and more than I can describe in words.

Omar, You are the best eldest brother a human on this planet could ever ask for. Thanks for letting me learn the lessons the hard way. Ahmed, I know we've been saying let's talk every week since I arrived in the US and even though that never happened, I don't think a day has passed that you have not crossed my mind. I even have a playlist called "ahmed" that I use when I run, and you know how much running helps me get through stuff, like writing this thesis. Mohammed, I am glad you were able to find role models more closely aligned with your goals in life during your time at MIT. I cannot even imagine having a better experience through this place without you joining the journey. It has been such a blessing to have brothers at MIT, and I found it so funny when I started as an Educational Counselor to do MIT interviews that the regional coordinator still couldn't tell the difference between our voices. Basheer, Don't let the tricks of the mind trick the heart, and, oh yeah, Corazon. <3 You taught me more than you know, and you always remind me of what is important to me. You will do great no matter what you decide to do, just please don't do as I do and enjoy the ride—you'll miss it when it's all over. Don't even do as I say and follow your pure heart. Lubna and Reem, Thanks for being the sisters that I never had. Your support and kind visits as in-laws while writing this thesis have really been delightful and motivating for me to become a better version

of myself. Look at me, I am blessed to have the best siblings in the world.

Miss. Wendy, I would not be where I am without you crushing my ego (for the better) time and time again. I carry your lessons from my early childhood in your classes with me every single day. And same goes to you, Miss. Maha, people still don't believe that this all started with the common application you both made us fill when we were in sixth grade—and that charity sale when I was Schrodinger's cat in that box, of course, one of my extracurricular activities. Dr. Sally and Abu Rami, Words cannot describe how empowering my relationship with you two has been instrumental to the growth of my character over the years. And that goes beyond my DAS experience, which could not have been possible without your insanely diligent efforts over the years. Only God knows how much I miss you and how careful I am about not bothering you through your busy lives. I often think to myself what would Dr. Sally and Abo Rami tell me if I asked them about this or that. You four are parents of so many successful people beyond your family and I aspire to accomplish even the smallest fractions of what you've accomplished in your humble lifetimes.
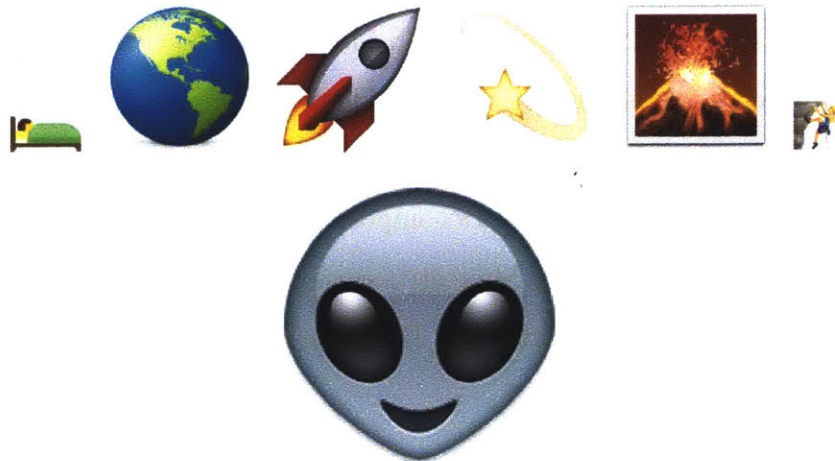
This one is for you, the hidden soldier in my life, you know who you are: Thank you for being my best friend throughout thick and thin. Thank you for playing with lasers with me. 'Member that day you helped me hold it together and run through TGS from 5pm to 5am? I 'member, indeed. You knew I thought that I messed up the experiment and watched me contemplate my existence and all my life decisions. For a split-second, I even considered giving up and dropping out of the program. Then, you reminded me that there was no panicking allowed. We have gone a long way and we're here at the finish line! May distance never allow us to drift apart. It was truly the '19 to fly that we jinga to after all.

To those who have been close to me in the past and are currently not present in my life or those who I may have missed in this extraordinarily long acknowledgements section, I wish you the best always and would like to acknowledge that I would not be where I am today without the constructive experiences that we have had together. My heart goes out to all of you during these stressful times, and may we cross paths again in the future in ways that we have not imagined possible. I'd

also like to acknowledge the following people and organizations, who while I did not have time to write specifics, played a crucial role in getting me to this point in my scientific career and personal life, including but not limited to: Steve Jepeal, Moodera, Angie, Zweirlein, Kulik, Xiangnan, Alan, Tisdale, Ike, Mujid, Majd, Ali, Sherif, Yazeed, Emad, Jodutt (Brojo), Boon, Bakr, Abdelsaboor, Sarah, Aalyah, Raghad, Dr. Annas, Abdullah (Alsaeed), Fozan, Abubakar, Erik, Yousef, Mahmoud, Aleena, Wael, Hasan, Yen-Jie, Aviv, SpaceX, Mawhiba, Douglas Woodall, Cameron Guthrie, Paul Bonness, John Muratore, Tom McClelland, JPL, SAEV, CERN, Dr. Steve Guertin, Dr. Ibrahim Almojel, Fil, Alice, Alex Dalzell, Ali—the list goes on.

Oh, and I almost forgot. Saleem, thank you for learning how to love yourself, how to stand up for yourself and, more importantly, how to be yourself. In Arabic, your name can either mean pure or poisoned by snake venom (optimism to get better). You know the right definition to choose in context of what's toxic for you. You choose whether you want to avoid the toxicity altogether or become constructive enough to remove that toxicity yourself. Perhaps you are the convergence of both meanings, and maybe this is just jibber jabber. Never forget that it's people before problem sets. You are awesome, stay awesome, and keep doing awesome stuff. I probably have the longest acknowledgments and may even be the first to add emojis to a thesis.

A story starting from a land far, far away to deep space at JPL, SpaceX to leave Earth and nuclear to power through interstellar space. Then, from nuclear to nuclei to making humans interplanetary, all the way to Olympus Mons—per aspera ad astra.

Contents

List of Figures

18

20

List of Tables

Chapter 1

Introduction

"All processes that are stable we shall predict. All processes that are unstable we shall control."

—John von Neumann, 1950

For many utilities, extended operation of light water reactors (LWRs) beyond the 40-year original license period is critical for continued sustainable energy production. It is likely that 90% of reactors will seek life extensions up to and beyond 60 years. In these cases, the US Nuclear Regulatory Commission (NRC) must approve lifetime extensions for these reactor systems based on the reliability of the plant components to be assured throughout the current license and the extended period of time. Regardless of whether a lifetime extension is needed, the NRC maintenance rule, Title 10 of the Code of Federal Regulations Part 50.65, (10 CFR 50.65) dictates that an effective material aging management program must be implemented throughout the lifetime of the reactor [1]. This would involve the monitoring and evaluation of LWR materials by means of characterizing the aging and degradation of its structural components [2].
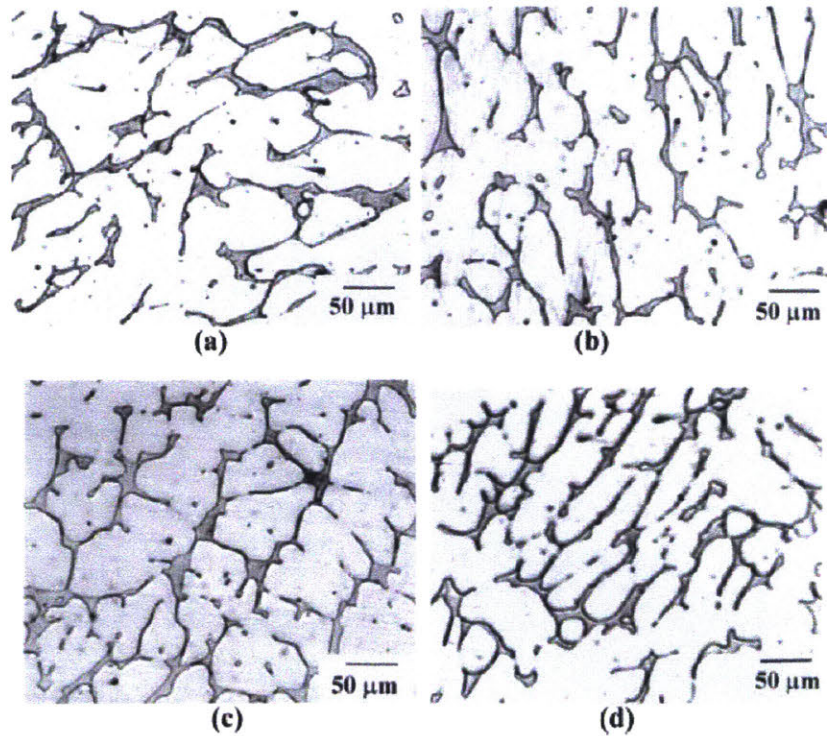
Figure 1-1: Microstructure of example CASS alloy, dark gray represents the ferrite phase and light gray represents the austenite phase; (a) unaged (b) aged for 6 months (c) aged for 12 months (d) aged for 18 months [4]

1.1 Why we need nondestructive techniques in nuclear materials science

In general, material degradation in nuclear reactor components is extremely complex. There are more than 25 different alloys used in LWR systems, and these materials respond differently to the harsh conditions of a nuclear reactor. [3] Cast Austenitic Stainless Steels (CASS) are a class of LWR structural materials widely used across many major, critical structural components. When the ductile to brittle transition temperature (DBTT) of CASS alloys that are thermally aged throughout the reactor lifetime approaches room temperature, they are considered unfit for service. [2]

However, it is extremely difficult to perform direct measurements of material aging and degradation in materials which have been subject to radiation, and to determine whether the damage was from irradiation, exposure to corrosive fluids, prolonged
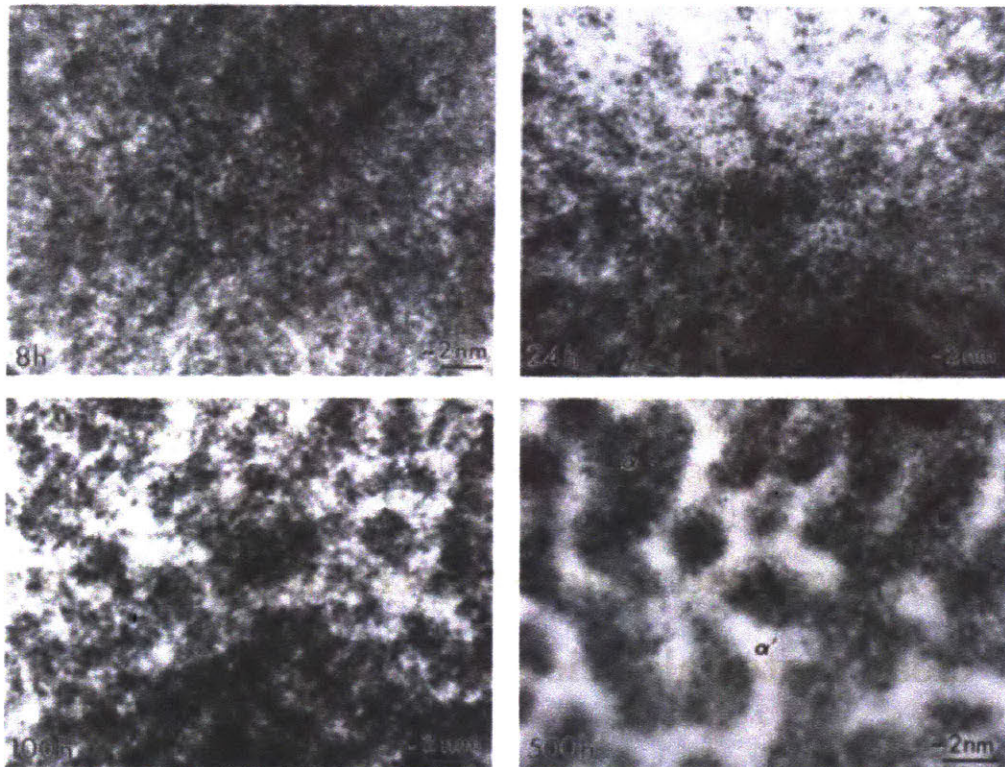
Figure 1-2: TEM nanostructure of example CASS alloy showing the evolution of the α'-phase morphology due to spinodal decomposition (a) aged for 8 hours (b) aged for 24 hours (c) aged for 100 hours (d) aged for 500 hours [5]

exposure to elevated temperature, and/or any other mode of environmental degradation. The most common methods used today to probe these radiation damage modes and degradation mechanisms involve measuring overall material properties at the macroscale, or focusing on small areas via destructive analysis. The link between the structure of environmentally degraded materials to changes in material properties is a largely unmet challenge for radiation materials science [6].

1.1.1 What can be accomplished with non-destructive techniques in nuclear materials science

Ideally, a theoretical framework would be used to guide an experimental approach to understanding the response to environmental degradation factors to bridge this gap, yet a fully described theoretical framework for radiation materials science has not been developed. [6] By conventional methods, radiation damage data is collected destructively and *ex situ*, which is typically time-consuming, expensive, and requires the study to be done with different samples. [7] This is the primary reason for the sparse data points discussed previously in radiation damage studies. The added benefit of a rapid, *in situ* technique that is also non-destructive is an overall decrease in time for experimental campaigns. Given the non-destructive nature of TGS, the same studies can be performed by averaging over multiple spots on the same sample across all analyses for detection of radiation damage. For sustainable operations and maintenance of LWRs, the potential to decrease experimental campaigns from months/years (restricted to maintenance times for LWRs) to days/weeks carries significant cost savings to LWR material assessments. [8] This also creates a need for Nuclear Regulatory Commission (NRC) regulatory policies that accept the results of TGS experiments and predictions to support the lifetime extension or early shutdown of LWR operations.

Therefore, the only viable way to rapidly bridge this gap is to quickly link easily measurable quantities, preferably in a non-destructive manner, to those of ultimate interest such as DBTT and Charpy impact energy. Recent studies have shown that the

28

sensitivity, repeatability, and predictability of transient grating spectroscopy (TGS) measurements represents a promising tool to potentially replace and/or complement existing characterization techniques [6,8–19] We propose to realize these gains in characterization by bypassing more traditional dose-structure-property relationships such as TEM, normally the hallmark of materials science, in favor of direct dose-property measurements supplemented by structural characterization for better understanding. Overall, the ability to monitor and evaluate the health of LWR structural materials as they degrade directly impacts reactor reliability, availability, and safe operations. The aging and degradation of these materials can be mitigated with continuous monitoring, as component replacements can be made when these failures occur. Even when failures are detected, it may not be economically feasible to make such replacements. Therefore, a complete understanding of materials aging and degradation processes is a major priority for the lifetime and sustainability of LWR systems [2].

1.2 Motivating LWR sustainability with nuclear materials policy

To address the issue of material degradation in LWRs in general, the NRC developed the Expert Panel Report on Proactive Materials Degradation Assessment (NUREG/CR-6923) to prevent materials degradation from impairing the integrity of reactor structural materials (including CASS), [2] and to identify where and when degradation can be expected to occur in the future. In conclusion of the directive, the NRC highlights the significance of transitioning from reactive management of materials degradation to proactive management, given that the interdependencies of the complex degradation mechanisms associated with thermal aging and radiation damage require a high level of experimental sophistication to be understood. Deploying rapid, non-destructive techniques such as TGS can be used to provide the information needed to manage LWR material degradation programs.

1.2.1 Extending LWR lifetimes to eighty years using giga-hertz ultrasonics as an in-vessel inspection technique

Considering the regulatory framework set forth by the NRC, performing TGS, a form of gigahertz ultrasonic techniques, on CASS materials is in line with the transition to proactive management of nuclear materials. The ability of TGS to detect thermal aging of CASS presents it as a reliable characterization method for the NRC needs and conclusions in NUREG/CR-6923. [2]

Practically, results from TGS measurements can be used to support requests for LWR lifetime extensions if the benefits outweigh the costs, i.e. it is predicted that the materials will last longer than the current license or the profits of operation can outweigh the costs of replacing the core barrel when degraded materials become a risk for LWR safety and operations. On the other hand, if the costs outweigh the benefits of continued operation, results from TGS measurements may offer significant cost savings on operations if an early shutdown is warranted by predicted early failure of CASS materials. With this unprecedented method of predictive insight into the lifetime of reactor structural materials and thus reactor lifetimes, the unique advantages of TGS as a non-contact, non-destructive evaluation technique can significantly contribute towards the greater sustainability of LWRs and any associated operations or maintenance—as addressed by NUREG/CR-6923.

1.3 Overview of thesis structure

The Introduction section discusses the motivation for and significance of non-destructive evaluation techniques in nuclear materials. The benefits and implications of TGS as a non-destructive technique is also discussed in context of LWR lifetime extensions and the framework of regulations put forth by the NRC on the management of nuclear materials degradation.

The Background section provides a literature review on the CASS alloys investigated in this study, their modes of degradation, and what materials properties are

critical to characterize in order to monitor and evaluate their health through the lifetime of the reactor. Current non-destructive evaluation techniques are evaluated and compared to select a suitable characterization tool to detect degradation in reactor structural materials. TGS is then explained in detail, and a review on recent literature on applications of TGS in radiation materials science is provided to support the feasibility of TGS as a tool for non-destructive evaluation of nuclear materials.

The Methods section provides a guide on the tools employed in this study, including methods completed with collaborators (addressed accordingly in each section). The section includes an overview of the steps undertaken to complete Charpy impact tests, microstructural characterization, micro and nanoindentation, and TGS measurements. Furthermore, the analysis algorithms, models, tools, and calculations used to process the raw data from experiments are also highlighted—and are also available online via the Short Lab GitHub repository. https://github.com/shortlab/SDajani-Thesis

The Results section provides an overview of the raw and processed data collected for this study, and highlights the key observations from the experiments conducted throughout the study. Charpy impact test results show decreasing Charpy impact energy with increased thermal aging. Microstructural characterization results confirm the presence of spinodal decomposition in thermally aged samples, as well as precipitations along the grain boundaries. Microindentation results show an increase in Vickers hardness of delta ferrite in comparison to austenite in thermally aged samples, and nanoindentation results show an increase in relative nanostiffness of delta ferrite along with changes in material properties at the interface between ferrite and austenite. Analyses on TGS measurements show a consistent trend of single surface acoustic wave (SAW) frequencies in non-aged samples, consistent with model calculations, with occasional double peaks observed due to illuminating two neighboring grains in the TGS spot (an infrequent occurrence). In addition, results from TGS also show a statistically significant appearance of a second SAW frequency in thermally aged samples that is significantly higher than any variations expected in model calculations.

The Discussion section aims to attribute the second SAW frequency to the microstructural degradation of CASS alloys due to thermal aging. The link between the direct (SEM, TEM, EDX) and indirect (Charpy, indentation) evidence is established in order to confirm that microstructural degradation via spinodal decomposition and nucleation and growth has occurred in thermally aged samples, and may be attributed to SAW frequencies measured via TGS for non-destructive detection of such degradation modes in structural nuclear materials. Ultimately, the statistical significance of this hypothesis is discussed in context of the most plausible competing hypothesis that attributes variations in SAW frequencies to random crystal orientation rather than differences in material properties due to degradation.

The Conclusion section provides a summary of the body of work, including an overview on the need for non-destructive evaluation techniques and the benefits that TGS may offer for nuclear materials proactive management programs, highlighting the main outcomes of this study on CASS alloys as an example for an application of this NDE tool. Based on the results of this study, the most vital directions of future work are suggested and discussed to consolidate the link between SAW peak splitting and microstructural degradation, including spinodal decomposition and nucleation and growth, and in order to extend TGS as a tool to monitor and evaluate other classes of materials in nuclear systems and beyond.

Chapter 2

Background

2.1   Cast Austenitic Stainless Steels (CASS) in Nuclear Light Water Reactor (LWR) Systems

CASS are a class of alloys primarily composed of iron (Fe), chromium (Cr), and nickel (Ni) in a duplex structure of austenite (γ) and meta-stable ferrite (δ) phases. [20–27] The grading standard for CASS alloys is based on the (i) chemical composition, determined by the amount of Fe, Cr, Ni, Mn, Si, and C, and (ii) microstructural constituents, determined by the volume fractions of γ and δ phases. [28–31] In nuclear reactors, CASS alloys are most commonly used due to the lower overall alloy content and relatively high Cr content. [32] Due to a lower overall alloy content in these duplex structures, these material systems are more cost-effective than super-austenite or super-ferrite counterparts because of their extensive, large-scale usage in LWR systems. [33] Furthermore, due to the relatively high Cr content in these alloys, these materials are highly resistant to corrosion and are therefore predominantly used for primary coolant piping, pump casings, valve bodies, and elbows of LWR systems [34].

However, the environmental degradation of CASS is a primary concern for LWR lifetime and sustainability due to their extensive usage in the structural components of the primary side of the reactor. [35] Among various compositions of CASS alloys, higher ferrite content is directly correlated to degradation (in the form of hardening

[wt%]	Fe	Cr	Ni	Mn	Mo	Si	Cu	Co	P	V
CF8	Bal	20.01	8.61	0.57	0.3	1.31	0.07	0.08	0.031	0.02
CF8M	Bal	20.77	10.16	0.95	2.51	0.85	0.39	0.16	0.023	0.02

Table 2.1: CF8 and CF8M CASS sample compositions in weight percent as received from EPRI castings, measured via quantitative analysis by inductively coupled plasma optical emission spectrometry at Dirats Laboratories [27, 47]

[ppm]	C	S	O	N
CF8	590	130	36	450
CF8M	220	30	53	572

Table 2.2: Composition of tracer elements in CF8 and CF8M CASS as received from EPRI castings, measured via quantitative analysis by combustion at Dirats Laboratories [27, 47]

and thermal embrittlement) primarily caused by spinodal decomposition. [4, 34, 36–38]. As detecting this form of degradation is an integral part of proactive management of nuclear material systems, [2] the materials susceptible to this form of degradation in a reactor are variants of CF3/CF3A/CF3M and CF8/CF8A/CF8M—the 'nuclear grade' CASS alloys, which contain 3-30% δ and 70-97% γ. [20, 39–46]

2.1.1 CASS CF8 (SS 304) and CF8M (SS 316) in Nuclear Light Water Reactor Systems

Across LWR systems in general, a myriad of structural materials is used to serve various roles in the reactor. For CASS in particular, reactor coolant and auxiliary system piping use grade CF8A, CF8M, and CF3M. Reactor coolant pump casings use grade CF8, CF8A, and CF8M. Reactor coolant valve bodies use grade CF8A and CF8M. [34] In replacements, CF3 is used rather than CF8 because its lower carbon content leads to less δ-phase formation, resulting in higher ductility and lower hardness—making it more difficult for embrittlement to occur [48].

Given that both CASS CF8 and CF8M are used in structural components on the primary side of the reactor, it is simply inevitable that these materials are exposed to environmental degradation factors throughout the lifetime of the reactor. Therefore, in this study, the CASS alloys investigated are CF8 and CF8M grade, and the chemical

Figure 2-1: Diagram of reactor system and constituent materials, adapted from [35] to highlight the extensive usage of 304 and 316 SS across reactor structural components. (Source: Roger Staehle, Beaune Workshop 2008)

composition of these alloys is listed in Tables 2.1 and 2.2. [27, 47] Further uses of CASS CF8 and CF8M alloys in nuclear systems can be seen in Figure 2-4 highlighted as "304 SS" for CF8 and "316 SS" for CF8M. In particular, the degradation factor investigated in this subset of CASS materials is thermal aging because it has been well-established that it leads to thermal embrittlement, [20–26, 49–53] and is a well-known fact that temperature acts synergistically with irradiation to drive microstructural degradation by the same mechanisms. [50–53] The following sections will highlight the rationale and characterization objective for the degradation of these materials in LWR systems, namely, how these materials degrade and what currently limits our ability to non-destructively detect spinodal decomposition in thermally aged CASS alloys.

2.2 Environmental Degradation of CASS Materials in Nuclear LWR Systems

As discussed in section 2.1, CF8 and CF8M are used at scale in the cooling systems of LWRs. For this use-case, the most deleterious degradation factor for these materials is the exposure to elevated temperatures throughout their service in the reactor. Thus, in context of the role of CASS alloys as structural materials in LWRs, the primary focus of the environmental degradation of these materials throughout this study is thermal aging—simulated as aging time at a set of temperatures that mirror reactor operating conditions.

2.2.1 Degradation Modes in CASS Alloys

In CASS materials, the general trend for thermal aging is decreasing ductility and toughness alongside increasing hardness and DBTT [54, 55]. Given the role of these materials in reactor systems as discussed in section 2.1, the most dangerous form of degradation is their exposure to thermal aging, and in turn, structural embrittlement, at temperatures that range from 280°C to 340°C, which fall within the range of reactor operational conditions. [56] Once the DBTT of the alloy, as measured by Charpy impact energy analysis, approaches room temperature, any pressurized thermal shock at room temperature can potentially cause total material failure [57]. Furthermore, the extent of thermal embrittlement depends on the grade of alloy (composition), the temperature at which the material was exposed, and how long the material was exposed to heating at any given temperature. [22, 26] Low-carbon grades such as CF3 are the most resistant to embrittlement, while high-carbon grades with high Mo content are the least resistant to thermal degradation [34]. This form of thermal degradation and embrittlement is caused by microstructural evolution that ultimately lead to the cleavage of the δ-phase, and, thus, the separation across the δ/γ phase boundary [58].

Considering the types of microstructural transformations that these materials are

susceptible to throughout their lifetime in a reactor, thermal aging effects due to microstructural degradation in the γ-phase are generally negligible because kinetics of phase transformation in austenite are slow in comparison to δ. Therefore, austenite retains its ductility throughout the time that the duplex alloy is used in a reactor, even when G-phase, carbide, and nitride precipitates may form slowly when exposed to elevated temperatures [36]. However, thermal embrittlement in CASS alloys is driven by microstructural phase transformations in the δ-phase and across the austenite-δ-ferrite boundary, primarily by two types of mechanisms: spinodal decomposition and nucleation/precipitation. [20–26, 49–53, 59–66]

In the classical theory describing phase transformation, the principle derived by Gibbs necessitates that the chemical potential of a component *must* increase with the density of that component. Ultimately, it has been shown by Cahn et al. that this thermodynamic driving force necessitates that $(\frac{\partial^2 G}{\partial c^2}_{T,P} > 0)$ must hold true for an alloy to remain stable with respect to changes in composition due to phase transformations. However, when this condition is unmet (i.e. $\frac{\partial^2 G}{\partial c^2}_{T,P} \leq 0$), there will be a thermodynamic driving force for phase transformations to occur. When this condition on stability is unmet, two distinct types of phase transformations, or *phase separations*, may occur depending on the alloy composition and temperature. As a result, two distinct phenomena (nucleation and spinodal decomposition) can arise when this condition on the stability of the alloy solution is unmet.

Considering the model solution illustrated in the free energy—composition diagram shown in 2-3, assuming that the thermodynamic state (P, T, c) of the solution mixture is in the linearly unstable region (where $g(c)$ is concave), continuous phase separation occurs spontaneously as it would drive an overall decrease in the free energy of the system—as illustrated in 2-3. This *continuous* process is an energetically favorable degradation mechanism for alloy compositions that lie in the region between inflection points corresponding to c_{s-} and c_{s+}, has been shown to depend on the elastic energy associated with these phase transformations. When the elastic strains are not constant in different crystallographic directions, the change in chemical potential that lowers the free energy of the system drives the displacement of adjacent atomic planes
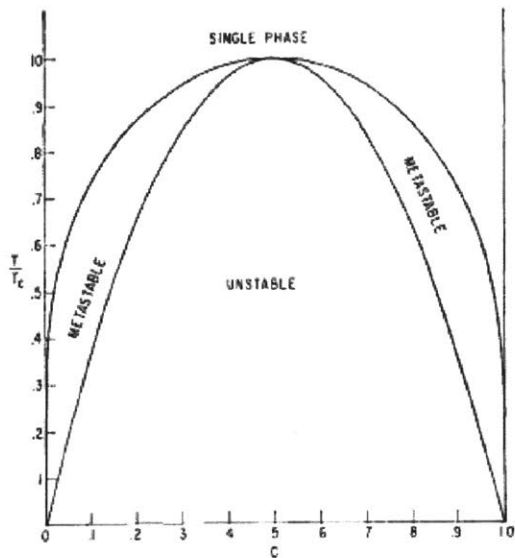
FIG. 7. Phase diagram of a regular solution showing the equilibrium phase boundary and the spinodal.

Figure 2-2: Phase diagram showing the equilibrium phase boundary and the unstable and metastable regions of a model regular solution (Source: [67])
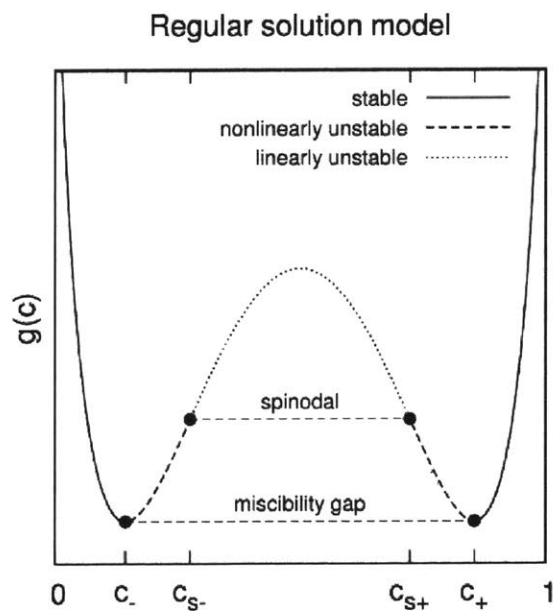
Figure 2-3: Free energy diagram showing the spinodal and miscibility gap of a model regular solution (Source: [68])

in a sinusoidally modulated manner. [69] Throughout this process, sinusoidally modulated changes in composition with increasing amplitude at a fixed wavelength, known as the spinodal wavelength, occur as a result of the elastic anisotropy of an unstable solution (the elastic constants not being constant in different directions). [69] This type of phase transformation occurs in specific crystallographic directions dictated by the elastic anisotropy of the solution, and is known as spinodal decomposition. [70]

Furthermore, the inflections points surrounding the region at c_{s-} and c_{s+} are known as the limit of metastability, or non-linear instability. For alloy compositions that lie in the metastable, non-linearly unstable region between the points at c_- and c_{s-}, as well as c_+ and c_{s+}, phase separation via spinodal decomposition is thermodynamically unfavorable. Instead, alloy compositions in the metastable region may only degrade (spontaneously) by a competing mechanism known as nucleation and growth. Although the condition on free energy for stability is met, i.e. $(\frac{\partial^2 G}{\partial c^2}_{T,P} > 0)$, the growth of a nucleus at the fixed low-energy compositions at c_- and c_+ for alloys at compositions between c_+ and c_{s+} as well as c_- and c_{s-}, respectively, may also drive phase transformation to lower the free energy of the system. However, in this case, there is a fundamental trade-off on free energy between the decrease the free energy by forming the low energy phases at c_- and c_+ (proportional to volume) and the increase in free energy associated with the interfacial energy γ due the growth of the new phase (proportional to surface energy). These two competing forces balance at a critical radius at which a nucleus larger than the critical radius will continue to grow spontaneously to lower free energy with increasing volume, and a nucleus lower than the critical radius will continue to shrink to lower interfacial energy due to the increasing surface area. This process occurs due to the existence of impurities across alloy solutions that serve as the growing nucleus, and is known as nucleation and growth, as well as precipitation.

To summarize the physical origin of the degradation phenomena that cause the embrittlement of the CASS alloys used in LWR systems, an important distinction is to be made between phase transformations that occur in the metastable region and the unstable region of the phase diagram. There are fundamental differences between

39

spinodal decomposition and nucleation deduced from the classical treatment of phase transformations. Spinodal decomposition is typically described as a phenomenon that is 'small in degree' and 'large in extent,' while nucleation is 'large in degree' and 'small in extent.' [68, 69] Spinodal decomposition begins with a small-amplitude change in composition at a fixed wavelength, passes through stages of increasing amplitude, and results in a large extent of change in composition. On the other hand, nucleation begins from a large extent of the new phase at a fixed composition, passes through stages of increasing extent of the formation of the new phase, and results in a small extent of change in composition.

In CASS alloys, degradation via spinodal decomposition in the δ-phase into nano-sized high-Cr α' and high-Fe α phases [71] hardens the δ-phase and reduces its plasticity and fracture toughness [72–74]. Next, the precipitation and growth of carbides, nitrides, and a high-Ni, high-Si G-phase [75–78] at the δ-γ boundary make cracks more likely to propagate through this interface region [34].

2.2.2 Kinetics and Evidence of Degradation in CASS Alloys

To quantify this phenomenon, the extent of thermal embrittlement is characterized by room-temperature (RT) normalized Charpy impact energy, which decreases with thermal aging [34]. The minimum RT Charpy impact energy at saturation does not depend on the aging temperature, but strongly correlates with the chemical composition of the steel [25]. Generally, the minimum RT Charpy impact energy decreases with increased ferrite content, increased concentration of carbides and nitrides, or increased percentage of Mo. [56]

Furthermore, the kinetics of thermal embrittlement, e.g. activation energy and aging time until saturation, are controlled by several factors. Since spinodal decomposition of the δ-phase is the primary mechanism of thermal aging, the size and spacing of the α'-phase is what primarily controls embrittlement kinetics [71]. A larger size of α'-phase and smaller spacing in between should lead to a higher activation energy and faster embrittlement because the spinodal decomposition process occurs very quickly across a short range. Low activation energies and slow embrittlement is typically

40
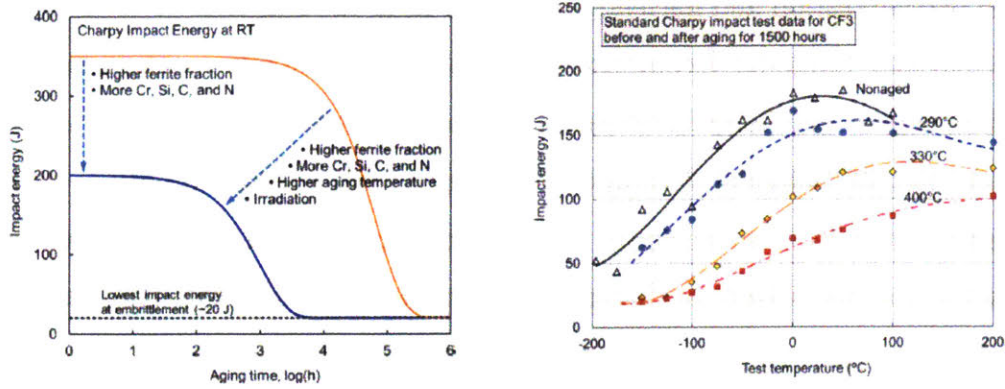
Figure 2-4: (a) Schematic of the embrittlement process using the Charpy impact energy to quantify the extent of thermal embrittlement [34] (b) Aging temperature dependence of Charpy impact energy in CF3-grade CASS [34]

attributed to the increasing presence of G-phase due to carbide-nitride precipitation and growth. Furthermore, the kinetics of the embrittlement mechanisms discussed previously are enhanced to occur even faster (lower aging time until saturation) when the aging temperature is increased [56].

Overall, thermal degradation in CASS materials depends on both intrinsic factors (e.g. material properties and composition) and extrinsic factors (e.g. aging temperature, irradiation). [34] These factors may also act synergistically to introduce further or enhanced degradation modes. For LWRs and nuclear systems in general, it has been well established that irradiation acts synergistically with thermal aging when CASS materials are exposed to irradiation in the reactor environment. [50–53] Although the extent to which irradiation (or other external factors) can enhance thermal aging depends on the type of irradiation and exposure time, and other complex radiation-matter interactions, the mechanism of degradation by embrittlement remains the same.

2.3 Characterization of Spinodal Decomposition in LWR CASS Materials

Now that we have established that spinodal decomposition is the primary mechanism of embrittlement for CASS materials through thermal aging, we seek to explore the main methods to characterize this degradation process.

2.3.1 Methods to Detect Microstructural Degradation

Technique	*Nondestructive*	*Noncontact*	*Rapid*	*Depth* $\sim 1\mu m$	*Spatial* $\sim 100\mu m$	*In situ capability*
UT	x		x			
S/T EM				x	x	
CIT				Bulk	Bulk	
SAM	x		x			
SLAM	x		x			
HOLO SLAM	x		x			
SBSS	x	x		x	x	x
Piezo-SAW	x		x	x		
APT		x		x		
XRD	x	x		Bulk	Bulk	x
SAXS	x	x		x	x	x
Indentation	x[0]			x	x	
RUS	x	x	x	x	x	x
PALS	x	x		x	x	x
TGS	x	x	x	x	x	x

UT—Ultrasonic Testing
S/T EM—Scanning/Transmission Electron Microscopy
CIT—Charpy Impact Test
SAM—Scanning Acoustic Microscopy
SLAM—Scanning Laser Acoustic Microscopy
HOLO SLAM—Holographic SLAM
SBS—Surface Brillouin Scattering Spectroscopy
Piezo-SAW—Piezo-based Surface Acoustic Wave Spectroscopy
APT—Atom Probe Tomography
XRD—X-Ray Diffraction
SAXS—Small Angle X-Ray Scattering
Indentation—Nanoindentation and Microindentation
RUS—Resonant Ultrasonic Spectroscopy
PALS—Positron Annihilation Lifetime Spectroscopy
TGS—Transient Grating Spectroscopy

Table 2.3: Survey of characterization tools/methods for detecting microstructural degradation surveyed for strengths and limitations (Adapted from [8])

---

[0]pseudo-non-destructive for nanoindentation.

Currently, TEM imaging and microanalysis is necessary to probe microstructural changes in materials by elementally mapping the spatial distribution of atoms using a technique known as energy-dispersive x-ray (EDX) microanalysis. A typical TEM image for a thermally-aging CASS alloy is shown in Figure 1-2 in Section 1.1. However, TEM analysis is extremely expensive and time-consuming, and is inherently limited by its ability to only survey a small portion of the bulk sample. In addition, the practical issues with inserting/removing material coupons from the radiation environment can introduce additional artifacts from sample preparation steps, which can potentially obscure the levels of accumulated environmental degradation from thermal aging, radiation damage, and the like. [79, 80] Furthermore, these material coupons are also limited in quantity and are often depleted over the lifetime of the system serviced (i.e. in this case, the reactor). Similarly, microanalysis can also be performed via APT but is also limited by its ability to survey a small portion of the bulk samples, in addition to the disadvantages associated with the destructive nature of preparing specimens for this class of characterization techniques. [81]

Therefore, in light of this challenge to the characterization of microstructural degradation in nuclear materials, the key to understanding how environmental conditions and material properties change is a non-destructive (NDE) technique to probe the extent of degradation spatially and temporally (i.e. in real time). Thus, an ideal method for this kind of *in situ* analysis would also need to be non-destructive and non-contact. [8] In addition, the technique must be able to collect data rapidly and study multiple material properties at once. Since *in situ* analysis is desired, the probes must be able to probe surface and near-surface phenomena to the depth of ion diffusion ($\sim$1 micron in the case of charged particle damage only). [8] The method must also function well in extreme temperature environments with samples immersed in vacuum, high pressure gases, or corrosive fluids. [8] With these features, detecting spinodal decomposition in CASS alloys via a non-destructive tool can be established by correlating a measured quantity with a known feature attributed to this mode of degradation using the tools currently available.

Given that we have identified the key features required for non-destructive eval-

uation of nuclear materials generally and spinodal decomposition in CASS materials specifically, we can now survey and evaluate potential methods for mechanical spectroscopy of materials degradation. First, we will consider conventional ultrasonic testing (UT). This method can only detect flaws on the scale of microns but is too low resolution to detect many of the microstructural degradation features that occur at the nanometer scale such as G-phase precipitations in CASS alloys. [82] Although resonant ultrasound spectroscopy (RUS) has a higher resolution due to its ability to measure non-linear parameters can be used to calculate elastic constants to detect microstructural degradation, it is inherently limited by the quality of sample and its geometry during the measurement. [83] Using a technique such as X-Ray Diffraction can overcome the challenges with quality of the sample and its geometry by probing the bulk sample at once with fully penetrating x-ray irradiation, however, is limited in the detection of smaller signatures of microstructural degradation because any mixed phases must exceed a certain threshold ($\sim 2\%$) of the overall chemical composition for it to be detectable by XRD with a resolution limit of 2nm. [84]

To detect microstructural degradation that lead to changes of material properties at the mesoscale, mechanical testing can also be employed to correlate such material properties back to microstructural degradation as indirect evidence. For example, thermal embrittlement via spinodal decomposition leads to higher hardness and lower ductility. Thus, micro or nanoindentation can be used to probe the hardness of the sample to inspect whether spinodal decomposition has occurred. Furthermore, indentation is limited in spacing between indents, and the spacing must exceed approximately ten times the penetration depth of the indent. The scale of penetration depths for microindentration and nanoindentation are in microns or tens to hundreds of nanometers, whereas the spacing between phases in spinodal decomposition typically occurs on the order of 2-5nm for CASS alloys, as shown in Fig. 1-2.

In addition, Charpy impact testing may also be used to measure the ductility of the bulk sample to inspect for a decrease in ductility. However, both techniques are destructive and require physical contact with the sample, also making it difficult to employ them in situ. This warrants the need to perform these measurements on

material coupons, which 'come with' other challenges such as running out material coupons over time, not being able to probe kinetics and mechanisms of degradation, and slow, inefficient turnaround on testing.

However, material properties detected via destructive, contact-based mechanical tests often correlate to properties measured by non-destructive, non-contact spectroscopy techniques, which can be alternatively used to detect microstructural degradation by conducting the appropriate reference studies to correlate microstructure to measured property accordingly. Common methods for mechanical spectroscopy are Piezo-based surface acoustic wave (SAW) analysis, [85] scanning laser acoustic microscopy (SLAM), [86] three-dimensional holographic SLAM (HOLOSLAM), [87] and scanning acoustic microscopy (SAM). [88] However, Piezo-SAW and acoustic methods such as SAM, SLAM, and HOLOSLAM require coupling the measurement with a mechanical or fluid medium such as a solid, oil, or water. [8] As a result, these methods cannot be performed *in situ* in extreme environments of temperature and irradiation.

Surface Brillouin Scattering (SBS) is also commonly used among mechanical spectroscopy techniques. This technique measures small fluctuations in incident light due to atomic vibration spectra. The issue with this method is that it takes an extremely long time to collect one data point, making it difficult for this to be used for real-time in-situ analysis. [8,89] Small Angle X-ray Scattering (SAXS) is another spectroscopic technique that can be used *in situ* to quantify the spatial distribution of atoms at the nanoscale to detect microstructural degradation. However, SAXS requires the usage of a synchrotron, which can accrue further microstructural damage from the probing irradiation beam itself, is extremely expensive, and is often limited in accessibility at large research facilities. [90] Positron Annihilation Lifetime Spectroscopy (PALS) offers the advantage of being relatively inexpensive and can be performed in-situ for the detection of microstructural degradation, but is limited by the deep, uncontrolled penetration of positrons and, thus, can only measure average values of material properties (along the path of the positron until it annihilates). [91]

Finally, laser-generated surface acoustic wave (LSAW) metrology is class of me-

chanical spectroscopy techniques that are typically implemented via four distinct methods: interferometry, reflectivity analysis, deflection methods, and diffraction methods—including transient grating spectroscopy (TGS). [92] LSAW analysis is a non-contact, non-destructive technique that can be used *in situ* during irradiation since the probes are not electronic and will not be damaged by radiation as well. [93] In particular, TGS can collect data rapidly (hundreds of thousands of signals data averaged in minutes) to perform LSAW analysis on LWR structural materials such as CASS alloys. [94] The laser probes in LSAW-based can also penetrate the specimen beyond the surface, which typically require $\sim$1 micron of depth. [95] The main practical limitation to this approach is that it still requires establishing correlations between TGS spectral changes with the conventional understanding of material degradation in general and environmental degradation in particular.

2.3.2 Detecting Microstructural Degradation via LSAW Analysis

By assessing the advantages and disadvantages of each characterization tool, as summarized in Table 2.3, this thesis attempts to establish TGS as the most suitable technique for *in situ* characterization of microstructural degradation due to thermal aging. Although the technique is relatively new to nuclear structural materials, the non-destructive and non-contact capability of TGS allows us to eliminate the contending spectroscopic methods—excluding SBS. However, the ability to collect data rapidly with TGS in a matter of seconds/minutes as opposed to weeks/months with SBS makes TGS more practical for *in situ* analysis of materials degradation. [89] This is because the added benefit of performing measurements *in situ* will not be realized given the prolonged time it takes to collect data for SBS. Overall, TGS satisfies the criteria needed to correlate material properties to environmental degradation factors such as thermal aging and irradiation, and provides the spatial and temporal information on microstructural degradation—non-destructively, and in a non-contact and rapid manner. [8]

46

By performing SAW analysis on TGS spectral changes, recent studies have already demonstrated that quantities relevant to microstructural degradation can be measured reliably. [6, 8–18] A study on silicon-on-insulator (SOI) substrates showed that the dislocation density correlates with the decay constant obtained from SAW analysis, which was important for establishing the correlation between TGS spectral changes and DPA as a measure of microstructural degradation due to radiation damage. [96] Results from laser interferometry performed on copper samples with high anisotropy to study neutron radiation damage suggest that SAW analysis could measure changes in elastic properties that reflect microstructural degradation from irradiation. [12] Another study focused on SAWs in single-crystal tungsten used TGS for SAW analysis to quantify the changes in Rayleigh wave velocity, Young's modulus, shear modulus, and other elastic properties due to helium implantation for fusion reactor first wall applications. [94]

Such studies show that changes in TGS signals can reliably probe various material properties via SAW analysis, as shown in Table 3. [8] With further TGS studies on LWR structural materials in particular, this can be extended to detecting spinodal decomposition in CASS alloys to detect the extent of thermal aging and predict the expected time to reach thermal embrittlement. Ultimately, the ability to quantify this mode of microstructural degradation in CASS materials can serve to support LWR reactor life extensions or early shutdown depending on the health of structural components and replacement costs.

The unique capabilities of TGS have demonstrated that it is suitable for detecting microstructural degradation by correlating results from TGS measurements to well-understood material properties, in particular to show that it can be used to non-destructively detect spinodal decomposition as an indicator of thermal aging/embrittlement in CASS-based LWR structural materials. In addition to detection of microstructural degradation in materials, the ability to collect data rapidly in response to environmental factors *in situ* provides insight into the mechanisms of microstructural damage by analyzing the shape of property-response curves.

For example, as shown in Figure 6a, in a study on void swelling of ferrite and

47

Radiation Damage Mode	Estimated Effect on the Material	Change in LSAW signal
Void formation	Decrease in thermal diffusivity	Decrease in overall curve slope of thermal decay
Dislocation buildup	Phonon scattering, SAW scattering	Faster acoustic damping time constant
Point defects (measurable conc. at very low temps)	Stiffening, softening	Change in Rayleigh wave frequency

Figure 2-5: Expected changes in TGS signal with representative effects of the types of materials degradation modes that can be detected [8]

sorbite, [97] researchers used a smooth exponential fit for ferrite data and a bilinear fit on sorbite data to provide insight into distinct degradation mechanisms for both phases. However, the data points are sparse so the curve fit models may not match the mechanism of degradation had the gaps in the data been filled. In contrast, if TGS was performed in-situ for such studies, more conclusive mechanistic information could be inferred from the data collected in the gaps during the onset of the accumulated damage (e.g. in this study, void swelling). [12] Now, recent studies have emerged showing that TGS is, in fact, a viable method with predictive capabilities to characterize materials with the sensitivity required to detect changes in material properties that indicate degradation. [6, 8–18]. A close agreement between observed results and predictive calculations using classical molecular dynamics (MD) simulations have also been shown. [6] In 2016, Dennett et al. and Ferry et al. performed benchmark TGS measurements on metallic single crystals that showed a 0.1% absolute sensitivity and <575 ppm relative sensitivity, proving its ability to repeatedly detect small changes in elastic properties due to material degradation induced by irradiation. [6] In addition, as shown in Figure 6b, classical MD was used to simulate the SAW excitation and detection process with close resemblance to experimental results. [6, 10] Similarly, using

TGS consolidates the ability to monitor the progression of degradation modes caused by thermal and irradiation aging such spinodal decomposition and embrittlement in CASS materials.

Because TGS is a form of gigahertz, non-contact ultrasonic testing, it can be used to monitor and evaluate the health of nuclear structural materials, including CASS. This technique is performed by generating a surface acoustic wave (SAW) using a pump laser that creates waves of thermal expansion. Then, changes in this SAW are analyzed using a probe laser that measures the propagation and decay of the surface wave. A diagram showing the sample surface, the pump laser, probe laser, and formation of SAWs is seen in Figure 2-7. A single TGS measurement takes ≈100 nanoseconds with a sampling rate of 1kHz to ensure robust statistics. [6, 10, 98] During this pulse, as shown in Figure 2-6 the probe laser diffracts off the 'transient grating' produced by the SAW, and changes in this diffraction signal reflect the material properties that can then be used as metrics to monitor degradation. [10]. Given that the spot size of TGS is about 150 microns in size, any phases illuminated by the spot will contribute to the diffraction signal. [6, 98] Thus, our hypothesis is that resolving the TGS signal in the frequency space will allow us to detect phase transformations, and, in turn, microstructural degradation, by comparing changes in the SAW speeds/frequencies and elastic properties measured in samples aged in varying conditions.
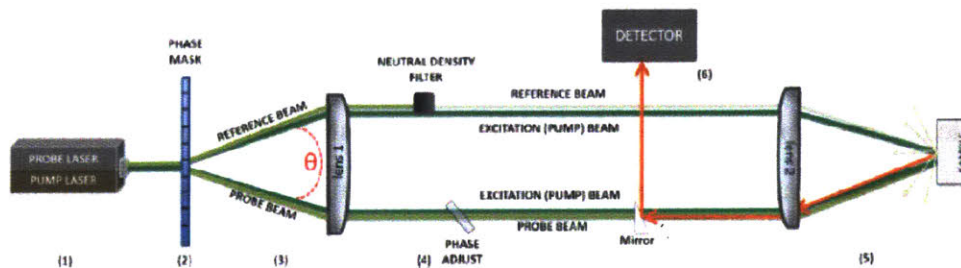
Figure 2-6: Diagram of a TGS experimental apparatus [8]

In summary, in order for TGS to be applied practically as an in-vessel inspection technique for the monitoring and evaluation of structural materials, it is required to meet the criteria set forth in sections 2.3.1 and 2.3.2. Specifically, the detection of mi-
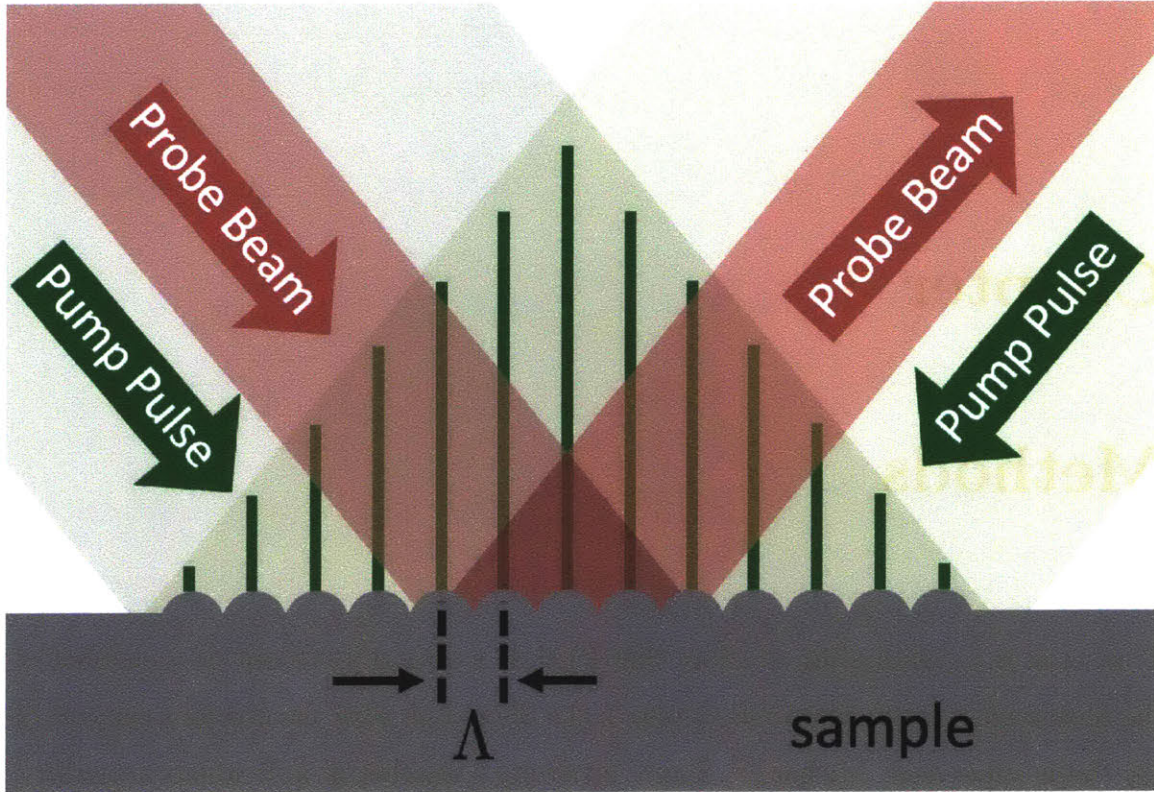
Figure 2-7: Diagram of SAW generation due to pump pulse interference. Probe beam leads to detector and outputs signal such as the one seen in Figure 3-6. Adapted from [6] in collaboration with Benjamin Dacus through [19]·

crostructural degradation in the form of spinodal decomposition involve requirements that are best satisfied using TGS. Namely, this form of gigahertz ultrasonics is (a) non-destructive, (b) non-contact (at a distance), (c) rapid, (d) have $\sim 100\mu m$ of spatial resolution as well as $\sim 1\mu m$ of depth resolution to be sensitive to probe multiple phases at once, (e) supported by predictive modelling and can be correlated empirically to established techniques for validation, and (f) equipped with in-situ capability for field implementation. For these reasons, this thesis attempts to establish this tool as an in-vessel inspection technique by linking changes in SAW characteristics to microstructural degradation, as confirmed and validated by contending materials characterization techniques and elastic theory predictions.

Chapter 3

Methods

This work is a culmination of effort that I led as a master's student as a member of the Mesoscale Nuclear Materials Group in the Short Lab with the gracious support of my thesis supervisor, Michael P. Short, involving a number of individuals accredited for their contributions throughout the thesis, and was published in the Proceedings of the 19th International Conference on Environmental Degradation of Materials in Nuclear Power Systems-Water Reactors. [19]

3.1   Sample Preparation and Aging Conditions

All samples were cut along the tangential direction of the original casting. CF8 and CF8M CASS samples were aged by researchers at PNNL [?, 27]for 10,000 hours and 30,000 hours at 290°C, 330°C, 360°C, and 400°C, along with an unaged control sample from each corresponding casting. Thin 1mm-thick cross-sectional samples were cut using a low-speed saw cutter (IsoMet by Buehler), then polished down to $0.05\mu m$ grit size using alumina MasterPrep on a rotating mount polishing system. Microstructural characterization via SEM and TEM, TGS, microindentation and nanoindentation measurements were performed on these samples as described in the relevant sections below.

3.1.1 Charpy Impact Testing

Impact tests were performed by researchers at PNNL [27, 47] for CF8 and CF8M CASS alloys aged at 10,000 hours and unaged control samples on standard Charpy V-notched samples (10mm x 10mm x 25mm) using a 350J capacity Charpy impact tester. Only room temperature (RT) Charpy impact energies from these measurements are presented to correlate with RT TGS data, which were obtained from several tests that were done in a wide temperature range to construct temperature ductile-brittle transition curves for each sample at each aging condition.

3.2 Microstructural Characterization

Thin-foil specimens for TEM characterization of CF8 aged at 400°C for 10,000 hours as well as unaged control were prepared from 3.0 mm diameter disc samples that had been mechanically thinned to 100μm and subsequently electropolished in a solution of 20% $HClO_4$ and 80% CH_3OH at -35°C. These specimens were subsequently analyzed by Prof. M. Grace Burke of the University of Manchester, UK, in a Philips CM20 200 kV LaB_6 TEM and an FEI Talos F200 S/TEM with X-FEG and Super X (4 SDDs) for STEM-EDX spectrum imaging and microanalysis. The STEM-EDX Spectrum Image datasets were processed using FEI Velox 2.3 software.

The fracture surfaces of the same CF8 alloy specimens (unaged control and aged 400°C for 10,000 hrs) were examined in a Zeiss Merlin field emission gun scanning electron microscope (FEG-SEM) equipped with two Oxford Instruments X-Max 150 Silicon drift detectors (SDDs) for energy dispersive x-ray (EDX) microanalysis.

3.3 Micro and Nanoindentation

Nanoindentation measurements were performed on the complete set of CF8 alloy specimens aged for 10,000 hours along with an unaged control using a TI 950 Tri-boIndenter from Hysitron with a Berkovich diamond indenter tip. Samples were tested under load control using a trapezoidal load function, with 10 seconds loading,

5 seconds holding, 10 seconds unloading with a peak force of 10 mN. A 25x25 grid of indents were performed in a 120x120 micron area with 5 microns in between. An optical micrograph of a representative sample after nanoindentation is shown in Figure 3-1.
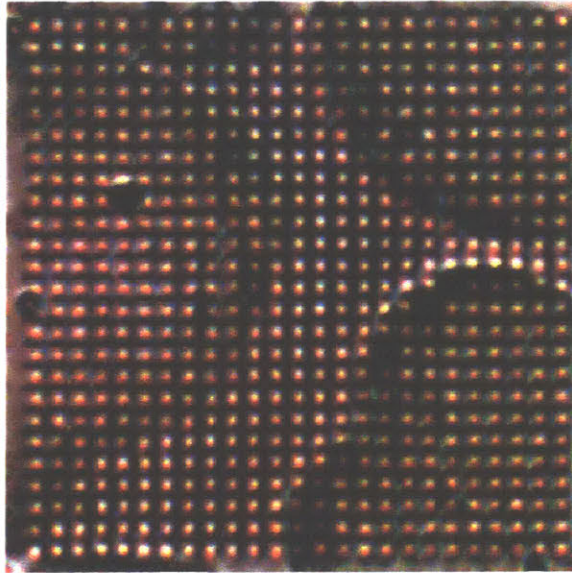
Figure 3-1: Optical micrograph showing 25x25 grid of nanoindents performed in a 120x120 micron area.

Vickers microhardness indents were also performed on the same set of CF8 samples aged for 10,000 hours along with an unaged control via a Vickers LECO Microhardness tester using a 5g force to minimize indentation size, and to localize the indent entirely within either austenite or δ-ferrite grains. A dwell time of 15 seconds was used, and the indent size is measured as the average of the two diagonals.

3.3.1 Oliver-Pharr Indentation Analysis

Raw displacement curves collected from nanoindentation were analyzed using Oliver-Pharr analysis to calculate reduced modulus, contact stiffness, and nanohardness. [99] First, hardness is given by the following equation, using A as the projected area of elastic contact, and P_{max} as the maximum load at maximum penetration depth—as shown in Figure 3-2:

$$H = \frac{P_{max}}{A} \tag{3.1}$$

Next, stiffness is given by:

$$S = \frac{dP}{dh} = \frac{2}{\sqrt{\pi}} Er\sqrt{A} \tag{3.2}$$

The value of $\frac{dP}{dh}$ is taken as the slope of the load-displacement curve at 95% of the max penetration depth, h_{max} as shown in Figure 3-2. Using A as previously defined, the reduced modulus, E_r, is then calculated from equation 3.2.

$$\frac{1}{Er} = \overbrace{[\frac{(1 - \nu^2)}{E}]}^{\text{sample material properties}} + \underbrace{[\frac{(1 - \nu_{tip}^2)}{E_{tip}}]}_{\text{tip material properties}} \tag{3.3}$$

Next, equation 3.3 is solved for the Young's modulus of the material, E using ν_{tip} as 0.07 and E_{tip} as 1140GPa for the diamond tip used in this study along with the Poisson ratio of the sample of interest. In our case, ν for CASS alloys is used as 0.28. [100]

3.3.2 Bayesian Information Criterion (BIC) Phase Clustering

Processed data from performing Oliver-Pharr analysis on nanoindentation results were analyzed using BIC phase clustering to determine the material properties in each phase of the material, as described in [101–103].[1] In short, this was achieved by interpolating material property values across the spatial grid of indents, and then clustering the data by plotting hardness vs. elastic modulus. (Figure 3-3)

---

[1] Analysis code developed in collaboration with Omar A. Al Dajani, Konrad J. Krakowiak, Prof. Franz.-J. Ulm
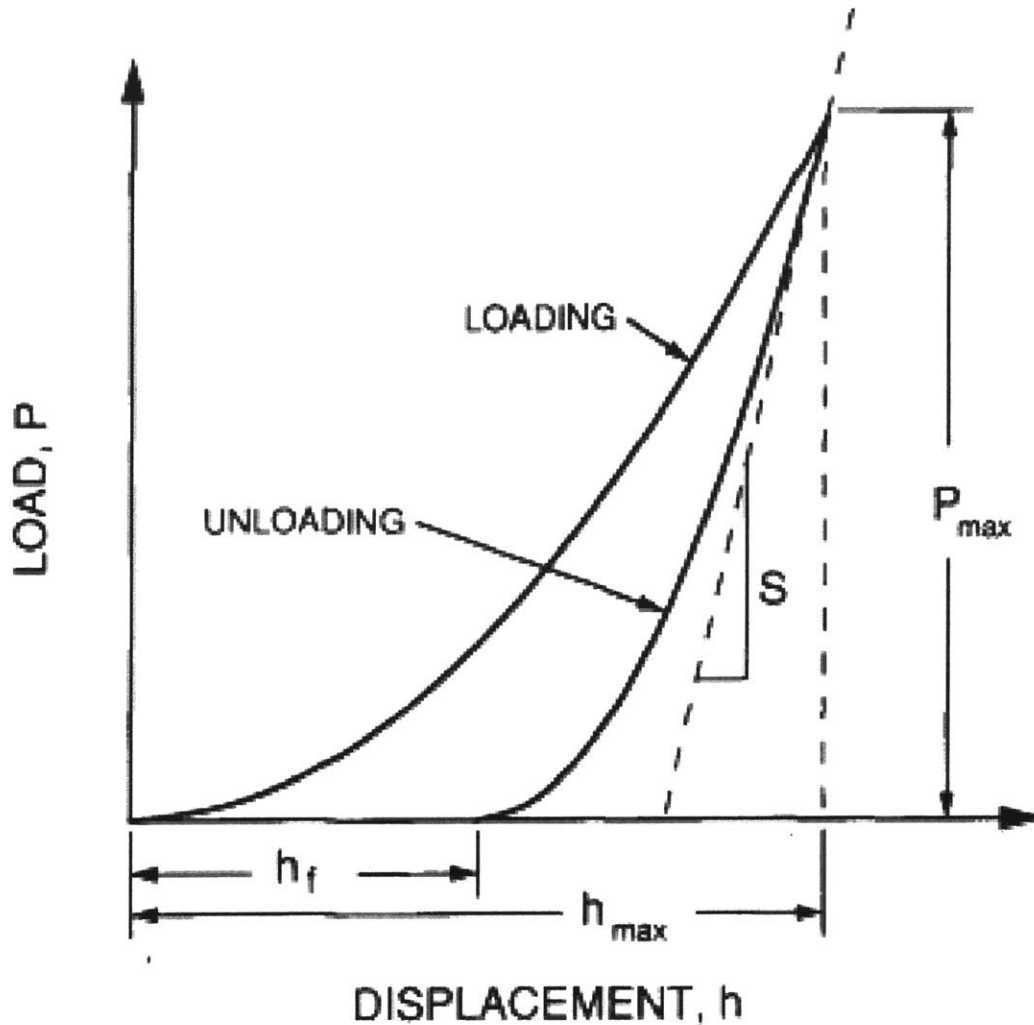
Figure 3-2: Raw displacement curve from [99] annotated with measured quantities from an indentation experiment: P_{max} as the peak indentation load used to calculate hardness, S as the unloading stiffness used to calculate reduced and elastic modulus.

The optimal number of phases in each indentation map is determined in a statistical manner by taking the number of phases that minimize the overall BIC error and assigning a phase to each spatial location based on the hardness and elastic modulus at the same location. (Figure 3-4)

Using this approach, hardness, stiffness, and elastic modulus for ferrite, austenite, and the interfacial regions are estimated, and the mean and standard deviation for each phase are reported in the corresponding sections of Results. (Figure 3-5)
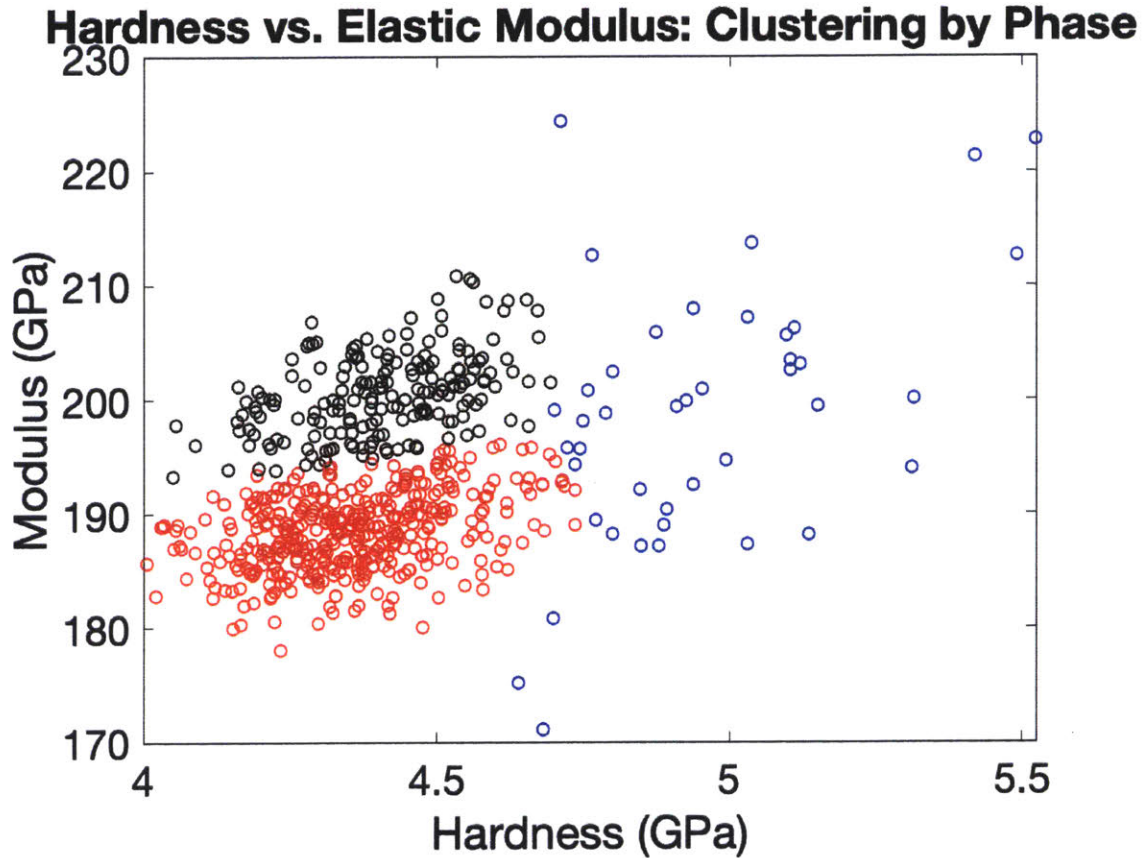
Figure 3-3: Clustering by phase via plotting nanohardness versus nanoelastic modulus

https://github.com/shortlab/SDajani-Thesis

3.4 Transient Grating Spectroscopy (TGS)

Four sets of samples were scanned via TGS: CF8 and CF8M alloys aged at 10,000 hours and 30,000 hours. Each sample was scanned in air and in vacuum with 10 spots each for statistical significance on the results of LSAW analysis.

3.4.1 SAW Frequency Predictions

Using the elastic constants for CASS CF8 shown in Table 3.1 from [105], the method developed in [11] was adapted in this thesis to predict the variation in theoretical SAW, PSAW, and bulk wave frequencies in these materials due to the random crystal orientation present in the polycrystalline specimens investigated in this study. Since

56
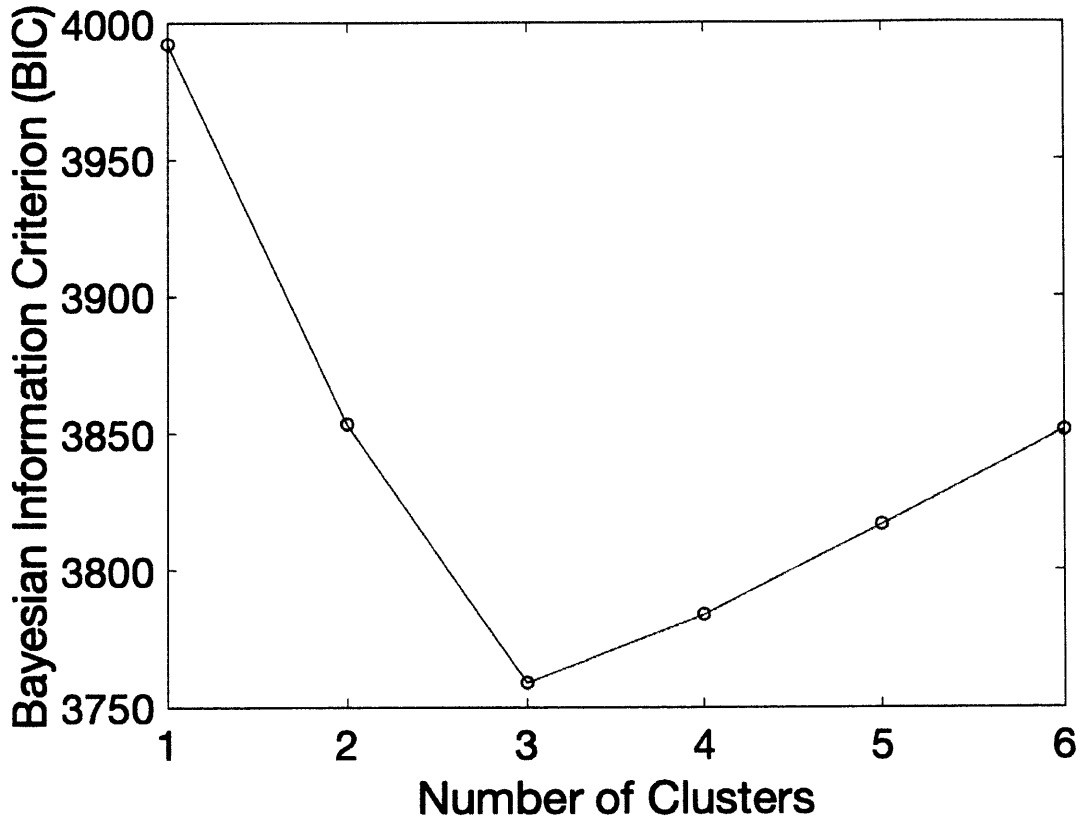
Figure 3-4: Plot generated to select the optimal number of phases by minimizing the BIC error calculated from 3-3

the crystal structure for these alloys exhibits cubic symmetry, the range of predicted frequencies is calculated across miller indices from $0°$ to $90°$, with approximately $5°$ in between each plane.

The algorithm was developed by [11] in MATLAB based on the elastodynamic wave equation for a homogeneous, anisotropic crystal assuming linear elastic deformation and the absence of any external forces or fields. The governing equation, as presented by [11], is used to output predicted acoustic velocities along any arbitrary crystallographic direction with given crystal structure symmetry, elastic tensor entries, and material density as inputs—expressed as:

$$C_{ijkl}\frac{\partial^2 U_l}{\partial x_j \partial x_k} = \rho\frac{\partial^2 U_l}{\partial t^2} \ni x_3 \le 0 \tag{3.4}$$
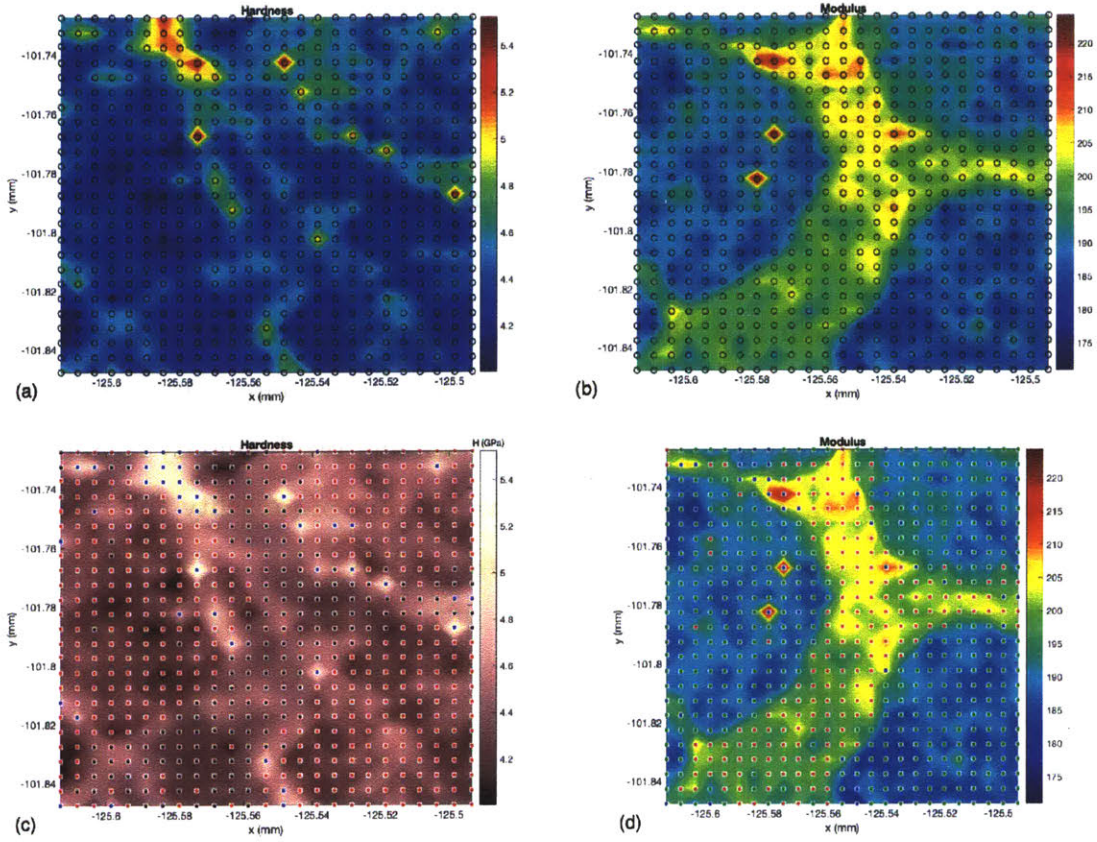
Figure 3-5: Assigning nanohardness and elastic modulus (c-d) to each phase in nanohardness and elastic property maps (a-b).

with U as displacement, ρ as crystal density, C_{ijkl} as elastic constants (also known as elastic tensor entries), and x and t as space and time, respectively. The condition on x_3 considers only the lower half of the crystal, treated as a semi-infinite system. When the x_3 constraint is removed, three bulk wave modes are solutions to Eq. 3.4, which are reached by substituting in U as an exponential: (1) longitudinal (L) wave, (2) fast transverse (FT) wave, and slow transverse (ST) wave. In this approach, the Einstein summation is the mathematical convention employed and the result presented is reached following the elegant derivation summarized by Rosenbaum. [11]

$$U_i(\vec{r}, t) = U_i(x, y, z, t) = 0 \ni t < 0 \tag{3.5}$$

Elastic Constant	C_{11}	C_{12}	C_{44}	Reference
Monocrystal SS304 (Calculated) $[N/m^2]$	$229.03 * 10^9$	$135.81 * 10^9$	$116.78 * 10^9$	[104]
Monocrystal SS304 (Calculated) $[N/m^2]$	$200.4 * 10^9$	$129.3 * 10^9$	$125.8 * 10^9$	[105]
Monocrystalline SS304 (Experimental) $[N/m^2]$	$204.6 * 10^9$	$137.7 * 10^9$	$126.2 * 10^9$	[106]
Polycrystalline SS304 (Experimental) $[N/m^2]$	$261.4 * 10^9$	$106.6 * 10^9$	—	[106]

Table 3.1: Values of elastic constants for monocrystal and polycrystalline 304-type stainless steel

According to these solutions, the response of surface displacement as a result of laser impingement acting as an external force being exerted in a semi-infinite crystal as a point stimulus is modelled using an initial condition and two boundary conditions. The initial condition, Eq. 3.5, is described by the principle of causality and refers to the lack of any displacement prior to the laser trigger. [11]

Newton's second law: $\Sigma \vec{F_i} = m\vec{a_i} = \int_V \rho f \partial V = \int_V \rho(\vec{r},t)\frac{\partial u_i(\vec{r},t)}{\partial t^2}\partial V$ (3.6a)

$$\implies \vec{f_i} = \frac{\partial u_i(\vec{r},t)}{\partial t^2} \tag{3.6b}$$

Force balance: $\int_S \vec{T}((\hat{n}))(\hat{n})\partial S + \int_V \rho(\vec{r},t)\vec{g}\partial V = \int_V \rho(\vec{r},t)\vec{f_i}\partial V$ (3.6c)

Hooke's Law in continuous media:

$$\vec{T}(\hat{n}) = \hat{n}_i T(x_i) = \sigma_{ij}(\vec{r},t)\hat{n} = \sum_{k=1}^{3}\sum_{l=1}^{3} c_{ijkl}\epsilon_{kl}\hat{n} = C_{ijkl}(\vec{r},t)\hat{n} \tag{3.6d}$$

$$\implies \int_S \sigma_{ij}\hat{n}\partial S + \int_V \rho(\vec{r},t)\vec{g}\partial V = \int_V \rho(\vec{r},t)\vec{f_i}\partial V \tag{3.6e}$$

Divergence theorem: $\int_S \sigma_{ij}\hat{n}\partial S = \int_V \vec{\nabla}\sigma_{ij}\partial V$ (3.6f)

$$\implies \int_V [\vec{\nabla}\sigma_{ij} + \rho(\vec{r},t)\vec{g}]\partial V = \int_V \rho(\vec{r},t)\vec{f_i}\partial V \tag{3.6g}$$

$$\therefore \vec{\nabla}\sigma_{ij} + \rho(\vec{r},t)\vec{g} = \rho(\vec{r},t)\vec{f_i} \tag{3.6h}$$

$$\implies \frac{\partial \sigma_{ij}(\vec{r},t)}{\partial x_j} = \rho(\vec{r},t)\frac{\partial u_i(\vec{r},t)}{\partial t^2} \tag{3.6i}$$

$$\frac{\partial \sigma_{ij}(\vec{r},t)}{\partial x_j} = \rho(\vec{r},t)\frac{\partial u_i(\vec{r},t)}{\partial t^2} \text{ (absence of any body forces)} \tag{3.6j}$$

$$\therefore \frac{\partial C_{ijkl}(\vec{r},t)}{\partial x_j}\frac{\partial u_k(\vec{r},t)}{\partial x_l} = \rho(\vec{r},t)\frac{\partial u_i(\vec{r},t)}{\partial t^2} \tag{3.6k}$$

$$\implies \begin{cases} C_{ijkl}\frac{\partial U_l(\vec{r},t)}{\partial x_j \partial x_k} = \rho(\vec{r},t)\frac{\partial U_l(\vec{r},t)}{\partial t^2} \text{ (homogenous medium) [11]} \\ \\ C_{ijkl} = \begin{pmatrix} c_{11} & c_{12} & 0 \\ c_{12} & c_{11} & 0 \\ 0 & 0 & c_{44} \end{pmatrix} \text{ (cubic anistropy) [107]} \end{cases} \tag{3.6l}$$

60

$$\sigma \Big|_{z=0} = C_{i3kl} \frac{\partial U_l}{\partial x_k} \Big|_{z=0} = \delta_{i3} \delta(x,y) \delta(t) \tag{3.7a}$$

$$U_i(\vec{r}, t) = U_i(x, y, z, t \to \infty) = 0 \tag{3.7b}$$

such that:

$$\delta_{i3} = \begin{cases} 1 & i = 3 \\ 0 & \text{otherwise} \end{cases} \tag{3.8a}$$

$$\delta(x,y) = \delta(x)\delta(y) \ni \tag{3.8b}$$

$$i, j, k, l = 1, 2, 3 \tag{3.8c}$$

Under this problem formulation, the first boundary condition in Eq. 3.7a corresponds to the starting point when the external force exerted by the laser perturbation is only exerted on the origin with non-zero stress normal to the surface. The second boundary condition in Eq. 3.7b corresponds to the vanishing displacement as the elastodynamic wave propagates and decays to zero as $\vec{r}$ and t approach infinity. [11]

Once the bulk wave (BW) solutions are computed, a displacement-slowness profile is generated for each crystallographic orientation and relative surface angle to identify the surface modes as SAWs, also known as Rayleigh waves (RW), or pseudo SAWs (PSAWs), also known as leaky SAWs. If the RW is too slow to be observable, the PSAW and bulk wave are selected. If the bulk wave is faster than the PSAW, the SAW and the bulk wave are selected. Otherwise, the SAW is selected as the lower velocity and higher slowness and PSAW as the higher velocity and lower slowness. Thus, for each orientation and surface, two acoustic modes are identified by the algorithm as SAW and PSAW, SAW and BW, or PSAW and BW. [11, 98] Finally, these modes are computed and plotted for each crystallographic orientation for a polarization range

from 0 to $\frac{\pi}{2}$ (cubic symmetry) over a range of relative surface orientations from 0 to π.

3.4.2 TGS Analysis

The frequency spectrum of the TGS signal (colloquially referred to as the 'power spectrum') reveals the elasticity of the material of interest, the decay constant reveals the thermal diffusivity, and the wave persistence reveals the acoustic damping. [10]. These properties and the corresponding SAW frequencies are calculated by fitting a curve to the TGS signal. The functional TGS equation describing multiple, concurrent SAW frequencies is given by:

$$I(t) = A \overbrace{\left[\mathrm{erfc}\left(q\sqrt{\alpha t}\right) - \frac{\beta}{\sqrt{t}} \exp\left(-q^2\alpha t\right) \right]}^{\text{thermal grating decay}}$$
$$+ \underbrace{\sum_{i=1}^{n} B_i \sin\left(2\pi f_i t + \phi_i\right) \exp\left(-t/\tau_i\right)}_{\text{damped acoustic oscillations}} + \underbrace{C}_{\text{constant offset}} \tag{3.9}$$

The thermal grating decay equation is used in order to find the thermal diffusivity k with known parameters t and $q = 2\pi/\Lambda$. The damped acoustic oscillation equation is used to find the acoustic damping parameter(s) τ_i and the frequency(ies) f_i. An estimate of the strongest SAW peak frequency is calculated from a Lorentzian fit of the Fourier transform and is used in the fit as a known parameter first. The parameters A, B_i, and C are found when optimizing the fit. Figure 3-6 shows a raw signal with annotations corresponding to the two-wave TGS equation.
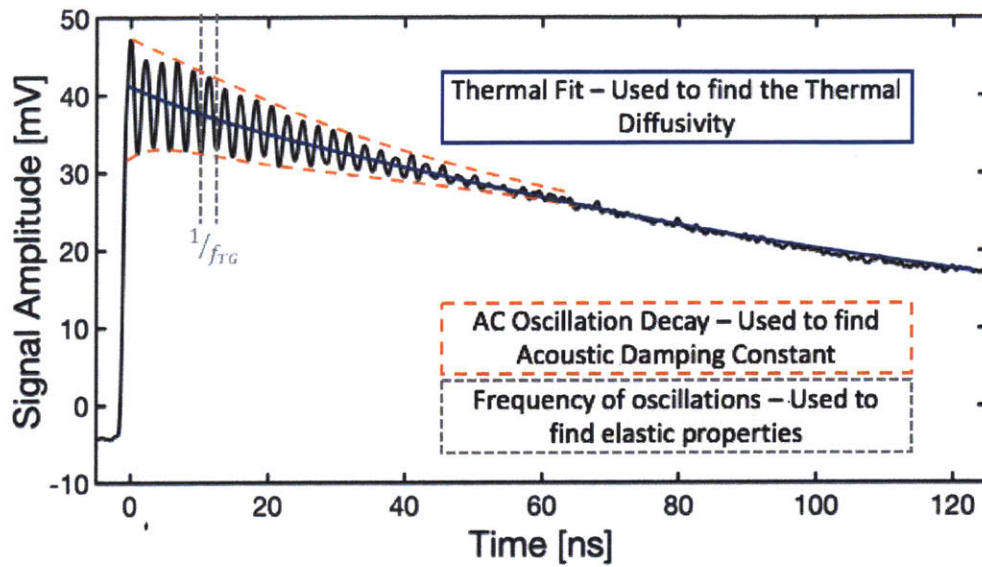
Figure 3-6: Annotated unaged CF8 CASS sample signal showing thermal fit (blue), acoustic decay, (red) and frequency of oscillations (dashed). Measurement was taken in vacuum so there is no oscillation due to waves created in air. Adapted from [19] in collaboration with Benjamin Dacus.

Chapter 4

Results

To demonstrate the usage of gigahertz, non-contact ultrasonics to monitor and evaluate the health of CASS alloys, the first step involved validating the state of aged and unaged samples using conventional materials characterization techniques (SEM and TEM). Next, impact tests of unaged and aged CASS specimens show decreased ductility via decreasing Charpy impact energy with increased aging temperature. In addition, we report observations of microstructural degradation towards thermal embrittlement via spinodal decomposition and nucleation and growth, in addition to the emergence of fracture surfaces and dislocations in thermally aged CASS in comparison to unaged specimens. Furthermore, results from microindentation show increasing hardness in the delta ferrite phase of thermally aged samples as well as at the gamma-delta interface, while results from nanoindentation show an increase in the relative stiffness of delta ferrite in comparison to neighboring austenite grains. Finally, we report the observation of a second, higher Fourier frequency via TGS measurements in thermally aged CASS in comparison to unaged specimens, which also occurs at a frequency outside of the range of predicted SAW frequencies for pristine polycrystalline CASS alloys.
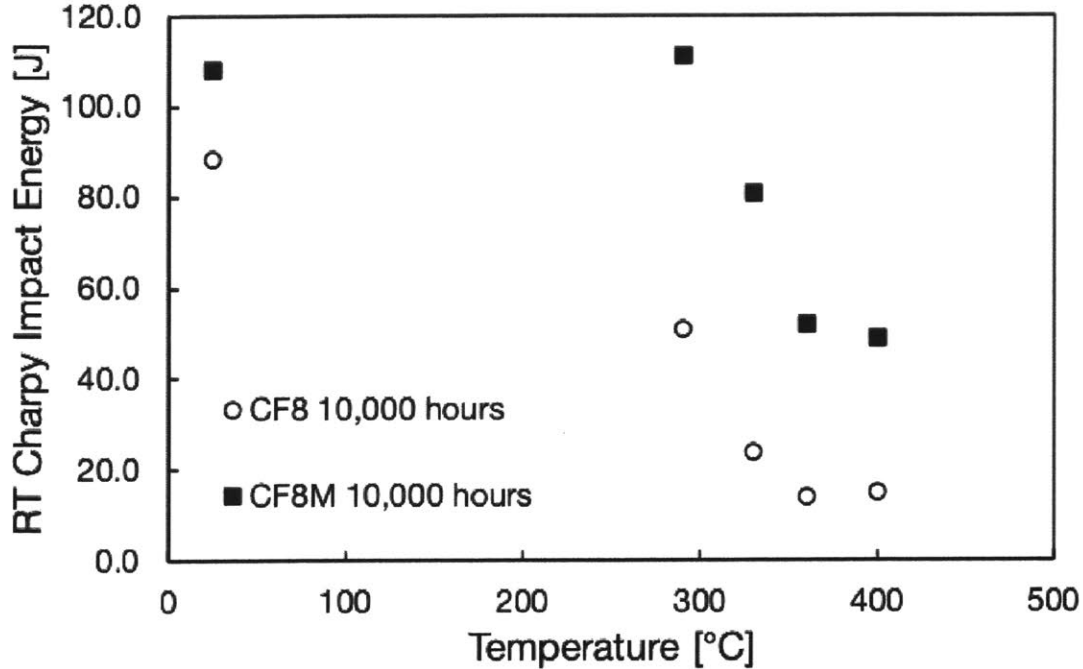
Figure 4-1: RT Charpy impact energies of CASS CF8 and CF8M samples as a function of aging temperature. (Credit: TS Byun, [47])

4.1 Charpy Impact Testing

To validate the effect of thermal aging on the ductility of CASS alloys in correlation to properties measured from TGS measurements on these alloys, impact testing was performed on CASS alloys aged for 10,000 hours with (CF8M) and without Mo (CF8) to measure Charpy impact energy. The unaged samples serve as controls to provide the upper shelf Charpy impact energy for each alloy type. Furthermore, as shown in Figure 4-1, we observe decreasing Charpy impact energy with increased aging time-at-temperature in both CF8 and CF8M specimens—confirming the loss of ductility in thermally aged CASS alloys.

4.2 Microstructural Characterization

To link the changes observed in material properties between unaged and aged CASS alloys, direct evidence of microstructural degradation in fractured Charpy specimens of CASS CF8 alloys was investigated via TEM and SEM. TEM was employed for
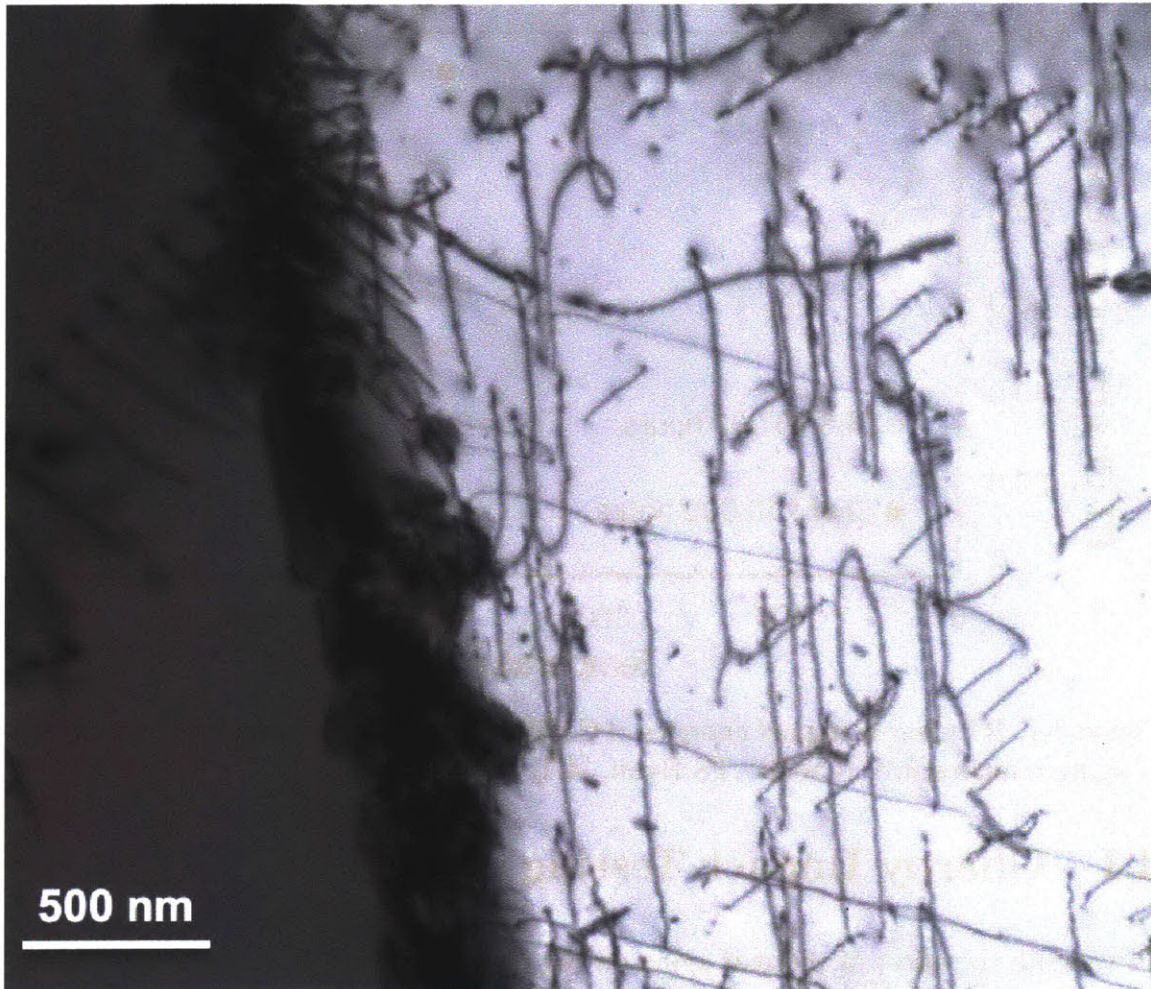
Figure 4-2: Bright-field (BF) TEM image showing the dislocation structure within the δ-ferrite in the as-received steel. Fine precipitation was also observed at the delta δ/γ interface. (Credit: M. Grace Burke, [19])

insight into the smaller features ($\leq 1\mu$m) such as the dislocation structure and the growth and nucleation of G-phase, as well as for elemental mapping of the presence and extent of spinodal decomposition in the delta ferrite phases of aged specimens. In addition, SEM was used for insight into the larger features ($\geq 1\mu$m) such as fracture surfaces associated with delta ferrite as well as the intergranular precipitation present at the interfaces between austenite and ferrite neighboring grains.
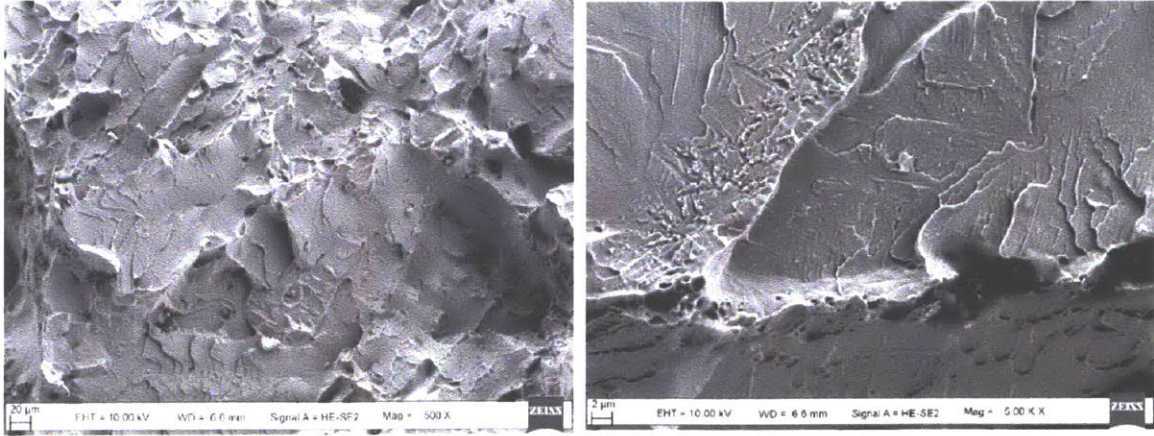
Figure 4-3: Secondary electron micrographs obtained from the fracture surface of the as-received steel. Note the cleavage fracture associated with δ-ferrite and regions of ductile failure associated with the austenite. (Credit: M. Grace Burke, [19])
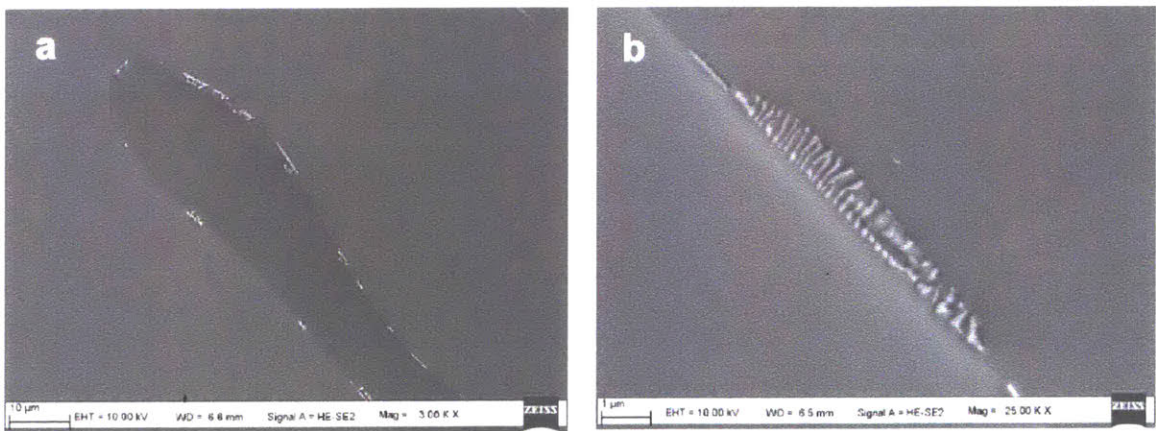
Figure 4-4: Secondary electron images of CF8 steel aged at 400°C for 10,000 h showing the extent of intergranular precipitation at the austenite-δ-ferrite boundary. Note the region of discontinuous carbide precipitation in (b). (Credit: M. Grace Burke, [19])

4.2.1 Non-aged CASS Microstructure

The microstructure of the as-received (non-aged) steel consisted of coarse austenite grains with a network of δ-ferrite. No precipitation was detected within either the δ-ferrite or the γ austenite grains. However, fine carbide precipitation was observed at some austenite-δ-ferrite boundaries (Figure 4-2). Dislocation structures were also observed within the δ-ferrite and γ austenite grains, with evidence of increased dislocation activity (and cross-slip) in the austenite in the vicinity of the δ/γ interface.
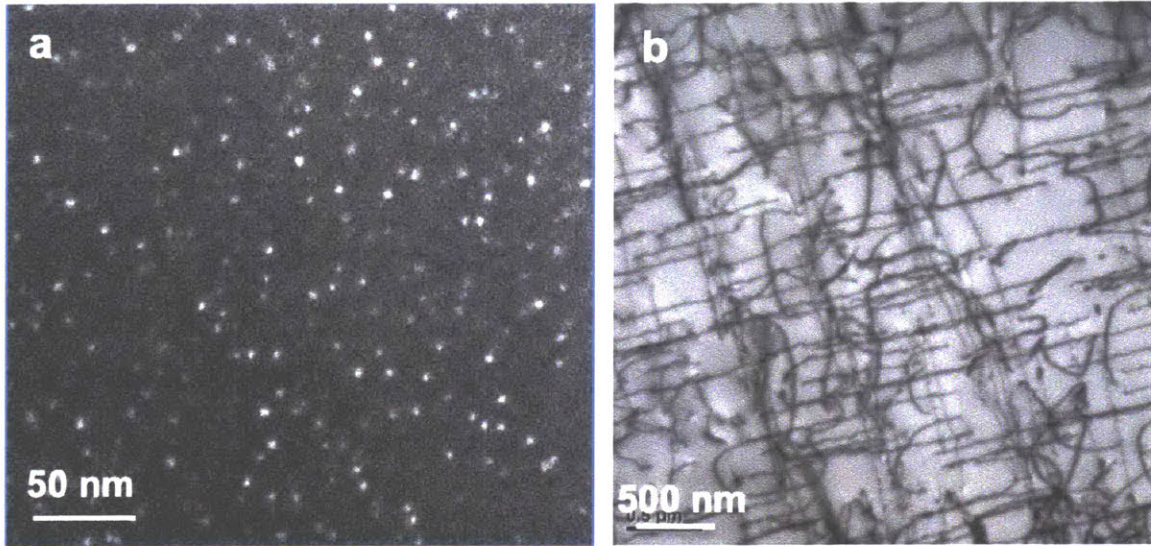
Figure 4-5: CF8 steel aged at 400°C for 10,000 hours. (a) Centered dark-field (CDF) TEM image of fine (~5 nm) G-phase precipitates in δ-ferrite. (b) Bright-field TEM image of the dislocation structure in the δ-ferrite. (Credit: M. Grace Burke, [19])
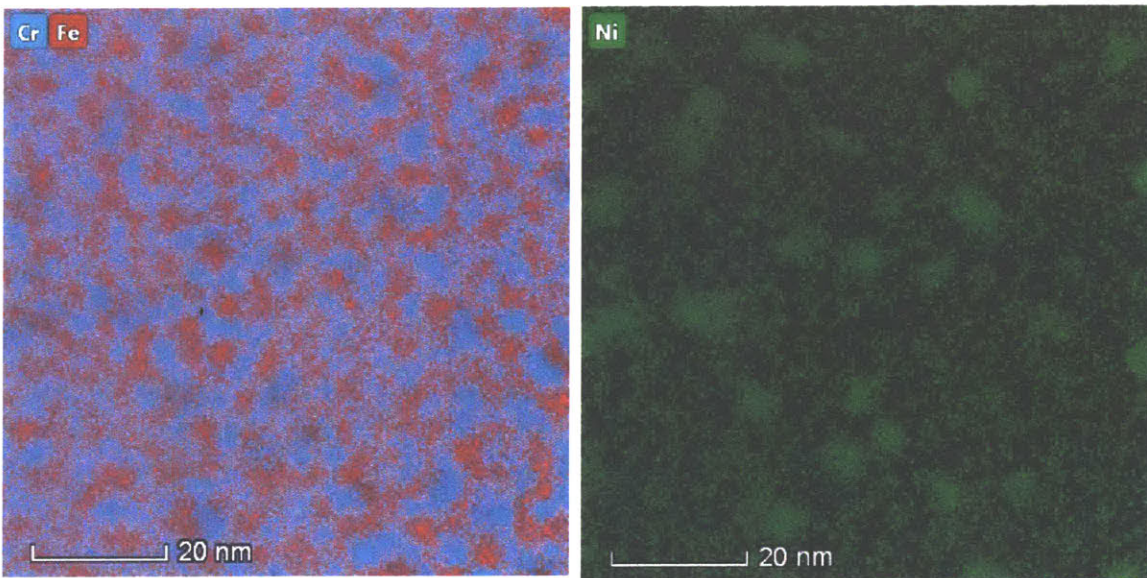
Figure 4-6: (a) Combined Cr and Fe elemental map extracted from a STEM-EDX SI data set showing the classic isotropic spinodally decomposed δ-ferrite. (b) Ni map showing the presence of the fine G-phase precipitates (Credit: M. Grace Burke, [19])

4.2.2 Aged CASS Microstructure

The fractured Charpy specimen was characterized by predominantly transgranular cleavage, with some areas of dimpled rupture. Representative examples are presented in Figure 4-3.
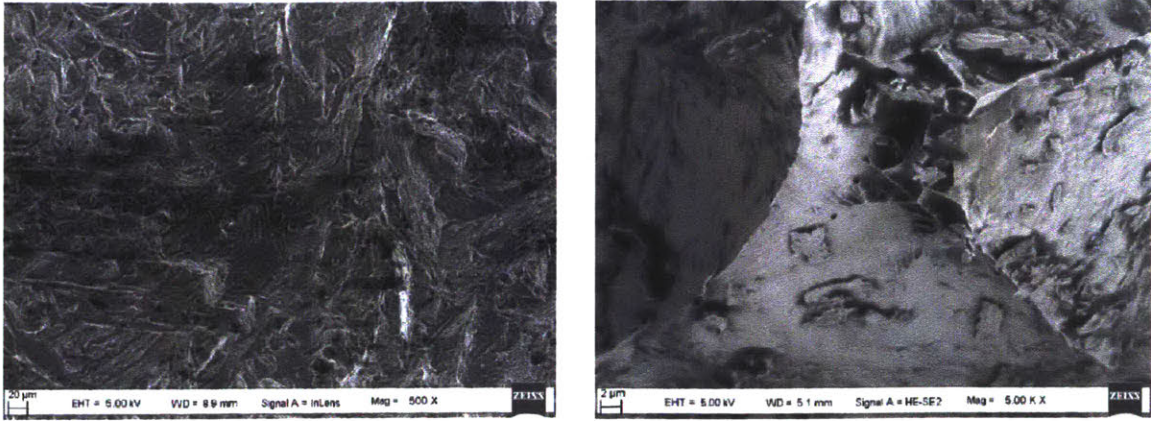
Figure 4-7: Fracture surface of CF8 aged at 400°C for 10,000 hours. Note the cleavage fracture and the presence of intergranular phases at the δ-ferrite-austenite boundaries. (Credit: M. Grace Burke, [19])
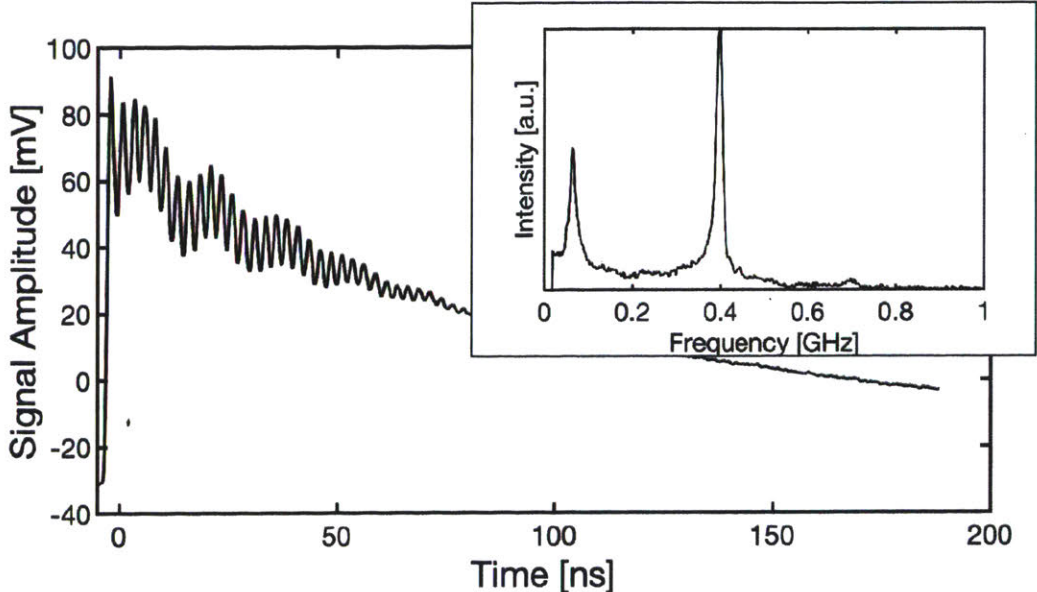
Figure 4-8: Unaged CF8 CASS control sample, raw time-domain signal and Fourier transform. Fourier frequency on low end of spectrum corresponds to pressure wave in air and corresponding oscillations can be seen in the raw signal. Adapted from [19]

Aging at 400°C produced no discernible change in the austenite; no additional precipitation was observed in the austenite. An increase in carbide precipitation at the δ/γ boundaries, Figure 4-4, with evidence of limited discontinuous $M_{23}C_6$ precipitation. Significant microstructural changes were observed in the δ-ferrite after ageing. Fine (~5 nm) G-phase (Ni silicide) precipitates were observed throughout the ferrite. In addition, STEM-EDX spectrum imaging analyses revealed that the
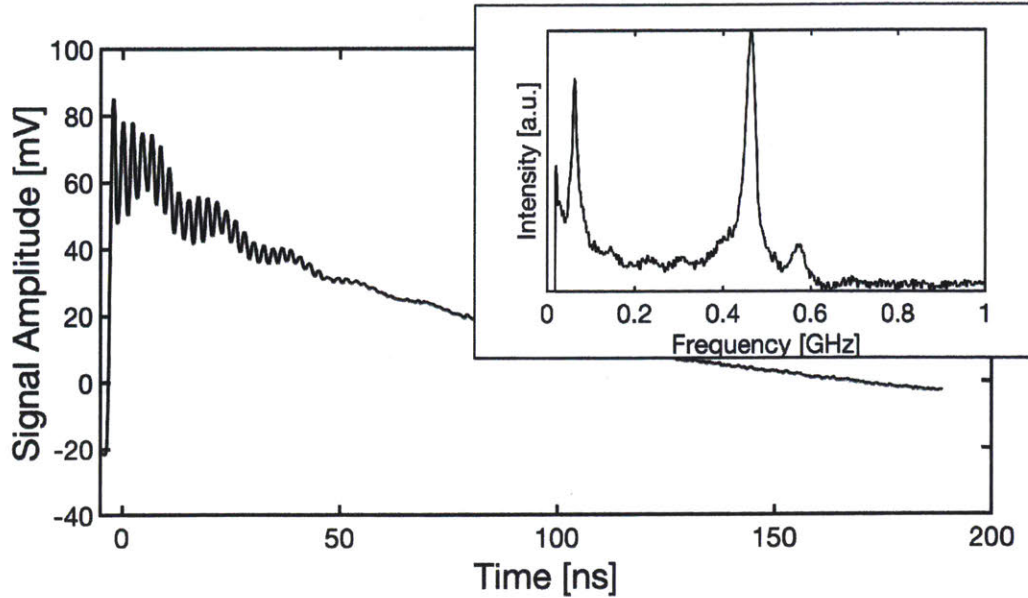
Figure 4-9: CF8 CASS Aged at 400°C for 10,000 hours, raw time-domain signal and Fourier transform. Fourier frequency on low end of spectrum corresponds to pressure wave in air and corresponding oscillations can be seen in the raw signal. Second peak, attributed to the α' phase from spinodal decomposition in δ phase, is seen emerging around 550 MHz.

δ-ferrite had decomposed into Cr-enriched α' and Fe-enriched α. This morphology of the decomposed δ-ferrite was consistent with the formation of the isotropic spinodally decomposed microstructure. Figure 4-6 shows the elemental images extracted from a STEM-EDX spectrum image dataset. The discrete Ni-regions represent the Ni-enriched G-phase precipitates.

4.3   Indentation

To link the changes in material properties between unaged and aged CASS alloys to properties measured using TGS, indirect evidence of microstructural degradation in fractured Charpy specimens of CASS CF8 alloys were investigated via micro and nanoindentation. Microindentation was used to probe the average hardness of γ and δ phases as well as the interfaces in between, while nanoindentation was used to map nanohardness and elastic modulus across grains of ferrite and neighboring austenite grains.

71

4.3.1 Microindentation

Figure 4-13 show the Vickers hardness (HV_{5gf}) in γ-austenite (Fig. 4-13-a), δ-ferrite (Fig. 4-13-b), as well as in the γ—δ interface (Fig. 4-13-c), averaged over 10 indents per phase, for CF8 and CF8M alloys aged for 10,000 and 30,000 hours as a function of aging temperature. These results show no discernible change in hardness in the austenite. In addition, excluding one outlier at 400°C, a trend of increasing hardness in the delta ferrite is also observed. Furthermore, increasing hardness is also observed in the gamma-delta interface, although the trend falls well within the statistical error of the measurement.

4.3.2 Nanoindentation

Figures 4-11 and 4-12 show images of microstructure with δ-ferrite apparent in the matrix and mapping of nanoindentation results in an inset of the micrograph. Figure 4-11 displays an unaged sample of CF8 steel, while Figure 4-12 was aged at 400°C for 10,000 hr. There is a clear contrast between the δ-ferrite and austenite grains in the nanoindentation map, showing clear differences in the hardness of the microstructure. Of interest is,the increase in contact stiffness of the δ-ferrite relative to the austenite after aging.

4.4 Transient Grating Spectroscopy (TGS)

To demonstrate that non-destructive, non-contact gigahertz ultrasonics can be used to monitor and evaluate the health of CASS alloys that serve as structural materials in LWRs, TGS was employed in air and in vacuum to characterize CASS specimens of two different chemical compositions (CF8 and CF8M, refer to Tables 2.1-2.2) that were aged for 10,000 hours and 30,000 hours at five aging conditions. A second, higher frequency emerges in the power spectrum (Fourier transform of raw TGS signal) of aged CASS alloys. Furthermore, to link the material properties measured via TGS to mesoscale properties such as ductility and hardness that serve as direct
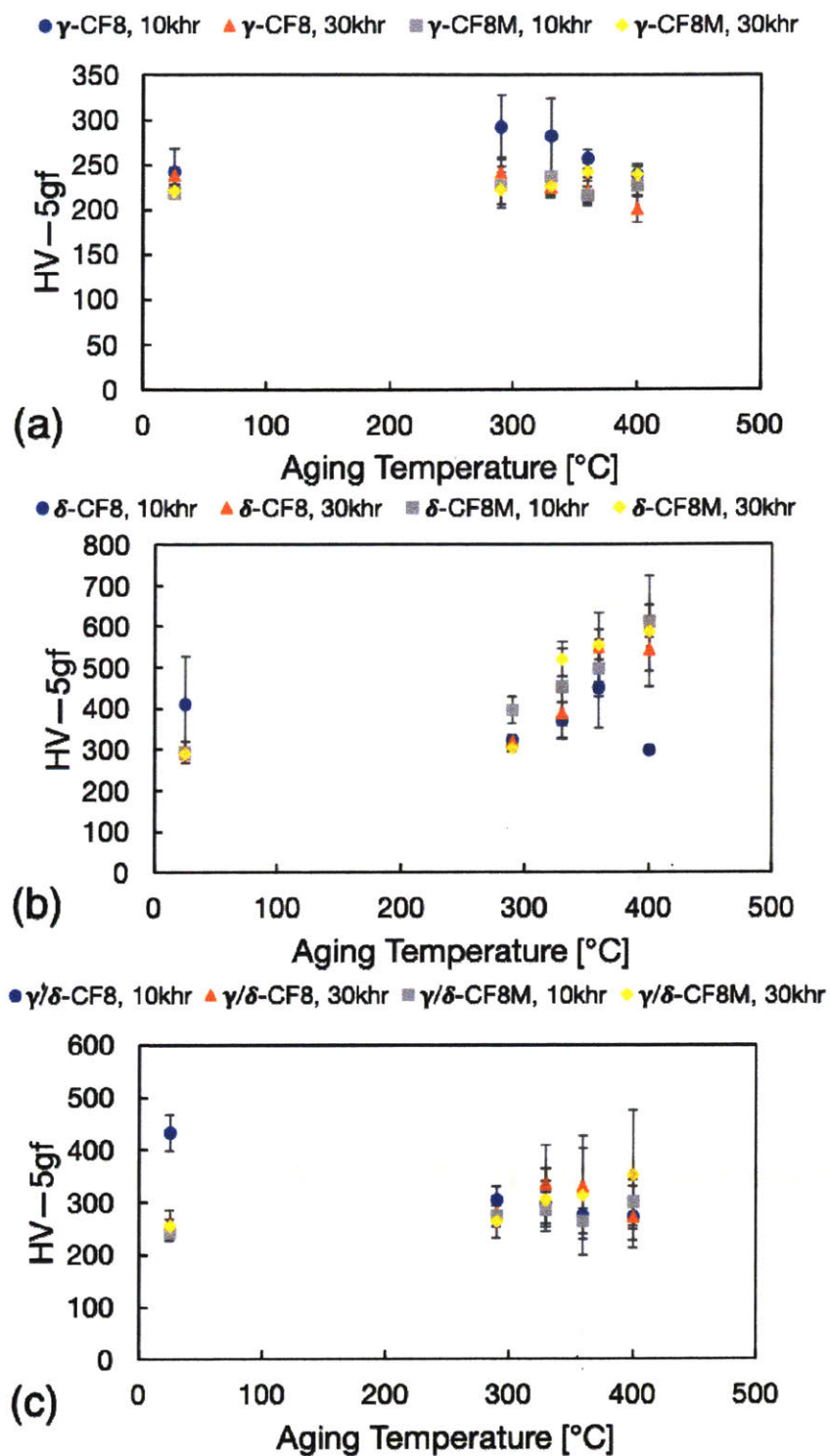
Figure 4-10: Microhardness results show no discernible change in austenite (a), increasing hardness in delta ferrite (b), and no statistically discernible trend at the gamma-delta interface (c). Errors show *one* standard deviation.
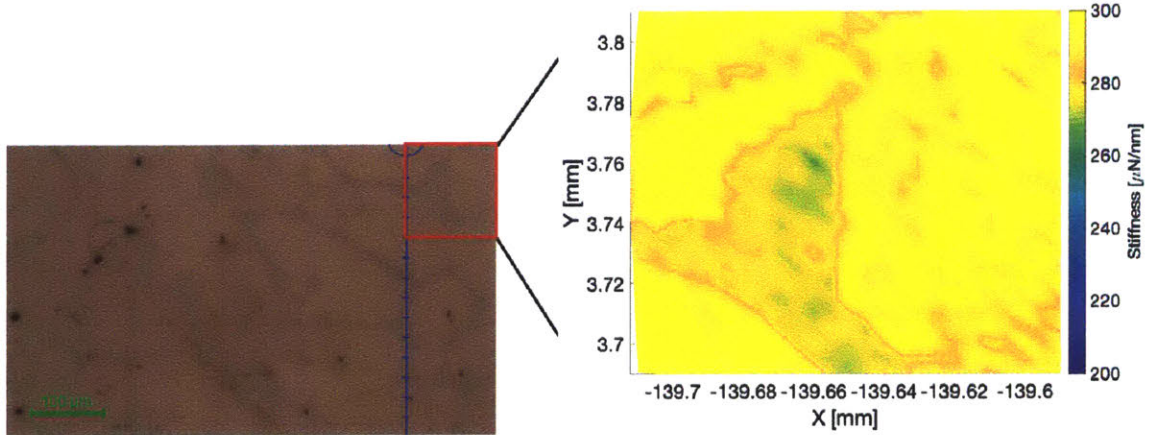
Figure 4-11: Micrograph of unaged CF8 steel showing δ-ferrite (gray) in austenite matrix (brown). The subset (scanned area) shows a stiffness map obtained via nanoindentation, showing distinct difference between the δ-ferrite grain and the surrounding austenite.
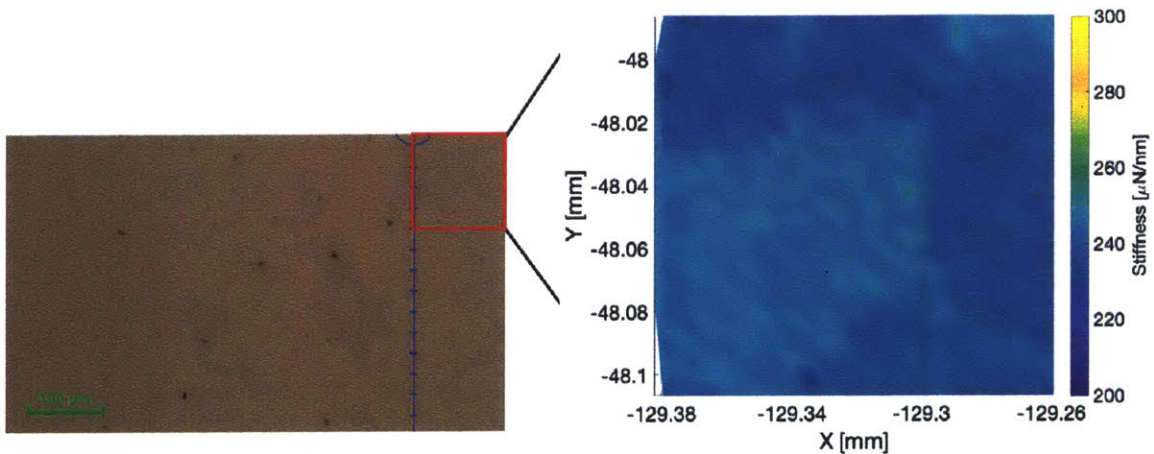
Figure 4-12: Micrograph of aged CF8 steel at 400°C for 10,000 hr showing δ-ferrite (gray) in austenite matrix (brown). The subset (scanned area) shows the nanoindentation map with δ-ferrite at a higher stiffness than the surrounding austenite.

and/or indirect evidence of microstructural degradation, the observed peak splitting in aged samples is shown to correlate with properties measured from conventional material characterization techniques. To test for the statistical significance of peak splitting in thermally aged specimens to be used as a metric to detect microstructural degradation, using known elastic properties of 304-type stainless steel, the measurable acoustic frequencies by TGS are predicted to estimate the expected variation from random crystal orientation in polycrystalline CASS alloys. In future studies, in situ TGS must be employed to deconvolve the origin of peak splitting in these materials.
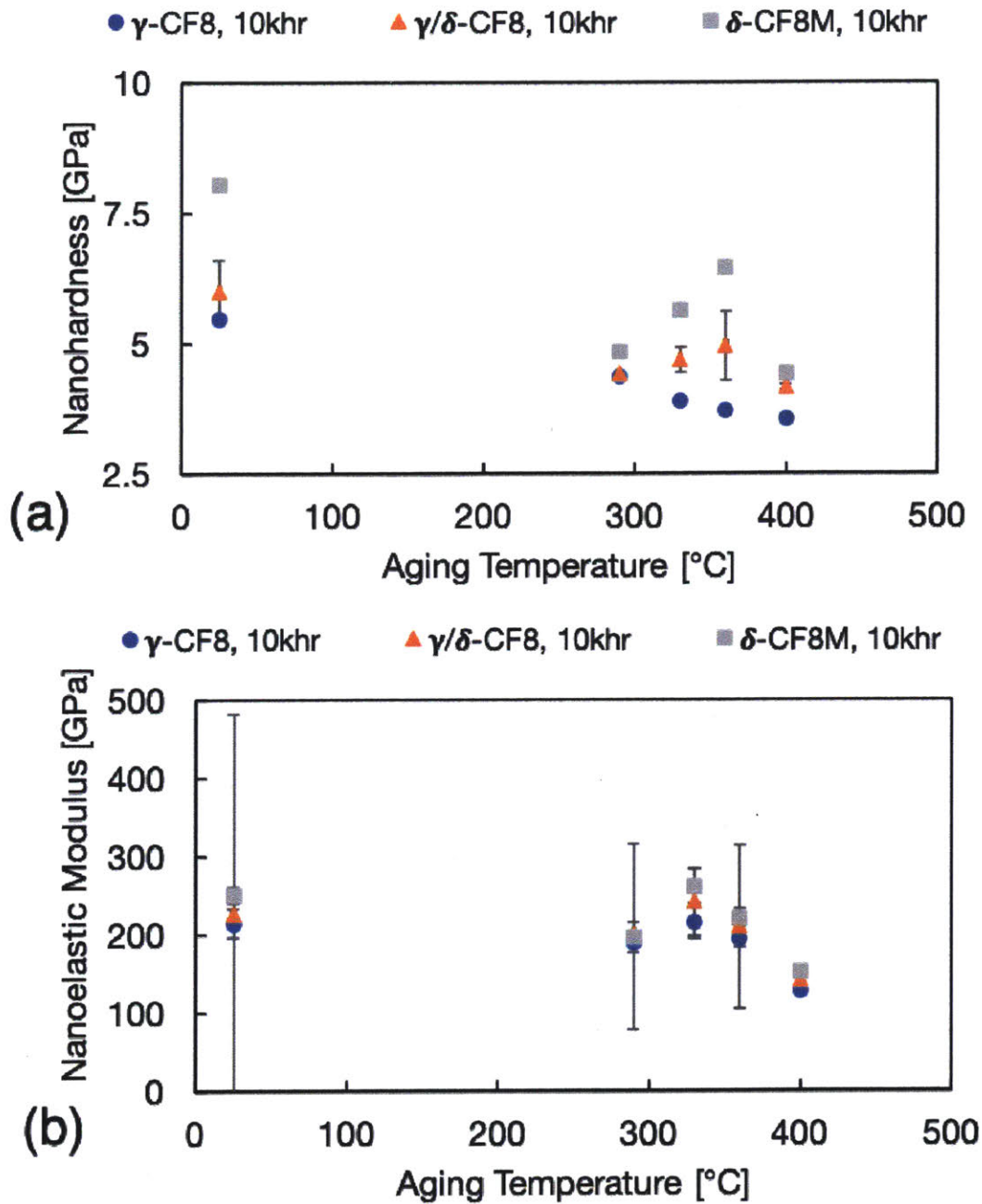
Figure 4-13: Nanoindentation results in the delta ferrite and the gamma-delta interface show increasing nanohardness between 290°C and 360°C (a) and increasing stiffness between 290°C and 330°C at the gamma-delta interface (b). Errors show *one* standard deviation.

4.4.1 TGS Measurements

Figures 4-8 and 4-9 show example TGS signals of CF8 CASS samples before and after thermal aging. Of particular interest is the difference in the Fourier transforms

of the two samples. In the unaged condition, there is a single, well defined peak at a frequency near 0.4 GHz, where in the sample that was aged at 330°C for 10,000 hours, peak splitting is observed clearly. The frequency peak near 70MHz is an air acoustic wave, due to volumetric TGS excitation of the air in front of the sample, and can be safely ignored in frequency space. Figure 3-6 shows a close-up of a signal taken from an unaged CF8 sample in vacuum that indicates the acoustic and thermal contributions. These annotations are more easily understood by referring to equation 3.9. With multiple frequencies (as in the case for the aged sample), there will be different acoustic properties based on the frequency used in the fit, which correspond to the acoustic properties of different phases that have nucleated due to aging. A proper fit to this split-peak signal will include two (or more) sinusoidal components with different frequencies, added together.

4.4.2 TGS Correlations

Various measurements were taken of SAW frequencies on CASS samples aged for 10,000 hours at 290°C, 330°C, 360°C, and 400°C. The results from all five samples are summarized in Figure 4-14. There is a clear increase in the second SAW frequency, and subsequently SAW speed, as the aging temperature increased. The second peak also consistently had a higher frequency than the first peak, which as seen in Figure 4-9 emerges after aging and the first frequency remains unchanged.

SAW frequency as a function of the Charpy impact energy is plotted in Fig 4-15. The frequency decreases with increasing impact energy, and the SAW frequency of the second peak starts at much higher frequencies than the first peak at low impact energies. This is believed to be due to spinodal decomposition of the δ-ferrite and/or the presence of G-phase, shown in TEM images of the same specimens, as previous studies have shown this phase to become harder with aging [34, 36, 38]. Nanoindentation results also show a relatively increased stiffness between the δ-ferrite and austenite phases, compared to the unaged condition, though the absolute values did decrease. Few robust correlations between nanoindentation and more macroscale properties exist, thus Vickers hardness tests of the two phases were conducted. Measuring each
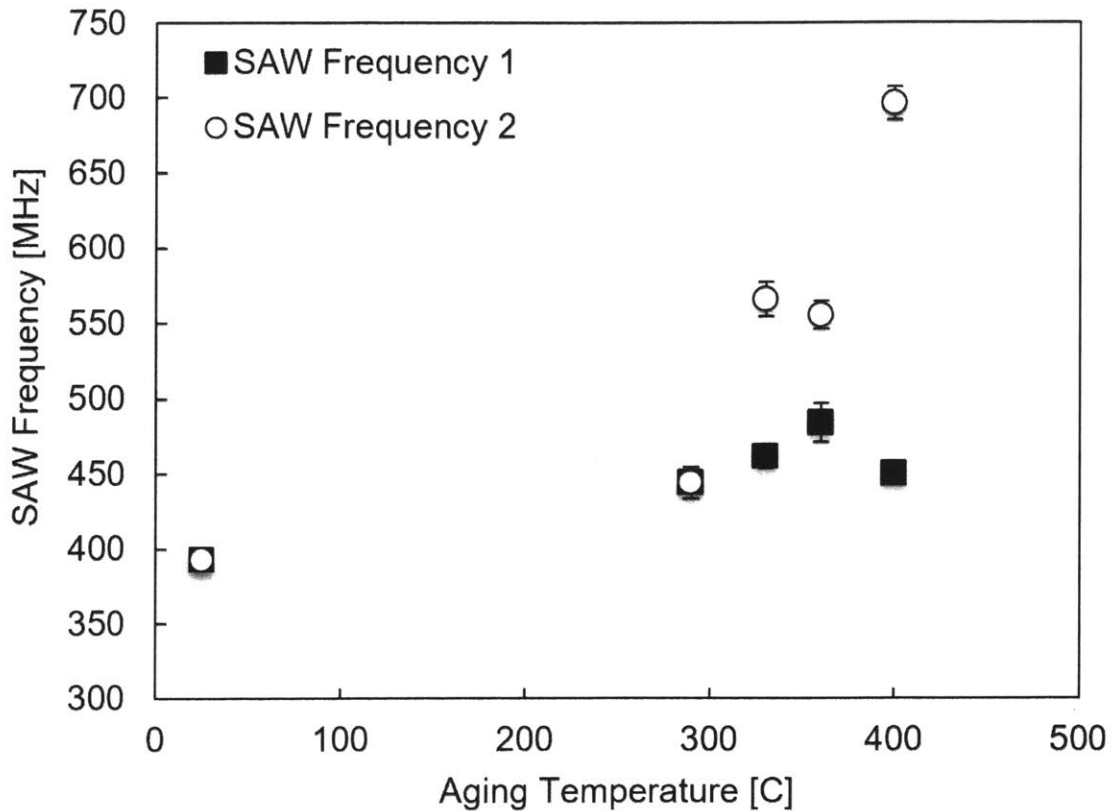
Figure 4-14: SAW frequencies vs. sample aging temperature for CF8 steels. Errors show 95% confidence intervals with statistical & measurement error added in quadrature.

phase on the 400°C aged specimen showed austenite with a hardness of $231HV_{5gf}$, and δ-ferrite with a hardness of $285HV_{5gf}$. Multiple measurements of each phase yielded exactly the same values. [38]

The difference in the two measured SAW frequencies for a given sample are plotted against the aging temperature in Figure 4-16. It is clearly shown that the largest difference in SAW frequencies is seen at the highest aging temperature with the lowest difference in frequencies at the two lowest aging temperatures. A significant, though imperfect, positive correlation exists between CF8 SAW 2nd frequency and aging temperature at 10,000 hours, while a similarly significant, though imperfect, negative correlation exists between 2nd SAW frequency and Charpy impact energy of the same materials.
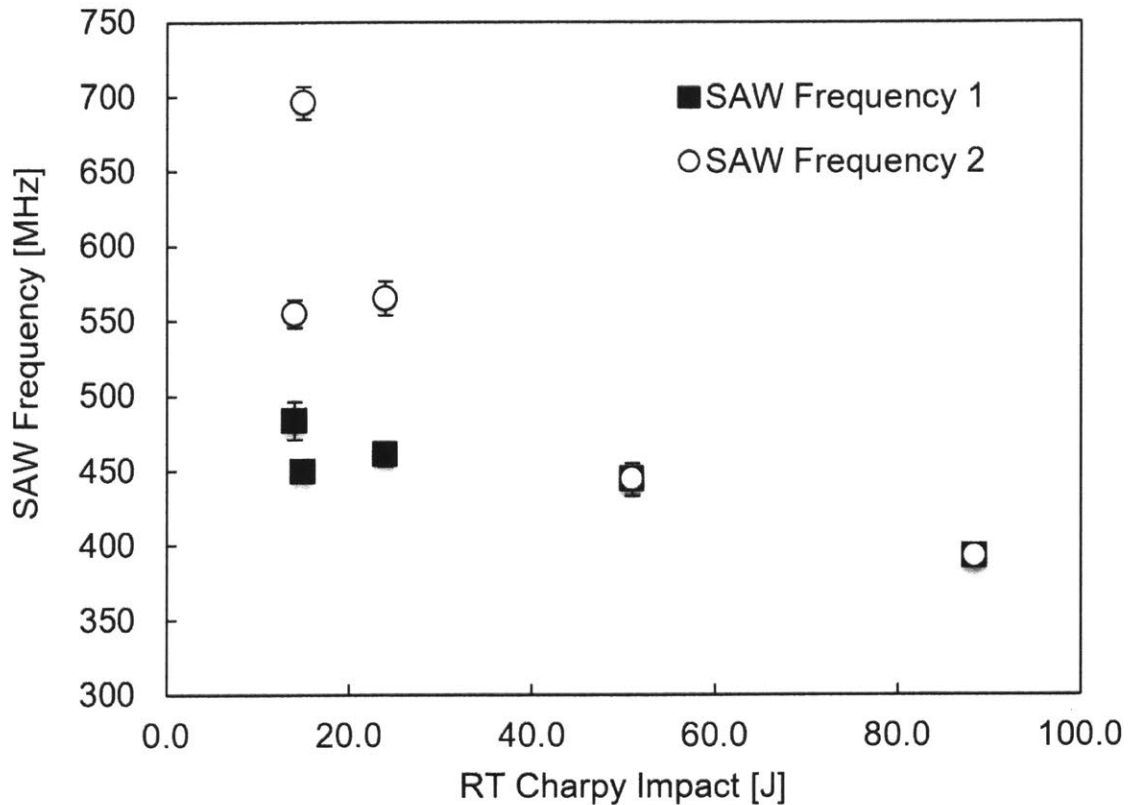
Figure 4-15: SAW frequency as a function of the RT Charpy Impact energy. Errors show 95% confidence intervals with statistical & measurement error added in quadrature.

The difference in the two measured SAW frequencies are plotted against the Charpy impact energy in Figure 4-17. There is a decrease in SAW frequency difference as the Charpy impact energy increases. Plotting this cut of the data allows for a more easily measured and interpreted metric of CASS aging, which could be rapidly implemented in the field, trained by previous Charpy coupons of the same components. It is not yet known why the second SAW frequency dips for CF8 aged at 360°C, though this merits further investigation.

Furthermore, as shown in Table 4.2 increasing delta ferrite micro/nanohardness also correlates with more double peaks, specifically above the predicted SAW/PSAW frequency range.
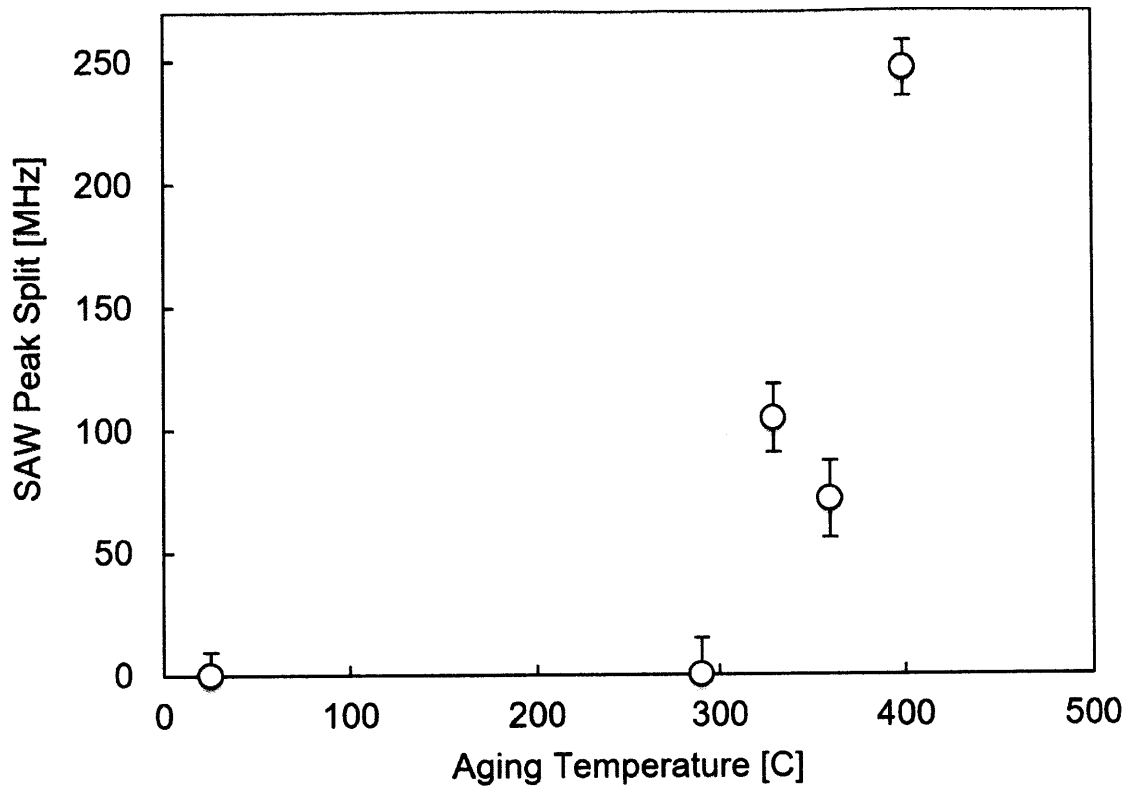
Figure 4-16: The difference in SAW frequencies as a function of aging temperature. The highest peak split was seen at the highest aging temperature. Errors show 95% confidence intervals with statistical & measurement error added in quadrature.

4.5 Summary of Results

The table below provides a summary of the results obtained in this thesis. The results advancing the primary objective of the thesis are highlighted throughout the chapter. The raw data and complete, unprocessed datasets in which these results are derived from are appended in the supplementary thesis repository—https://github.com/shortlab/SDajani Thesis
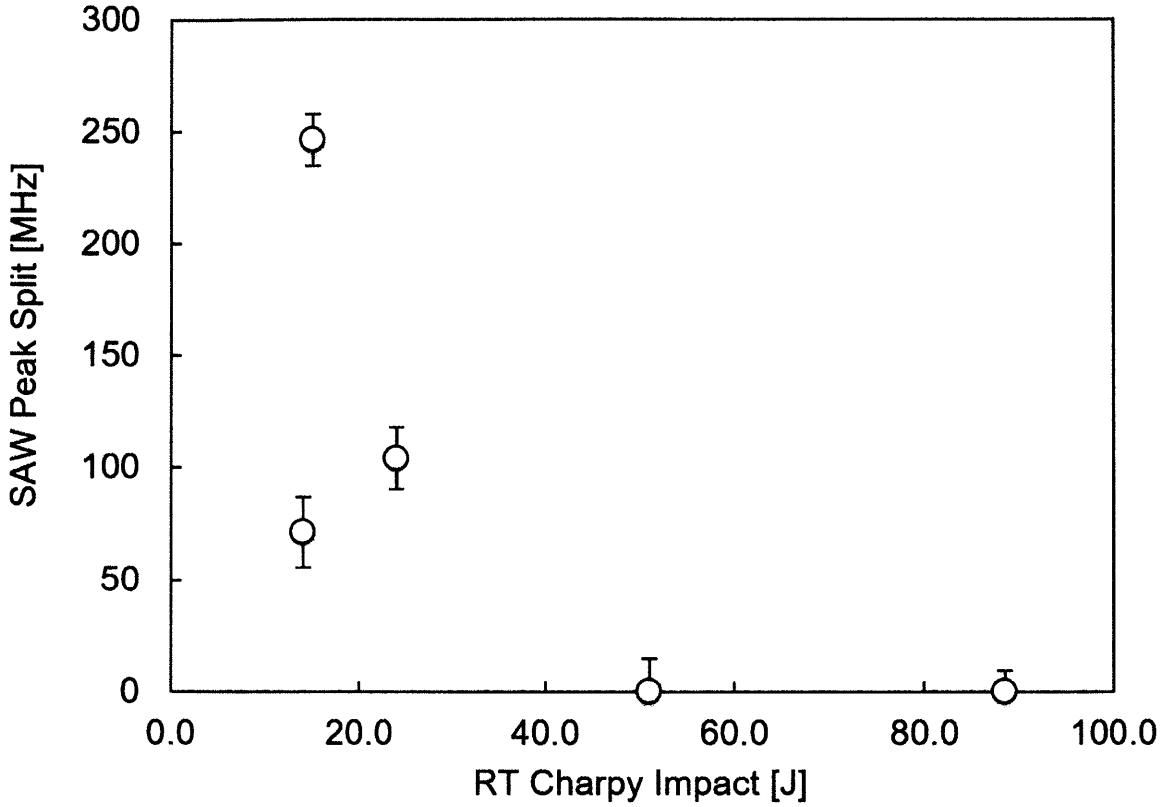
Figure 4-17: The difference in SAW frequencies as a function of RT Charpy Impact energy. The highest peak split was seen at the lowest RT Charpy Impact energy. Errors show 95% confidence intervals with statistical & measurement error added in quadrature.

Miller Indices	Surface Orientation [°]	Mode A (SAW/PSAW) [MHz]			Mode B (PSAW/Bulk) [MHz]		
		$f_{A,min}$	$f_{A,max}$	Δf_A	$f_{B,min}$	$f_{B,max}$	Δf_B
0 0 1	0	333.5625	493.578125	160.015625	443.65625	627.359375	183.703125
0 1 11	5.2	333.5625	493.578125	160.015625	443.65625	627.359375	183.703125
0 1 6	9.5	330.46875	472.140625	141.671875	378.5	888.09375	509.59375
0 1 4	14	333.78125	429.921875	96.140625	445.625	489.71875	44.09375
0 3 8	20.6	345.296875	450.046875	104.75	400.640625	707.21875	306.578125
0 1 2	26.6	333.5625	430.296875	96.734375	445.234375	490.203125	44.96875
0 3 5	31	336.921875	426.25	89.328125	425.53125	550.0625	124.53125
0 3 4	36.9	334.890625	425.53125	90.640625	436.6875	511.25	74.56250
0 5 6	39.8	345.296875	450.046875	104.75	400.640625	707.21875	306.578125
0 1 1	45	339.4375	434.03125	94.59375	415.625	599.515625	183.890625
0 5 4	51.3	336.015625	462.53125	126.515625	388.203125	796.171875	407.96875
0 3 2	56.3	333.328125	466.859375	133.53125	382.5625	833.328125	450.765625
0 5 3	59	338.984375	458.296875	119.3125	392.765625	764.53125	371.765625
0 2 1	63.4	340.828125	437.828125	97	411.515625	625.78125	214.265625
0 3 1	71.6	336.921875	426.25	89.328125	425.53125	550.0625	124.53125
0 4 1	76	338.984375	458.296875	119.3125	392.765625	764.53125	371.765625
0 6 1	80.5	332.21875	469.046875	136.828125	379.359375	851.78125	472.421875
0 12 1	85.2	331.5625	469.921875	138.359375	377.640625	862.0625	484.421875
0 1 0	90	334.890625	425.53125	90.640625	436.6875	511.25	74.56250

Table 4.1: Predicted SAW frequencies using random crystal orientation model
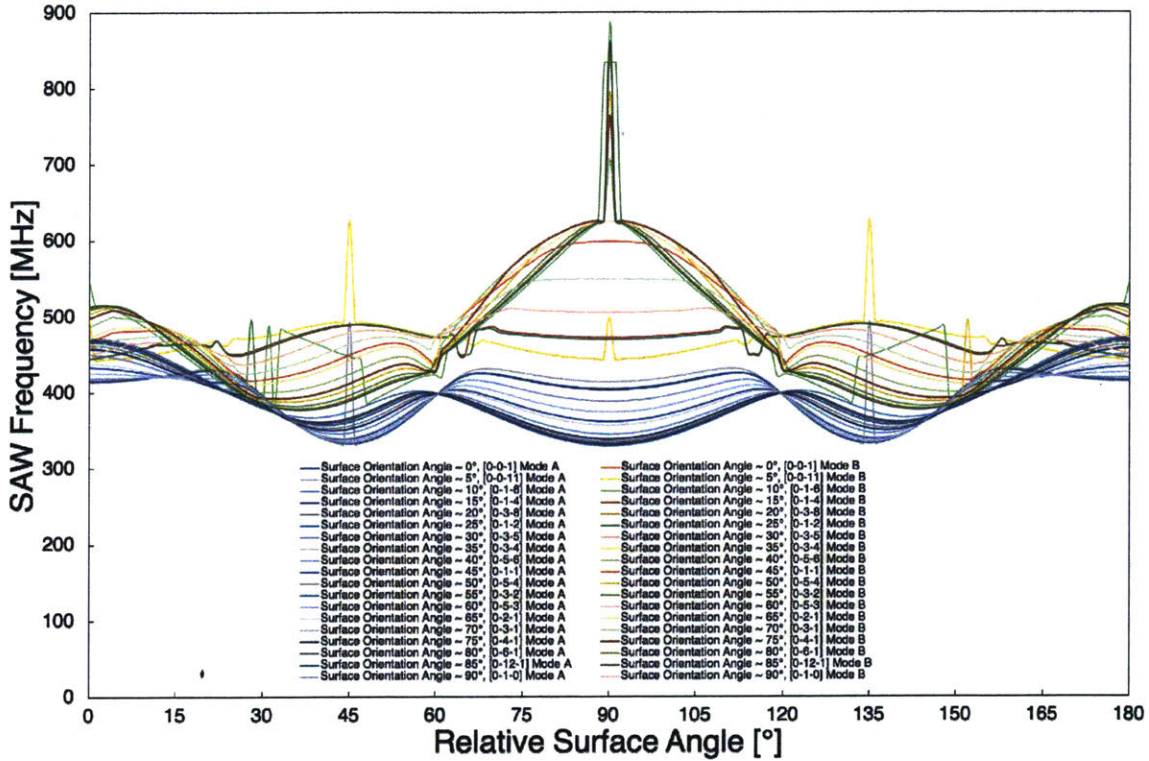
Figure 4-18: Predicted acoustic frequencies for a polarization range from 0 to $\frac{\pi}{2}$ radians ([0 0 1] to [0 1 0]) due to random crystal orientation by mode (as a function of relative surface angle) for pristine (unaged) cast austenitic stainless steel. Monochromatic lines all correspond to Mode A across polarization range (SAWs or PSAWs) across polarization range and colored lines correspond to Mode B across polarization range (PSAWs or bulk waves), according to the convention in Table 4.1

Material	Aging t [hrs]	Aging T [°C]	Charpy E [J]	HV_{5gf}			$H_{Nanoindentation}$ [GPa]			$E_{Nanoindentation}$ [GPa]			TGS [MHz]		Δf [MHz]	$N_{PeakSplits}$
				γ	γ—δ	δ	γ	γ—δ	δ	γ	γ—δ	δ	$f_{SAW,1}$	$f_{SAW,2}$		
CF8	10000	RT	88.5	241.8	432.8	411.6	5.4587	6.0031	8.0561	214.6893	225.5129	250.0311	392.8028	405.0777	12.2749	0 / 20
		290	51.0	292	305.4	322.8	4.3521	4.4075	4.8434	188.4373	200.3358	196.9983	428.9701	560.19124	131.2211	20 / 20
		330	24.0	282.2	297	372.8	3.8978	4.6796	5.6411	215.5602	241.3535	261.8765	458.2549	586.20888	127.9540	19 / 20
		360	14.0	256.4	273.4	450.8	3.7175	4.9431	6.4571	194.2134	209.7068	221.7128	393.9714	622.6641	228.6927	17 / 20
		400	15.0	239.67	273	298.33	3.5376	4.1591	4.4221	127.8649	141.8922	152.1413	422.9476	558.3030	135.3554	18 / 20
	30000	RT	172.0	237.8	256.4	289.4	3.8677	4.2265	4.5822	212.0334	218.0041	225.6055	392.3394	415.2939	22.955	4 / 20
		290	—	241	280	320.6	4.0934	4.8406	5.1693	197.4311	214.2833	233.6828	396.0573	539.6794	143.6220	13 / 20
		330	—	224.6	334.4	388.8	3.427	4.6093	6.8269	180.3304	200.1194	216.5941	425.8878	504.1179	78.2301	15 / 20
		360	—	221.4	330.4	548.2	3.6397	5.7222	8.1296	236.2415	247.9229	249.5182	417.2628	589.9955	172.7327	17 / 20
		400	—	200.4	271.4	543.2	3.2556	4.729	8.8239	157.6629	171.4683	203.9745	438.2410	568.9124	130.6714	18 / 20
CF8M	10000	RT	108.0	218.4	243.4	294.2	3.6266	4.0537	4.1949	206.3962	212.5955	216.3379	396.5723	430.1015	33.5292	5 / 20
		290	111.0	227	274.4	395.8	3.4868	4.359	4.6924	110.6120	124.3432	128.7518	365.2420	583.0716	217.8296	19 / 20
		330	81.0	236.4	286.2	452.6	3.5982	4.8477	6.5601	193.6217	209.2959	229.6803	438.6354	553.3038	114.6685	20 / 20
		360	52.0	215.2	263.6	498.2	3.3629	5.2901	7.2597	164.0427	191.4154	202.9832	358.4440	605.4952	247.0513	20 / 20
		400	49.0	227.6	299.8	612.6	3.4829	4.7155	7.8844	114.2559	125.7034	151.0821	411.8824	525.7345	113.8520	12 / 20
	30000	RT	182.0	220.8	255.2	289.4	3.7061	3.9765	4.4963	153.2134	159.4908	161.0369	435.1633	473.1605	37.9972	4 / 20
		290	—	222.2	262.8	304.2	3.5244	4.0323	4.6209	177.494	186.759	198.7247	392.4493	497.6681	105.2189	19 / 20
		330	—	226.2	305	520.2	3.6352	5.9524	7.518	115.3996	136.1421	148.0783	406.4144	574.9005	168.4860	15 / 20
		360	—	242	312.6	555.8	3.3715*	5.1568*	6.1746*	36.2605*	43.163*	46.646*	413.8366	585.3356	171.4990	20 / 20
		400	—	239.2	352.2	589	2.9663*	5.2632*	8.0088	51.5479*	64.235*	76.7935*	447.2136	559.1340	111.9204	13 / 20

Table 4.2: Summary of results

Chapter 5

Discussion

In order to establish the usage of gigahertz, non-contact ultrasonics as a reliable technique to monitor and evaluate the health of LWR structural materials, this thesis attempts to link changes in material properties observed by conventional materials characterization techniques to measurable variations in TGS measurements performed on unaged CASS alloys in comparison to specimens thermally aged at various conditions. In short, results have shown that thermally aged CASS alloys exhibit microstructural degradation by spinodal decomposition and precipitation by means of direct confirmation from TEM microanalysis, as well as a decrease in ductility from Charpy impact testing and an increase in hardness from indentation—both serving as hallmarks confirming that thermal hardening towards embrittlement due to spinodal decomposition and precipitation have indeed occurred in these specimens as a result of varying thermal aging conditions. [4, 38] The degraded CASS alloys also show a measurable difference in the frequency spectrum (referred to colloquially as the 'power spectrum') of the TGS signal when compared to unaged, control samples, which we propose to utilize as a signature to detect microstructural degradation in thermally aged alloys. Namely, in the power spectrum of thermally aged alloys, a second peak emerges in the unallowable range of the SAW frequencies predicted by elastic theory due to random crystal orientation. Although SAW 'peak splitting' is observed in both unaged and aged samples, the range of variation in SAW frequencies observed in all control samples are captured by elastic theory predictions—attributing SAW

83

peak splitting in the allowable ranges of variation predicted by elastic theory from random crystal orientation to measurable pseudo-SAW frequencies and bulk modes across grains of undegraded austenite.

However, (a) the difference in TGS signal is correlated to material properties indicative of microstructural degradation (SAW peak splitting correlated to loss of ductility and thermal hardening) and (b) since *some* of the second frequency measured in aged samples occur in the unallowable range from elastic theory predictions (due to random crystal orientation). Thus, we can deterministically conclude that SAW peak splitting in thermally aged CASS alloys cannot be explained using elastic theory alone without the growth of new phases within the area illuminated by the TGS surface grating—i.e. microstructural evolution/degradation nucleates the growth of a new phase large enough to contribute to the TGS signal. Hence, we attribute the frequencies measured in the non-allowable range of variation from random crystal orientation to microstructural degradation.

The origin of the dip at 360°C shown in Fig. 4-15 remains unclear. There may be a specific degradation mechanism specific to this aging temperature, or there may be other degradation mechanisms competing with spinodal decomposition impacting the TGS signal occurring at this temperature. This may be elucidated by further TGS measurements performed *ex-situ* and *in-situ* during thermal aging to anneal out spinodal decomposition, on pure binary Fe-Cr binary alloys (without Ni for G-phase) that only undergo spinodal decomposition, or on Alloy 690 which only undergo carbide precipitation throughout thermal aging and lack the ability to undergo spinodal decomposition or g-phase precipitation. Ultimately, this dip has not been observed as a consistent trend across all samples and across all measurements thus far (Tab. 4.2) and, thus, requires further investigation.

Furthermore, by performing z-score and χ-squared statistical tests on the number of peak splits observed in unaged versus aged samples as well as a two-tailed t-test on all frequencies measured experimentally in unaged vs aged samples, the second peak significantly appears more frequently (p-value from z-score = 0.04, p-value from chi-squared test = 0.08) and is significantly different in frequency in thermally aged

samples (p-value from t-test = 0.0015), all in comparison to counts and frequencies measured in unaged specimens, respectively. Therefore, we can statistically conclude that a unique signature of peak splitting can be attributed to thermally aged, microstructurally degraded CASS alloys, and, as supported by materials characterization results, is likely due to spinodal decomposition, as precipitation is unlikely to contribute to the TGS signal due to the small volume fraction of precipitate present in any given TGS surface grating (as supported by TEM images and microanalysis). Thus, we deterministically and statistically conclude that microstructural degradation in CASS alloys can reliably be detected via TGS in a predictive, rapid, non-contact, and non-destructive manner by probing for SAW peak splitting.

5.1 Microstructural Degradation Confirmed in Thermally Aged CASS Alloys

Microstructural degradation has been confirmed in the thermally aged CASS alloy specimens investigated in this study with three distinct methods. First, results from SEM/TEM imaging and microanalysis of both aged and unaged specimens show direct evidence of spinodal decomposition as well as g-phase and intergranular carbide precipitation. Second, the loss of ductility, evident by decreasing Charpy impact energy as a function of aging temperature, show indirectly that these alloys have undergone microstructural degradation in the form of spinodal decomposition and precipitation. [4] Third, based on micro and nanoindentation results (Fig. 5-1, the thermal hardening towards embrittlement as evident by increasing hardness as a function of aging temperature also indirectly shows that spinodal decomposition and precipitation has occurred in these thermally aged CASS alloys. [38]
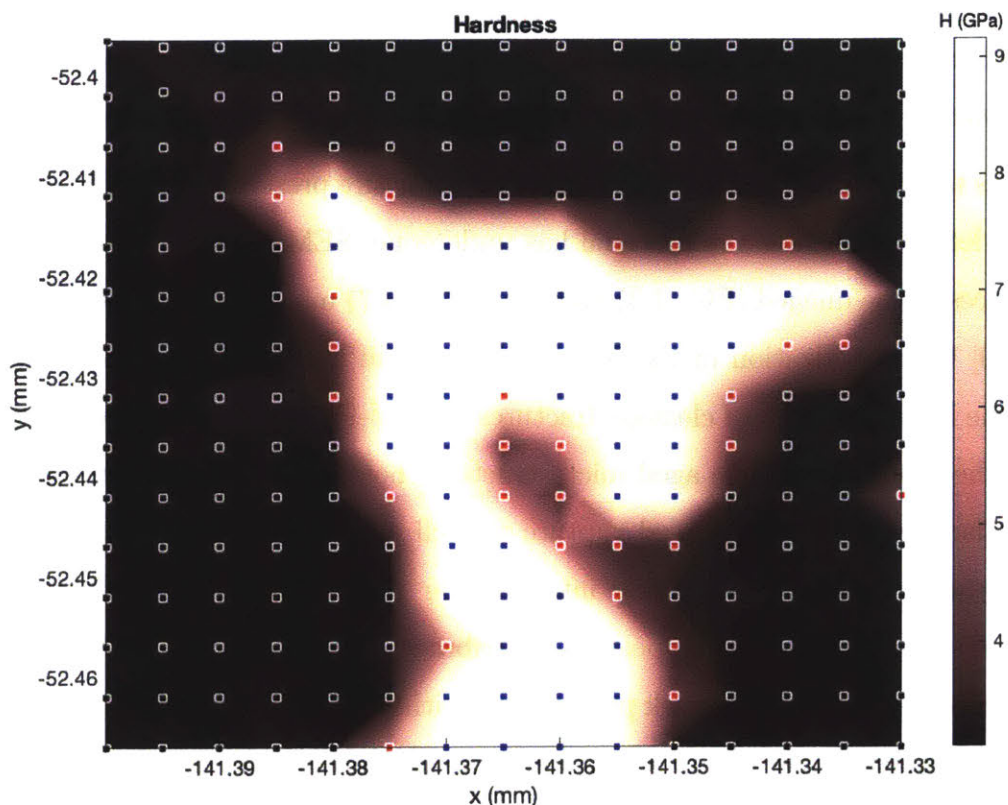
Figure 5-1: Aging at 400°C for 30,000 hours in spinodally decomposed CASS (verified by TEM as shown in Fig. 4-6) shows 3x hardening in ferrite (blue squares) vs austenite (black squares). Phases were assigned using BIC clustering method described in Section 3.3.2,

5.1.1 Microstructural Degradation in Aged Ferrite versus Austenite

Both SEM and TEM imaging as well as TEM microanalysis were performed on two CASS alloy specimens (CF8 unaged and CF8 aged at 400°C for 10,000 hours). By comparing the BF TEM images of the unaged microstructure shown in Figure 4-2 and the aged microstructure shown in Figure 4-5-b, a higher number and higher density of dislocations are found within the thermally aged δ-ferrite. The dislocation stress field uncovered in the aged microstructure facilitates spinodal decomposition in two ways. Dislocations make spinodal decomposition more kinetically favorable by allowing for faster phase separation through dislocation regions and more energetically favorable

by allowing for larger separated phase particles (i.e. Cr and Fe) at and near dislocation regions. Therefore, these two mechanisms combined allow for tilt grain boundaries to become favorable locations in CASS alloys for spinodal decomposition to occur. [108]

Next, as the fracture surfaces within the microstructure preserve an imprint of the history of deformation that the material has undergone, SEM images characterizing these surfaces in the unaged (Fig. 4-3) and aged (Fig. 4-7) microstructures were compared. [109] Characterization of the fracture surfaces in the unaged microstructure confirms the initial presence of cleavage fractures in the δ-ferrite and regions of ductile failure in the γ-austenite. The aged microstructure, however, shows the presence of transgranular cleavage and dimpled rupture as well as the growth of intergranular phases at the δ-γ boundaries. These intergranular phases, identified as discontinuous carbide precipitation [19] appear to contribute towards making the δ-γ phase boundary a better medium for crack propagation, either solely or in combination with G-phase precipitation. [34] The extent of intergranular carbide precipitation between delta-ferrite and gamma-austenite is shown in both figures 4-4-a and 4-4-b (close-up), which further support that carbide precipitation can also facilitate cracking across the δ-γ grain boundaries. (Fig. 5-2)

Furthermore, figures 4-6-a and 4-6-b provide direct confirmation of spinodal decomposition of δ-phase within the duplex ferrite-austenite alloy into Fe-enriched (α) and Cr-enriched (α') phases, characterized by a ~2-4nm spinodal wavelength. (Figures 1-2 and 4-6) In addition, figures 4-5-a and 4-6-b provide direct confirmation of G-phase precipitation within the δ-ferrite from CDF TEM images and STEM-EDX mapping of the Ni-enriched region of the spinodally decomposed specimen, respectively. [38] Ultimately, these results altogether provide direct evidence that our thermally aged CASS alloys have undergone microstructural degradation in three mechanisms: spinodal decomposition of the delta-ferrite, g-phase precipitation within delta-ferrite, and intergranular carbide precipitation along the delta-gamma-ferrite-austenite phase boundaries. Thus, these specimens are a suitable platform to link the SAW characteristics measured via TGS to the material properties associated with microstructural degradation, as characterized by conventional materials characterization

87
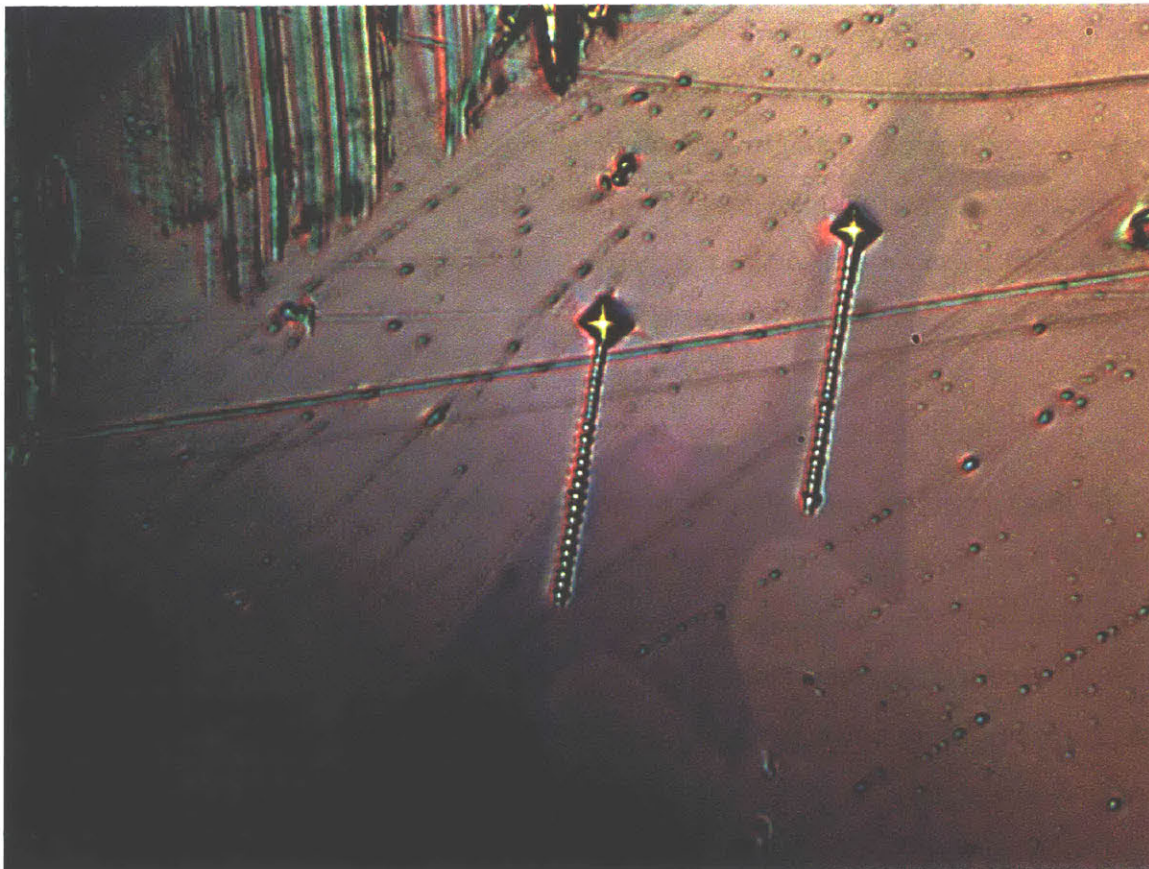
Figure 5-2: Micrograph showing two microindents applying a tensile stress to induce two cracks, a clear sign of embrittlement, (1) originating from within the gamma-austenite, propagating across the phase boundary into the delta-ferrite and (2) originating within and propagating across the delta-ferrite grain

techniques.

5.1.2 Material Property Variations in Aged Ferrite versus Austenite

Figure 4-1 show results of Charpy impact testing on CASS alloys to investigate fracture toughness, with and without Molybdenum (CF8 and CF8M), aged for 10,000 hours. The decreasing trend of Charpy impact energy indicates that these alloys are losing ductility and fracture toughness with increasing aging temperature, which is typically a hallmark of spinodal decomposition. The reduced ability for spinodally decomposed delta-ferrite to undergo plastic deformation as a result of the higher

elastic strain energy associated with the difference in atomic size between separated Fe and Cr atoms constrains the surrounding austenite matrix. Hence, decoherence between neighboring austenite and spinodally decomposed delta-ferrite lead to less ductile fractures and more cleavage fractures and delamination [110]—which is consistent with observations in the microstructural characterization results highlighted and discussed in Sections 4.1.2 and 5.1.1.

As illustrated in results from micro and nanoindentation in figures 4-13b and 3-2a, thermal hardening trends in the delta-ferrite phases of the investigated CASS alloys are correlated to the loss of ductility from Charpy impact tests—providing further indirect evidence of microstructural degradation by spinodal decomposition and g-phase precipitation. Since no statistical discernible trend in the delta-gamma phase boundary is observed, (Fig. 4-13c and Fig. 3-2a), we can rule out any hardening effects from intergranular carbides. Furthermore, given that there was no discernible change in the hardness of austenite and increasing hardness in delta-ferrite as a function of aging temperature, we can classify the mechanism of microstructural evolution/degradation as thermal hardening, attributing the increase in hardness to spinodal decomposition (growth of Cr-enriched α' phase) and g-phase precipitation. [111]

Hence, since the decrease in Charpy impact energy and increase in hardness indirectly indicate that the alloys investigated have undergone microstructural degradation, they are suitable, quantitative metrics that can be used to correlate the differences observed in SAW characteristics between unaged, pristine (non-degraded) alloys and thermally aged, degraded alloys to quantitative material properties that are indicative of microstructural degradation. In the end, the ability to link a measurable difference in the TGS signal between pristine and degraded materials enable the establishment of the technique for the monitoring and evaluation of materials in a rapid, non-destructive, non-contact, and predictive manner.

5.2 Thermal Aging Shown to Induce SAW Peak Splitting in CASS Alloys

Given that we have validated that our thermally aged samples have indeed degraded by spinodal decomposition and precipitation, we set out to link the observed changes in material properties associated with microstructural degradation to SAW characteristics as measured by TGS. When compared to control samples, the frequency spectrum of the TGS raw signal from degraded CASS alloys exhibits a unique pattern of SAW peak splitting that is correlated to material properties associated with microstructural degradation. In particular, the observed frequencies of pristine and degraded alloys are statistically different (p-value from t-test = 0.0015), and, in degraded alloys, the second peak frequency, the difference between first and second peak frequencies, and counts of observed SAW peak splitting are correlated to the decreasing ductility and increasing hardness, as observed in Charpy impact testing and indentation results performed on the same alloys.

Based on the differences in microstructural characterization between pristine and degraded CASS alloys, these observations, altogether, lead us to conclude that SAW peak splitting must be associated with microstructural degradation. We rule out the contribution of g-phase precipitation to the TGS signal given the small volume fraction occupied by g-phase in any given area illuminated by TGS ($r_{G-phase} =\sim 5$nm $\ll r_{TGS} =\sim 140\mu$m). Thus, the unique signature of TGS observed in degraded samples is attributed to spinodal decomposition.

5.2.1 SAW Peak Splitting Attributed to Spinodal Decomposition

Peak splitting after aging, as observed in Figures 4-8 and 4-9, show spinodal decomposition in the δ-ferrite. As the first SAW frequency remains unchanged, this suggests that the austenite is not undergoing any significant microstructural aging. This is supported by (a) micrographs showing no discernible change in austenite, (b) TEM

images showing the same, (c) similar Vickers hardness levels in the austenite, (d) occasional TGS signals on the aged specimens which showed only one SAW peak, and (e) variations observed in unaged specimens match the predicted SAW frequencies by elastic theory due to random crystal orientation. Because the TGS spot size is roughly 140 microns, and the austenite grain size is 1-2x that value, a few TGS analysis spots resided entirely or almost entirely within randomly-oriented austenite grains.

We attribute the second SAW frequency and, thus, the aging temperature-induced SAW peak splitting to spinodal decomposition of the δ-ferrite, as (a) evidenced directly by TEM images, indirectly by (b) hardening observed in analysis of micro/nano indentation results, (c) loss of ductility observed directly from Charpy impact test results, (d) second peaks emerges in the unallowable range by elastic theory predictions due to random crystal orientation, and (e) second peak appears more frequently in thermally aged samples. We expect the small volume fraction of precipitates, as observed by TEM, in any given TGS spot size to negligibly contribute to the TGS signal. However, because a grain of spinodally decomposed grain of delta ferrite will include two phases, α and α', we attribute the second, faster peak to the harder α', Cr-enriched Fe-phase since the increase in hardness will decrease the overall attenuation of the signal throughout the material, and, thus, we can expect to measure a higher frequency contribution from the degraded α' phase.

5.2.2 Unique Elastic Frequencies Correlated to Spinodal Decomposition

To start, a two-tailed students t-test was performed on all the SAW frequencies measured in thermally aged, degraded specimens vs unaged control samples. As shown in Figure 5-4, a p-value of 0.0015 was calculated, showing that the variation in elastic frequencies between aged and unaged CASS alloys measured via TGS cannot be a statistical artifact from measurement error. Furthermore, by employing predictive techniques, we can resolve the frequency spectrum even further to identify portions

of the frequency spectrum that uniquely belong to degraded samples and may be attributed to the microstructural features associated with degradation.

Hence, given that we know that our aged specimens have undergone spinodal decomposition, the working hypothesis regarding this statistical result is that the unique elastic frequency spectrum observed in degraded CASS alloys is a result of spinodal decomposition. Namely, in a 140 micron spot size illuminated by TGS, 5nm particle size of g-phase at a small volume fraction is unlikely to contribute to the TGS signal; however, a sinusoidal spread of Cr-enriched delta-ferrite is expected to vibrate at a different elastic frequency when illuminated by TGS than neighboring Cr-depleted regions of the same illuminated grain of delta-ferrite—as shown in Figure 5-3.

Next, as shown in Figure 5-5, a gross count of the number of SAW peak splits observed per TGS spot is correlated strongly with aging time-at-temperature, which has already been shown to correlate with microstructural degradation in the form of spinodal decomposition in these materials (by loss of ductility and thermal hardening) throughout section 5.1 and 5.2-5.2.1. This suggests that SAW peak splitting can be used to monitor the microstructural evolution of materials in general, and detect spinodal decomposition in this class of alloys in particular. Hence, a measurable difference in the frequency spectrum of the TGS signal in degraded CASS alloys in comparison to unaged specimens was identified and correlated to loss of ductility and hardening as a result of thermal aging, alluding to a difference in elasticity between both sample sets—we attribute this difference in elasticity measured via TGS to spinodal decomposition.

5.3 Growth of α' spinodal phase may explain SAW peak splitting

SAW peak splitting was observed in both unaged and degraded CASS alloys. In the case of unaged CASS, multiple peaks are fully explained with elastodynamic theory.
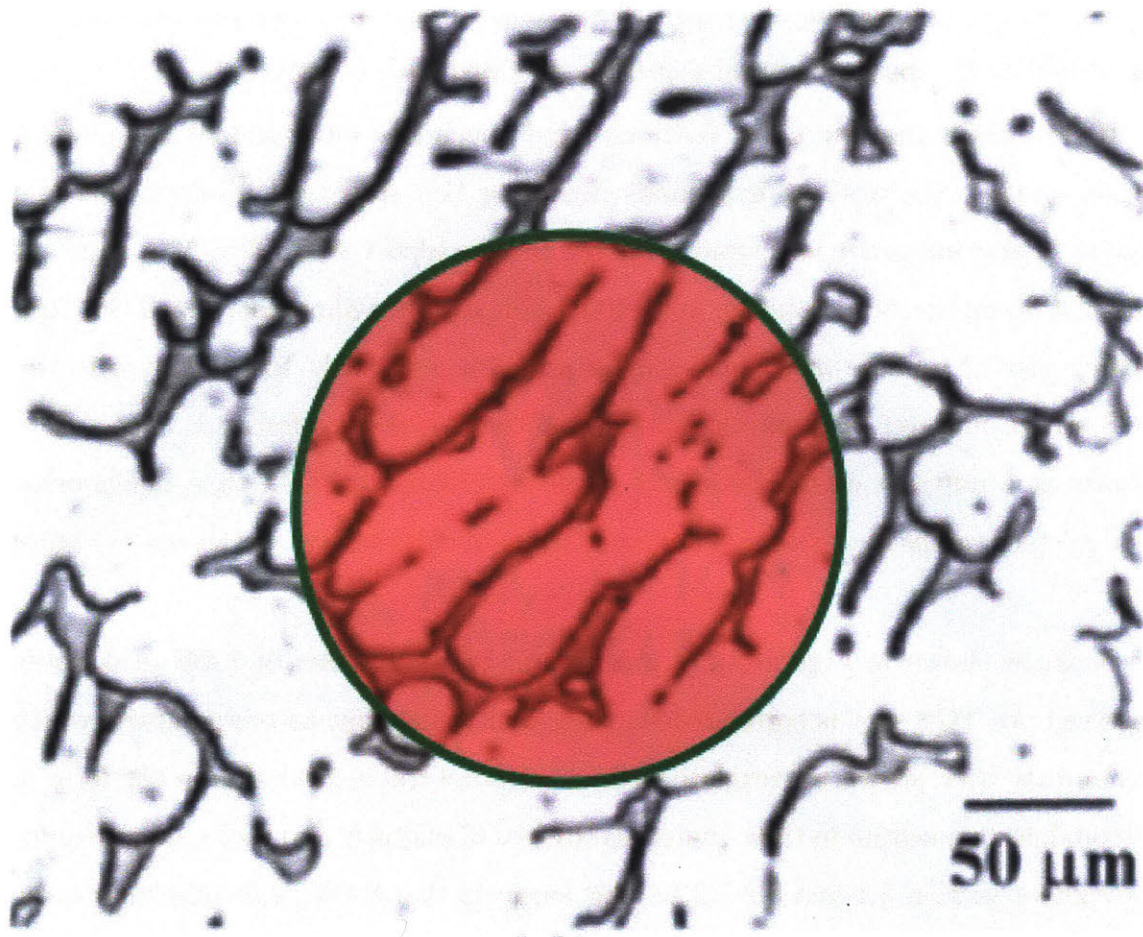
Figure 5-3: Microscale diagram showing the length scales involved in detecting spinodal decomposition at a distance, illustrating how different phases vibrate at different frequencies within the spot illuminated by TGS. The overlaid annotation shows the TGS spot size in comparison to the microstructure analyzed.

Two (or more) austenite grains that reside within the same TGS spot with different crystallographic orientations or at different relative surface angles with respect to the incoming beam will elastically vibrate at different frequencies when illuminated by TGS. This is supported by model predictions shown in figure 5-7, in which the variation in SAW frequency is captured in the ranges annotated on 5-8.

However, in the case of degraded CASS, a significant portion of the SAW frequencies measured falls within a range *unallowed* by elastodynamic theory, roughly between 0.63 and 0.83 GHz. Thus, random crystal orientation cannot explain SAW peak splitting alone. This leads us to conclude that SAW peak splitting as a phenomenon observed in CASS alloys cannot be fully explained without the growth of
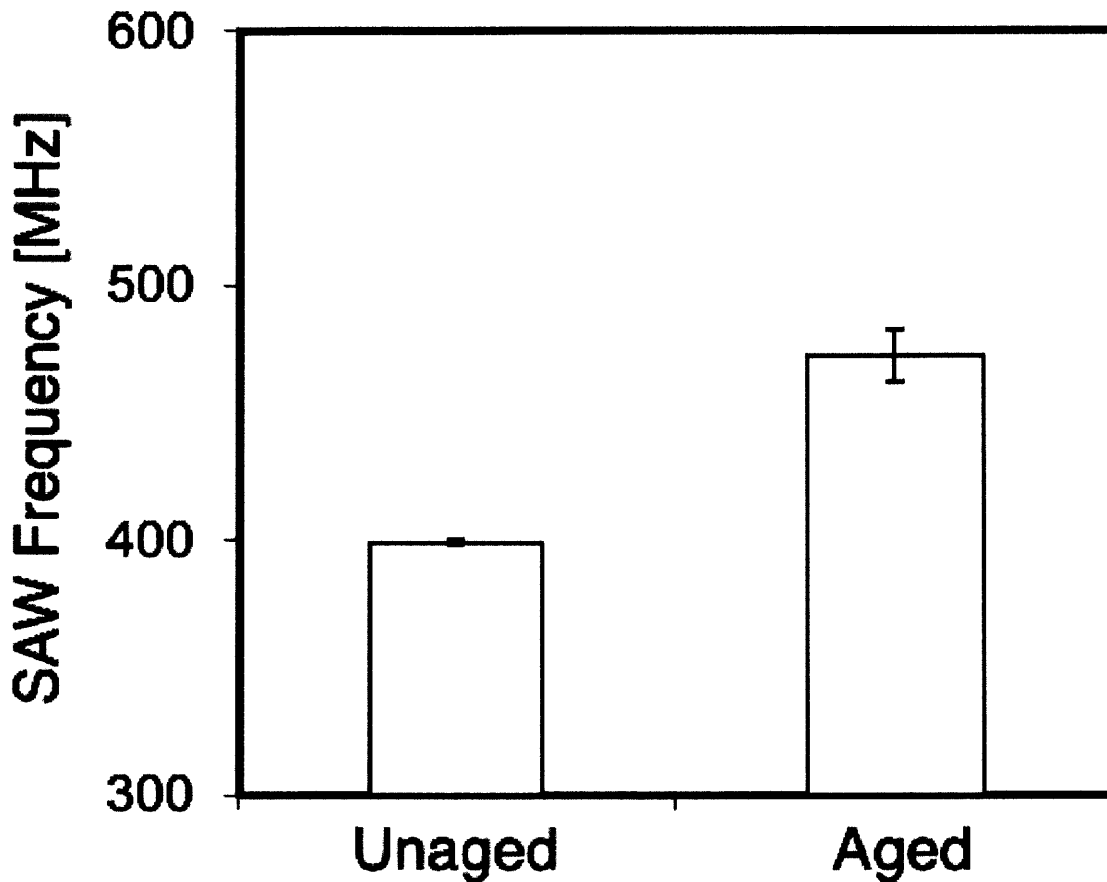
Figure 5-4: Two-tailed student's t-test performed on SAW frequencies measured in unaged vs aged CASS alloys shows a significant statistical difference between both populations, with a p-value of 0.0015 $\sim 10^{-3}$. Errors show 95% confidence intervals.

new phases. In other words, a spinodally decomposed grain of delta ferrite contains both a Cr-enriched Fe phase (α') and Cr-depleted Fe phase (α), such that the α'-phase exhibits (elastic) SAW characteristics similar to monocrystal Cr and the α-phase to exhibit (elastic) SAW characteristics similar to 304-type stainless steel, which is very similar in nature to the range of variation predicted in single crystal Fe as well. Furthermore, this is supported by the fact that elastodynamic modelling of the SAW frequencies in single crystal Cr correspond to the range unallowed by elastodynamic theory in CASS alloys.

To test for the statistical significance of this hypothesis, z-score and chi-squared
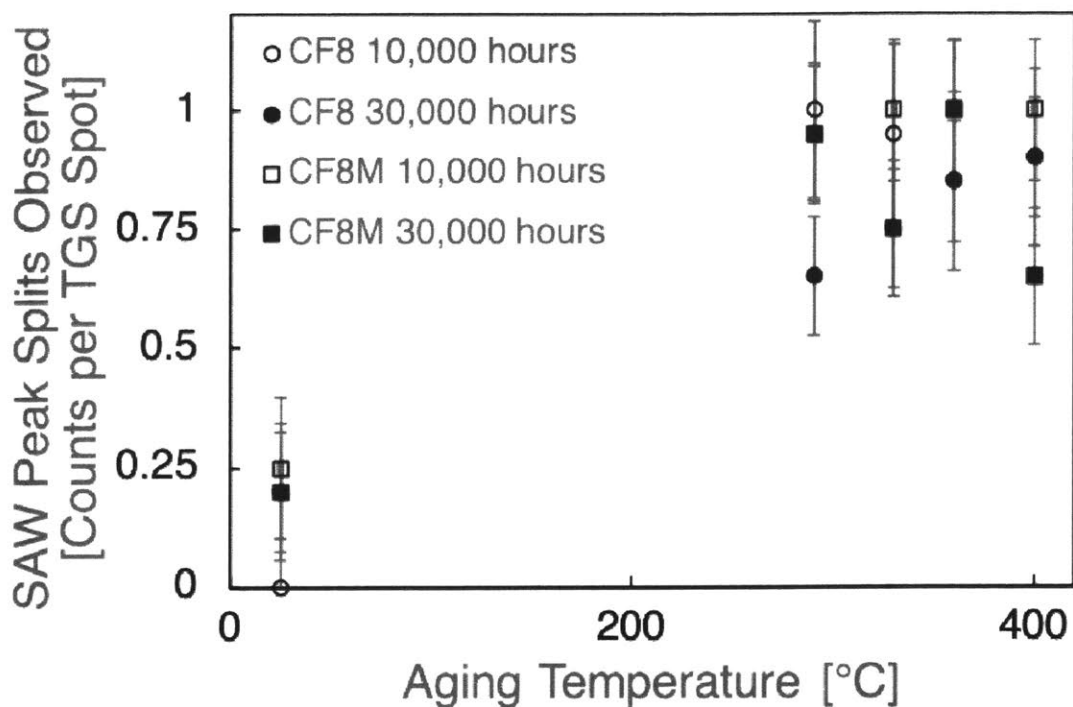
Figure 5-5: Fraction of SAW peak splits observed in degraded CASS alloys per TGS spot strongly correlated to aging time-at-temperature. Standard error shown to estimate standard deviation as count rate subject to Poisson error.

statistical tools are employed. The average number of peak splits observed in control, unaged specimens, normalized by number of scans, is taken as the expected number of peak splits due to random crystal orientation as predicted by elastodynamic theory—serving as the null hypothesis. The average number of peak splits observed in degraded, thermally aged specimens, normalized by number of scans, is taken as the observed number of peak splits due to microstructural degradation (attributed to spinodal decomposition)—serving as the alternative hypothesis. With a p-value of 0.04 from z-score statistics and 0.08 from chi-squared statistics, the null hypothesis attributing SAW peak splitting beyond the range of SAW frequencies predicted by elastodynamic theory is rejected with 92-96% confidence. Ultimately, the elastodynamic theory predictions that attribute the unique elastic frequency spectrum observed in degraded alloys to spinodal decomposition are always correlated with microstructural imaging and microanalysis via SEM/TEM, and also always corre-

lated with the loss of ductility and thermal hardening observed from Charpy impact testing and nanoindentation results—leading us to conclude that SAW peak splitting between 0.63-0.83 GHz is uniquely attributed to spinodal decomposition and can be used for the non-destructive detection of spinodal decomposition at a distance.

5.3.1 Random crystal orientation model accounts for SAW peak splitting in unaged CASS alloys

Figure 4-18 shows the range of frequencies predicted by elastodynamic theory in 304-type stainless steel (similar in composition to CF8 and CF8M). In this figure, mode A corresponds to SAW and PSAW frequencies and mode B corresponds to PSAW and bulk wave frequencies, as annotated in 5-6 with selection algorithm and model explained in section 3.4.1. To arrive at the range shown in Figure 5-7, delta functions that correspond to bulk wave acoustic modes at exact relative surface orientations are removed since they cannot be measured using the ± 5 degree precision of our TGS system. By plotting a histogram of all SAW frequencies observed experimentally in the CF8 and CF8M alloys investigated in this study, as shown in 5-8, we can capture the variation in SAW frequency due to random crystal orientation in aged, degraded samples as well as unaged.

5.3.2 SAW peak splits measured in spinodally decomposed samples inconsistent with random crystal orientation model

Note the range of unallowed frequencies in Fig. 5-7 between 0.63 and 0.83 GHz. By comparing this with the spread plotted in the histogram shown in 5-8, a unique pattern of SAW peak splitting is unveiled in the degraded, aged samples such that no SAW frequencies measured in unaged specimens are present in the unallowed range (shaded region in Fig. ??. These results indicate that the variation in SAW frequencies observed experimentally in degraded CASS shows that SAW peak splitting cannot
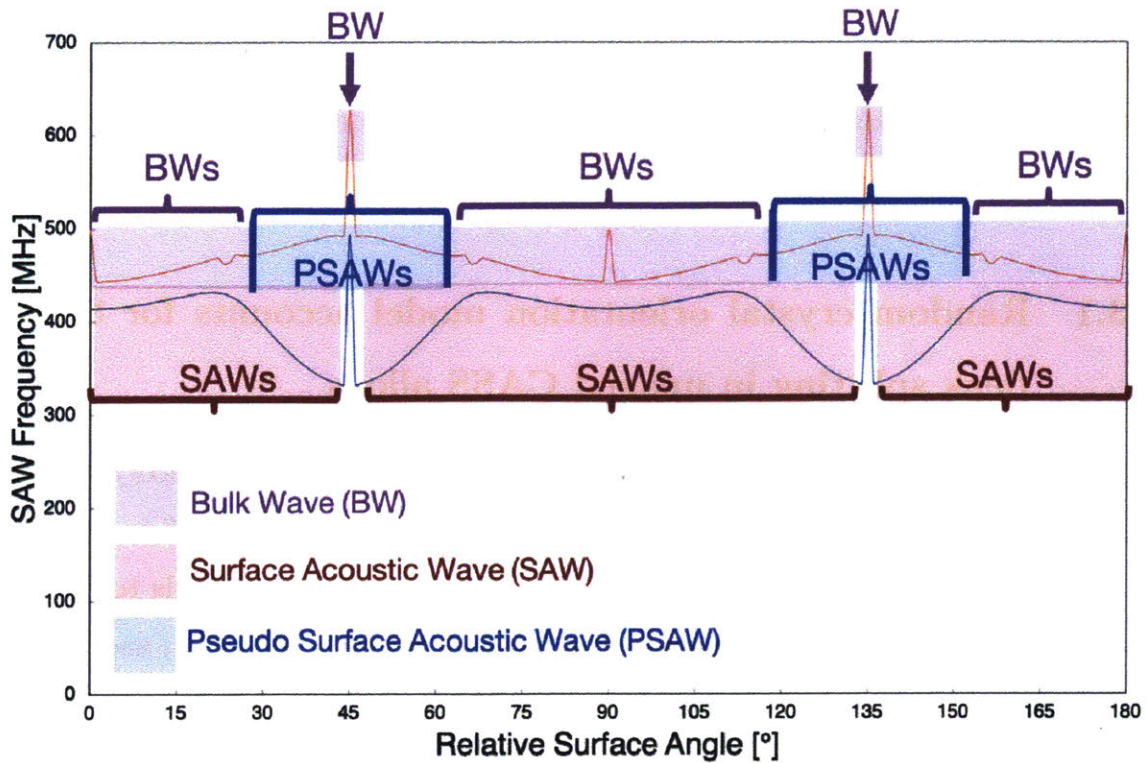
Figure 5-6: Predicted acoustic frequencies for a [001] 304-type stainless steel crystal (as a function of relative surface angle) for pristine (unaged) cast austenitic stainless steel. Here, the various acoustic modes are annotated as SAWs, PSAWs, or bulk waves to show our methodology of arriving at Figure 5-7 from 4-18. Annotations and mode assignments completed in collaboration with Cody A. Dennitt.

be *solely* attributed to randomly oriented crystals of CASS alloy. Furthermore, our hypothesis that the unique elastic frequency spectrum observed in degraded CASS alloys may be attributed to spinodal decomposition is supported by (1) higher frequency of SAW peak splits observed in degraded CASS alloys (Fig. 5-5) as well as the fact that (2) the distribution observed in degraded alloys is significantly different from unaged CASS (Fig. 5-4, p-value=0.0015).

5.3.3 Distinct SAW frequency (second peak) emerges more frequently in spinodally decomposed CASS alloys

By performing a z-score statistical test on the fraction of SAW peak splits observed in degraded vs control specimens, we can conclude that SAW peak splits significantly
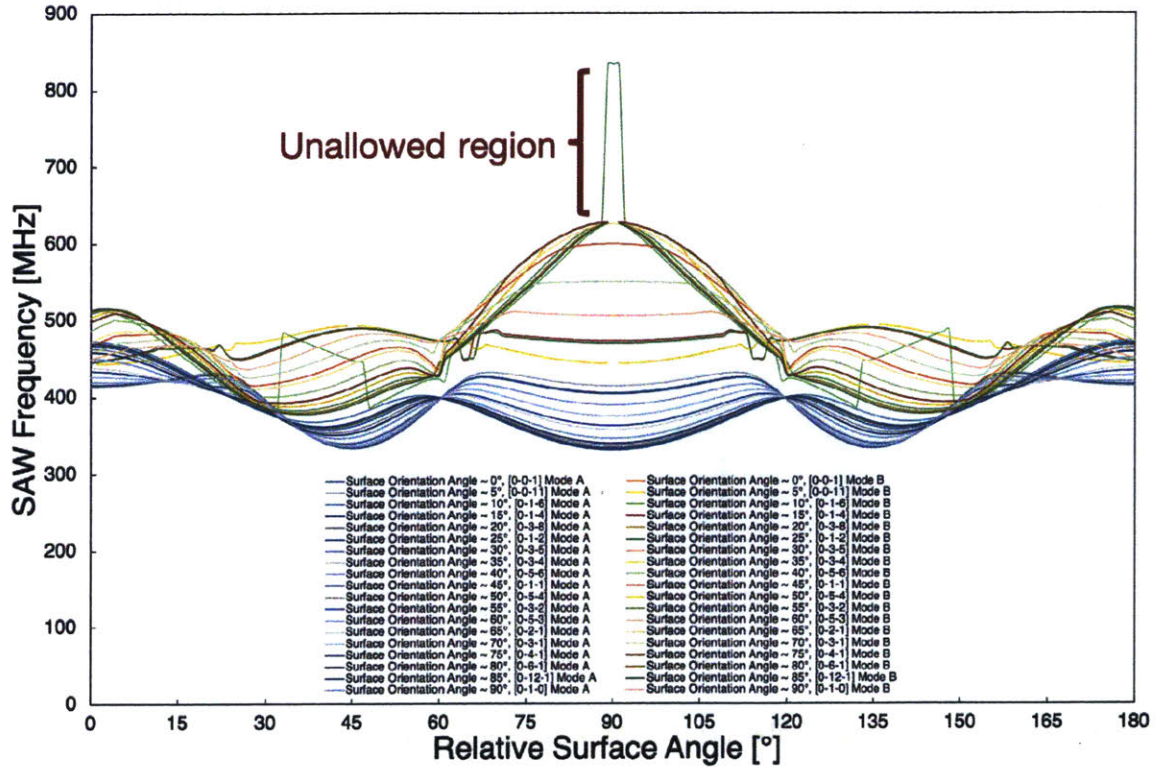
Figure 5-7: Predicted acoustic frequencies for a polarization range from 0 to $\frac{\pi}{2}$ radians ([0 0 1] to [0 1 0]) due to random crystal orientation by mode (as a function of relative surface angle) for pristine (unaged) cast austenitic stainless steel. Here, delta functions corresponding to PSAW and bulk modes were removed from Figure 4-18 since the probability of measuring each of these modes independently is zero. Monochromatic lines all correspond to Mode A across polarization range (SAWs only, delta function PSAWs of Mode A were removed from Fig. 4-18) and colored lines correspond to Mode B across polarization range (PSAWs or continuous, non-delta function bulk waves), according to the convention in Table 4.1

appear more frequently in degraded CASS in comparison to control, with a p-value of 0.04. Furthermore, a similar χ^2-test also leads to the same conclusion with a p-value of 0.08. The counts and statistical tests are summarized in Tables 5.1 and 5.2. These results show that the number of SAW peak splits significantly appears more frequently in degraded alloys. Thus, taken in combination with the t-test results in 5.2.2 shown in Fig. 5-4, which show that that the spread of frequencies is also significantly different in degraded CASS in comparison to controls, we are led to reject the null hypothesis that solely attributes SAW peak splitting to the elastodynamic variation predicted due to random crystal orientation.

98
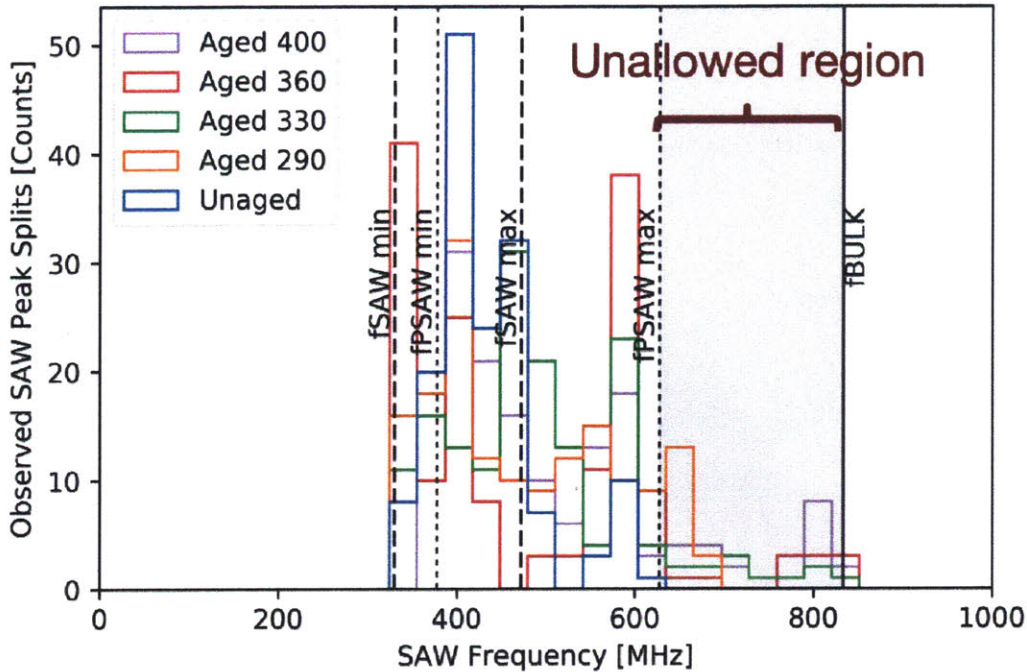
Figure 5-8: Distribution of observed SAW frequencies show the emergence of a statistically significant, second Fourier frequency outside the range of predicted frequencies due to random crystal orientation. Shaded region indicates the unallowable range of frequencies due to random crystal orientation, $f_{SAW,min}$ and $f_{SAW,max}$ indicate the expected variation from measuring SAW frequencies of crystals oriented differently, $f_{PSAW,min}$ and $f_{PSAW,max}$ indicate the expected variation from measuring PSAW frequencies of crystals oriented differently, and f_{BULK} indicates the allowable fast bulk mode–as predicted by elastic theory. This figure was conceived with support from Steve Jepeal through the MIT NSE Communication Lab.

This conclusion implies that variation due to random crystal orientation can explain SAW peak splitting in unaged samples but cannot account for all SAW peak splits in degraded, thermally aged alloys. Thus, we can conclude by (1) attributing peak splitting in the allowable range of frequencies predicted by elastodynamic theory to random crystal orientation, and (2) attributing peak splitting in the unallowed range of frequencies predicted by elastodynamic theory to microstructural degradation. Therefore, we deterministically and statistically conclude that microstructural degradation in CASS alloys can reliably be detected via TGS in a predictive, rapid, non-contact, and non-destructive manner by probing for SAW peak splitting.

	Unaged	Aged
N Peak Splits	13	277
Total TGS Spots Scanned	80	320
Fraction of Peak Splits Observed	0.1625	0.8656

Table 5.1: Counts of SAW peak splits observed in unaged versus aged samples show a statistically significant difference in frequency of occurrence, supporting that SAW peak splitting cannot be explained with elastodynamic theory due to random crystal orientation without accounting for microstructural degradation (i.e. the growth of new phases).

	Score	P-Value
Z-Score Statistics	1.744	0.04
Chi-Squared Statistics	3.042	0.08

Table 5.2: Results of statistical tests performed on the fraction of SAW peak splits observed in unaged versus aged samples show a statistically significant difference between both sets of specimens.

5.4 Summary of Discussion

The disadvantages of using TGS to detect spinodal decompositon include needing a well polished surface to maximize signal to noise ration and minimize scattering that may ambiguate the generation of SAWs (as an elastic response to TGS illumination). Since the signal is inversely proportional to noise in frequency $S \propto \frac{1}{f}$, phases with higher stiffness (and, thus, higher frequency due to less attenuation) are harder to detect due to stochastic nature associated with the phenomenon of spectral density, especially when multiple phases and varying crystal orientations are present. Furthermore, phases with similar elastic properties are more difficult to deconvolve since their signature in frequency space would overlap and appear as a single peak in the fourier spectra calculated from the raw TGS signal. For example, the unaged CASS in this study include two phases (ferrite and austenite), however, TGS measurements result in only one SAW frequency due to their roughly equal mechanical and elastic properties (hardness and elastic moduli)—as shown in Tab. 4.2. Another key limitation specific to the study of polycrystalline materials using TGS is the difficulty in differentiating between multiple phases with different elastic properties and the same phase (with similar elastic properties) in varying crystal orientations. The im-

100

plication is that it is challenging to pinpoint the origin of peaks when degradation is present, especially when that degradation could potentially change the crystal orientation (e.g. as is the case with increased favorability of G-phase precipitation across dislocations). Although, in the case of CASS, it is unlikely that G-phase can impact the TGS signal due to scattering caused by the discrete, small particle size (generation of SAWs require a continuuum). Even when the particles grow larger and may effect crystal orientation, it is likely that the neighboring grain orientations change only by a couple to a few degrees at most. As shown in Figure 5-7, a few degrees in relative surface angle would only change SAW frequencies, measured by TGS, in infinitesimal increments due to the wave continuum governed by elastodynamic theory in the random crystal orientation model.

The advantages of using TGS to detect spinodal decomposition is mainly involve the fact that the measurement of a frequency in the unallowed region shown in Figures 5-7 and 5-8 directly imply that the material has undergone spinodal decomposition for the case of CASS. Similar, more general conclusions can be drawn for any material exhibiting SAW peaks in elastically unallowed frequencies, indicating that microstructural change has occurred.

Based on the results of this thesis, spinodal decomposition can be detected using TGS if the spinodal regions fall within the area illuminated by the pump and probe beams. In general, this approach can be applied to detect spinodal decomposition if the length scale/area of the spinodal regions (phases grown due to spinodal decomposition) are large enough to be captured within the TGS spot size. Furthermore, by tuning the optics in the TGS apparatus, the spot size can be engineered to match the size of the spinodal region as characterized by TEM.

Other problems with TGS include the sensitivity to crystal orientation, i.e. the grain size dependence of the TGS signal. Although the predictability of TGS measurements are advantageous in the case of well-defined crystal systems, however, are increasingly more difficult for complex crystal systems such as composite alloys. In general, predictability requires known elastic constants, and measuring elastic constants require known crystal orientation. This is a problem because elastic constants,

particularly at elevated temperatures, are surprisingly scarce in literature. However, there are arduous methods to measure elastic constants, for example, by mapping TGS measurements on specific spots illuminated by TGS to crystal orientations elucidated by electron backscatter diffraction (EBSD). This way, back-calculating the elastic constant from the general solution of normal modes to equation 3.4, as derived in section 3.4.1, can be performed by fitting this data to the crystal orientation model (used in this study), adjusted by the suitable material paraemeters, in reverse.

Ultimately, these findings suggest that the growth of new phases due to microstructural degradation, most likely due to spinodal decomposition, can be non-destructively detected at a distance using TGS. However, it remains unclear whether SAW peak splitting can be attributed entirely to spinodal decomposition due to the presence of other forms of degradation, such as G-phase and carbide/nitride precipitation, which may also contribute to the TGS signal due to their effect on the crystal orientation. In-situ TGS studies can be done by annealing out spinodal decomposition at temperatures beyond the spinodal region ($\geq 450°C$) in the Fe-Cr phase diagram to address this question further. Higher aging times of 30,000 hours at higher temperatures have shown a stronger correlation with thermal hardening from spinodal decomposition. Thus, this merits further ex-situ TGS measurements to be performed on CASS alloys aged for 50,000 hours and 100,000 hours to establish the correlations between SAW frequencies measured via TGS to lowered ductility from Charpy testing and decreased toughness from indentation testing to consolidate these trends moving forward.

Chapter 6

Conclusion

We have shown that non-contact, non-destructive gigahertz ultrasonic techniques such as TGS may be used to detect microstructural degradation in key LWR materials. CASS was taken as an example for its wide usage across LWR systems and the costly risks of spinodal decomposition in these materials throughout the lifetime of the reactor. We demonstrated a link between observed surface acoustic wave (SAW) peak splitting in TGS and direct evidence of spinodal decomposition in the same specimens, backed up by hardness measurements which agree with previous studies. This motivates the usage of this and other rapid NDE techniques to extend to other material systems in LWRs, particularly to reactor pressure vessel steel.

6.1 Contributions

The author's contributions in this thesis are the following:

- Specimen preparation, including material matrix selection, low-speed cutting and polishing after Charpy impact testing

- Coordinating microstructural characterization experiments with collaborators as well as interpreting and linking results to achieve the primary objectives of the thesis

- Mechanical testing via micro and nanoindentation, including data analysis using BIC and generating trends for TGS correlations

- Photoacoustic testing using TGS set-up in air and in vacuum on all CASS specimens investigated in this study, including TGS phase analysis, FFTs, as well as peak fits and counts

- Based on a probabilistic approach, performing statistical testing on results to disprove the null hypothesis and assign a probabilistic value on the likelihood of the emergence of the second peak due to microstructural degradation

- Implementing deterministic model to predict SAW frequencies that explain results from TGS measurements as well as interpreting results to establish a methodology for ex situ detection of microstructural degradation

6.2   Future Work

The ability to link a new parameter, SAW peak splitting, directly to combined spinodal decomposition and G phase precipitation represents a potentially powerful new tool for LWR materials degradation management. Replacing such components can cost up to hundreds of millions of dollars, when accounting for both the component and the outage time, thus quickly gaining more information about whether and when to replace such a large component can be a make-or-break economic decision for aging LWRs. Even gaining a year of extra usage before a required replacement represents a serious economic benefit, especially today when LWRs are struggling to keep up with cheap natural gas and oversubsidized wind and solar power.

In future studies on CASS materials, by supporting such molecular dynamic-based models with experimental data, time-evolution of radiation damage modes in LWR structural materials can be projected using the mechanistic understanding of degradation processes revealed by TGS.

This study both motivates further, direct investigation into the robustness of this measurement mechanism on CASS, as well as where else such NDE techniques could

be useful in directly assessing material health. For example, the formation of copper nanoprecipitates is one of the principal embrittling mechanisms increasing the DBTT of reactor pressure vessel (RPV) steels [112, 113]. Should a technique like TGS be able to tie changes in signal to the extent of Cu precipitation or any other solute, they could be used to gauge RPV health. The potential gains for RPVs are even more amplified compared to CASS components, as the vessel *is* the reactor from a licensing point of view.

Bibliography

[1] United States Nuclear Regulatory Commission (US NRC). 50.65 requirements for monitoring the effectiveness of maintenance at nuclear power plants. *NRC Library*, April 2017. Available at https://www.nrc.gov/reading-rm/doc-collections/cfr/part050/part050-0065.html.

[2] P. L. Andresen, F. P. Ford, K. Gott, R. L. Jones, P. M. Scott, T. Shoji, R. W. Staehle, and R. L. Tapping. Expert panel report on proactive materials degradation assessment (nureg/cr-6923). *US NRC*, 2007.

[3] T. R. Allen, R. E. Stoller, and S. Yamanaka. *Comprehensive Nuclear Materials*. Elsevier, 2012.

[4] M. D. Mathew, L. M. Lietzan, K. L. Murty, and V. N. Shah. Low temperature aging embrittlement of cf-8 stainless steel. *Materials Science and Engineering: A*, 269(1):186 – 196, 1999.

[5] M. K. Miller and J. Bentley. Apfim and aem investigation of cf8 and cf8m primary coolant pipe steels. *Mater. Sci. Technol.*, 6(3):285–292, 1990.

[6] C. A. Dennett, P. Cao, S. E. Ferry, A. Vega-Flick, A. A. Maznev, K. A. Nelson, A. G. Every, and M. P. Short. Bridging the gap to mesoscale radiation materials science with transient grating spectroscopy. *Phys. Rev. B*, 94(21):214106, 2016.

[7] GS Was, Z Jiao, E Getto, K Sun, AM Monterrosa, SA Maloy, O Anderoglu, BH Sencer, and M Hackett. Emulation of reactor irradiation damage using ion beams. *Scripta Materialia*, 88:33–36, 2014.

[8] Michael P Short, Cody A Dennett, Sara E Ferry, Yang Yang, Vikash K Mishra, Jeffrey K Eliason, Alejandro Vega-Flick, Alexei A Maznev, and Keith A Nelson. Applications of transient grating spectroscopy to radiation materials science. *JOM*, 67(8):1840–1848, 2015.

[9] RA Duncan, F Hofmann, A Vega-Flick, JK Eliason, AA Maznev, AG Every, and KA Nelson. Increase in elastic anisotropy of single crystal tungsten upon he-ion implantation measured with laser-generated surface acoustic waves. *Applied Physics Letters*, 109(15):151906, 2016.

[10] C. A. Dennett and M. P. Short. Time-resolved, dual heterodyne phase collection transient grating spectroscopy. *Appl. Phys. Lett.*, 110(21):211106, 2017.

[11] Xinpeng Du and Ji-Cheng Zhao. Facile measurement of single-crystal elastic constants from polycrystalline samples. *NPJ Computational Materials*, 3(1):17, 2017.

[12] CA Dennett, KP So, A Kushima, DL Buller, K Hattar, and MP Short. Detecting self-ion irradiation-induced void swelling in pure copper using transient grating spectroscopy. *Acta Materialia*, 145:496–503, 2018.

[13] Cody A Dennett and Michael P Short. Thermal diffusivity determination using heterodyne phase insensitive transient grating spectroscopy. *Journal of Applied Physics*, 123(21):215109, 2018.

[14] Felix Hofmann, Michael P Short, and Cody A Dennett. Transient grating spectroscopy: An ultrarapid, nondestructive materials evaluation technique. *MRS Bulletin*, 44(5):392–402, 2019.

[15] Cody A Dennett, Daniel L Buller, Khalid Hattar, and Michael P Short. Real-time thermomechanical property monitoring during ion beam irradiation using in situ transient grating spectroscopy. *Nuclear Instruments and Methods in Physics Research Section B: Beam Interactions with Materials and Atoms*, 440:126–138, 2019.

[16] Sara E Ferry, Cody A Dennett, Kevin B Woller, and Michael P Short. Inferring radiation-induced microstructural evolution in single-crystal niobium through changes in thermal transport. *Journal of Nuclear Materials*, 2019.

[17] Olivier Cometto, Cody A Dennett, Siu Hon Tsang, Michael P Short, and Edwin HT Teo. A thermal study of amorphous and textured carbon and carbon nitride thin films via transient grating spectroscopy. *Carbon*, 130:355–361, 2018.

[18] Cody A Dennett, Penghui Cao, Sara E Ferry, and Michael P Short. Developing continuous non-contact thermomechanical property monitoring for ion irradiations using surface photoacoustics. Technical report, Sandia National Lab.(SNL-NM), Albuquerque, NM (United States), 2016.

[19] Saleem A. Al Dajani et al. Non-destructively detecting lwr structural material embrittlement using transient grating spectroscopy. In *Proceedings of the 19th International Conference on Environmental Degradation of Materials in Nuclear Power Systems–Water Reactors*, 2019.

[20] Robin Dyle. Materials degradation matrix and issue management tables overview-lto update. In *Second Workshop on US Nuclear Power Plant Live Extension, Washington, DC*, 2011.

[21] Omesh K Chopra and Appajosula S Rao. *Effect of Thermal Aging and Neutron Irradiation on Crack Growth Rate and Fracture Toughness of Cast Stainless Steels and Austenitic Stainless Steel Welds*. US Nuclear Regulatory Commission, Office of Nuclear Regulatory Research, 2015.

[22] OK Chopra and A Sather. Initial assessment of the mechanisms and significance of low-temperature embrittlement of cast stainless steels in lwr systems. Technical report, Nuclear Regulatory Commission, 1990.

[23] Omesh K Chopra. Estimation of fracture toughness of cast stainless steels during thermal aging in lwr systems. Technical report, Nuclear Regulatory Commission, Washington, DC (USA). Div. of Engineering, 1991.

[24] WF Michaud, PT Toben, WK Soppet, and OK Chopra. Tensile-property characterization of thermally aged cast stainless steels. Technical report, Nuclear Regulatory Commission, Washington, DC (United States). Div. of Engineering, 1994.

[25] HM Chung and TR Leax. Embrittlement of laboratory and reactor aged cf3, cf8, and cf8m duplex stainless steels. *Materials Science and Technology*, 6(3):249–262, 1990.

[26] HM Chung. Evaluation of aging of cast stainless steel components. Technical report, Argonne National Lab, 1991. No. ANL/CP-70872.

[27] TS Byun and JT Busby. Cast stainless steel aging research plan. *ORNL/LTR-2012/440*, 2012.

[28] ASTM A743/A743M-13. Standard specification for castings, iron-chromium, iron-chromium-nickel, corrosionresistant, for general application. Technical report.

[29] ASTM A744/A744M-13. Specification for castings, ironchromium-nickel, corrosion resistant, for severe service. Technical report.

[30] ASTM A351/A351M-14. Standard specification for castings, austenitic, for pressure-containing parts,. Technical report.

[31] Thak Sang Byun, Timothy G Lach, Ying Yang, and Changheui Jang. Influence of δ-ferrite content on thermal aging induced mechanical property degradation in cast stainless steels. In *Proceedings of the 18th International Conference on Environmental Degradation of Materials in Nuclear Power Systems–Water Reactors*, pages 1829–1840. Springer, 2019.

[32] Timothy G Lach and Thak Sang Byun. Microstructural evolution of cast austenitic stainless steels under accelerated thermal aging. In *Environmental Degradation of Materials in Nuclear Power Systems*, pages 643–652. Springer, 2017.

[33] BI Voronenko. Austenitic-ferritic stainless steels: A state-of-the-art review. *Metal Science and Heat Treatment*, 39(10):428–437, 1997.

[34] T. S. Byun, Y. Yang, N. R. Overman, and J. T. Busby. Thermal aging phenomena in cast duplex stainless steels. *JOM*, 68(2):507–516, Feb 2016.

[35] S. J. Zinkle and J. T. Busby. Structural materials for fission fusion energy. *Mater. Today*, 12(11):12 – 19, 2009. Figure adapted from Roger Staehle, Beaune Workshop 2008.

[36] O. K. Chopra and H. M. Chung. Embrittlement of cast stainless steels in lwr systems. Technical report, Argonne National Lab., 1989.

[37] O. K. Chopra. Long-term embrittlement of cast duplex stainless steels in lwr systems. semiannual report, october 1991–march 1992: Volume 7, no. 1. Technical report, Nuclear Regulatory Commission, Washington, DC (United States)., 1993.

[38] F Danoix, P Auger, and D Blavette. Hardening of aged duplex stainless steels by spinodal decomposition. *Microscopy and Microanalysis*, 10(3):349–354, 2004.

[39] O.K. Chopra. Effects of thermal aging and neutron irradiation on crack growth rate and fracture toughness of cast stainless steels and austenitic stainless steel welds. (NUREG/CR-7185, 2014).

[40] O.K. Chopra and A. Sather. Initial assessment of the mechanisms and significance of low-temperature embrittlement of cast stainless steels in lwr systems. (NUREG/CRâ5385, 1990).

[41] O.K. Chopra. Estimation of fracture toughness of cast stainless steels during thermal aging in lwr systems. (NUREG/CR-4513, 1991).

[42] W.K. Soppet W.F. Michaud, P.T. Toben and O.K. Chopra. Tensile-property characterization of thermally aged cast stainless steels. (NUREG/CR-6142, 1994).

[43] H.M. Chung and T.R. Leax. *Mater. Sci. Technol.* 6, 249 (1990).

[44] H.M. Chung. Evaluation of aging of cast stainless steel components. (Presented at ASME Pressure Vessel Piping Conference, San Diego, CA, 1991).

[45] T.S. Byun and J.T. Busby. Cast stainless steel aging research plan. (ORNL/LTR-2012/440, 2012).

[46] H.M. Chung. Cast stainless steel aging research plan.

[47] T. S. Byun, T. G. Lach, D. A. Collins, E. L. Barkley, and F. Yu. Mechanical and microstructural characteristics of cast stainless steels after thermal aging for 10000 hours. Technical report, Department of Energy/Office of Nuclear Energy, 2017. Available at https://lwrs.inl.gov/Materials%20Aging%20and%20Degradation/ Mechanical_and_Microstructural_Characteristics_of_Cast_Stainless_Steels_ after_Thermal_Aging_for_10000_Hours.pdf.

110

[48] T. G. Lach and T. S. Byun. Microstructural evolution of cast austenitic stainless steels under accelerated thermal aging. In J. H. Jackson, D. Paraventi, and M. Wright, editors, *Proc. 18th Intl. Conf. Env. Deg. Mater.*, pages 1859–1868, Cham, 2019. Springer International Publishing.

[49] OK Chopra et al. Estimation of fracture toughness of cast stainless steels during thermal aging in lwr systems-revison 1. Technical report, Argonne National Lab.(ANL), Argonne, IL (United States), 1994.

[50] Y Chen, B Alexandreanu, and Krishnamurti Natesan. Crack growth rate and fracture toughness tests on irradiated cast stainless steels. Technical report, Argonne National Lab.(ANL), Argonne, IL (United States), 2013.

[51] OK Chopra and WJ Shack. Crack growth rates and fracture toughness of irradiated austenitic stainless steels in bwr environments. Technical report, Argonne National Lab.(ANL), Argonne, IL (United States), 2008.

[52] OK Chopra. *Degradation of LWR core internal materials due to neutron irradiation*. US Nuclear Regulatory Commission, Office of Nuclear Regulatory Research, 2010.

[53] OK Chopra and AS Rao. A review of irradiation effects on lwr core internal materials–neutron embrittlement. *Journal of Nuclear Materials*, 412(1):195–208, 2011.

[54] S. L. Li, Y. L. Wang, S. X. Li, and X. T. Wang. Effect of long term aging on the microstructure and mechanical properties of cast austenitic stainless steels. *Acta Metall. Sin.*, 46(10):1186, 2010.

[55] S. L. Li, Y. L. Wang, H. Wang, C. S. Xin, and X. T. Wang. Effects of long-term thermal aging on the stress corrosion cracking behavior of cast austenitic stainless steels in simulated pwr primary water. *J. Nucl. Mater.*, 469:262 – 268, 2016.

[56] O. K. Chopra. Prediction of aging degradation of cast stainless steel components in lwr systems. Technical report, Argonne National Lab., IL (United States), 1992. No. ANL/CP-75791; CONF-920375-24.

[57] G. A. Qian and M. Niffenegger. Deterministic and probabilistic analysis of a reactor pressure vessel subjected to pressurized thermal shocks. *Nucl. Eng. Des.*, 273:381 – 395, 2014.

[58] Y. Chen, B. Alexandreanu, W.-Y. Chen, K. Natesan, Z. Li, Y. Yang, and A. S. Rao. Cracking behavior of thermally aged and irradiated cf-8 cast austenitic stainless steel. *J. Nucl. Mater.*, 466:560 – 568, 2015.

[59] Fréderic Danoix, Jacques Lacaze, A Gibert, Dominique Mangelinck, Khalid Hoummada, and Eric Andrieu. Effect of external stress on the fe–cr phase

separation in 15-5 ph and fe–15cr–5ni alloys. *Ultramicroscopy*, 132:193–198, 2013.

[60] SL Li, YL Wang, HL Zhang, SX Li, K Zheng, F Xue, and XT Wang. Microstructure evolution and impact fracture behaviors of z3cn20-09m stainless steels after long-term thermal aging. *Journal of Nuclear Materials*, 433(1-3):41–49, 2013.

[61] M Murayama, K Hono, and Y Katayama. Microstructural evolution in a 17-4 ph stainless steel after aging at 400 c. *Metallurgical and Materials Transactions A*, 30(2):345–353, 1999.

[62] Thomas Sourmail. Precipitation in creep resistant austenitic stainless steels. *Materials science and technology*, 17(1):1–14, 2001.

[63] LP Stoter. Thermal ageing effects in aisi type 316 stainless steel. *Journal of materials science*, 16(4):1039–1051, 1981.

[64] BF Weiss and R Stickler. Phase instabilities during high temperature exposure of 316 austenitic stainless steel. *Metallurgical and Materials Transactions B*, 3(4):851–866, 1972.

[65] JE Spruiell, JA Scott, CS Ary, and RL Hardin. Microstructural stability of thermal-mechanically pretreated type 316 austenitic stainless steel. *Metallurgical transactions*, 4(6):1533–1544, 1973.

[66] J. Charles. *Proceedings of Duplex Stainless Steel Conference, Vol 1 (Les Editions de Physique, Les Ulis Cedex, 1991) pp. 3-48*, 1991.

[67] John W Cahn. On spinodal decomposition. *Acta Metallurgica*, 9(9):795–801, 1961.

[68] Martin Bazant. Nucleation and spinodal decomposition, 2011.

[69] John W Cahn. On spinodal decomposition in cubic crystals. *Acta Metallurgica*, 10(3):179–183, 1962.

[70] John W Cahn. Phase separation by spinodal decomposition in isotropic systems. *The Journal of Chemical Physics*, 42(1):93–99, 1965.

[71] S. L. Li, Y. L. Wang, H. L. Zhang, S. X. Li, K. Zheng, F. Xue, and X. T. Wang. Microstructure evolution and impact fracture behaviors of z3cn20-09m stainless steels after long-term thermal aging. *J. Nucl. Mater.*, 433(1):41 – 49, 2013.

[72] H. M. Chung and O. K. Chopra. Microstructures of cast-duplex stainless steel after long-term aging. Technical report, Argonne National Lab., IL (USA), 1985.

[73] J. E. Brown, A. Cerezo, T. J. Godfrey, M. G. Hetherington, and G. D. W. Smith. Quantitative atom probe analysis of spinodal reaction in ferrite phase of duplex stainless steel. *Mater. Sci. Technol.*, 6(3):293–300, 1990.

[74] P. Auger, F. Danoix, A. Menand, S. Bonnet, J. Bourgoin, and M. Guttmann. Atom probe and transmission electron microscopy study of aging of cast duplex stainless steels. *Mater. Sci. Technol.*, 6(3):301–313, 1990.

[75] Yuichi Ishikawa and Toshihiko Yoshimura. Electrochemical and atom probe studies of cast and aged duplex stainless steel. *Materials Transactions, JIM*, 35(12):895–901, 1994.

[76] S. Kawaguchi, N. Sakamoto, G. Takano, F. Matsuda, Y. Kikuchi, and L. Mráz. Microstructural changes and fracture behavior of cf8m duplex stainless steels after long-term aging. *Nucl. Eng. Des.*, 174(3):273–285, 1997.

[77] J. J. Shiao, C. H. Tsai, J. J. Kai, and J. H. Huang. Aging embrittlement and lattice image analysis in a fe-cr-ni duplex stainless steel aged at 400 . *J. Nucl. Mater.*, 217(3):269–278, 1994.

[78] T. R. Leax, S. S. Brenner, and J. A. Spitznagel. Atom probe examination of thermally ages cf8m cast stainless steel. *Metall. Trans. A*, 23(10):2725–2736, 1992.

[79] Donghee Park, Peter A Mouche, Weicheng Zhong, Kiran K Mandapaka, Gary S Was, and Brent J Heuser. Tem/stem study of zircaloy-2 with protective feal (cr) layers under simulated bwr environment and high-temperature steam exposure. *Journal of Nuclear Materials*, 502:95–105, 2018.

[80] Takaaki Koyanagi and Yutai Katoh. Pie of nuclear-grade sic/sic flexural coupons irradiated to 10 dpa at lwr temperature. Technical report, Oak Ridge National Lab.(ORNL), Oak Ridge, TN (United States). High Flux â, 2017.

[81] MK Miller and MG Hetherington. Morphology and scaling behavior of ultrafine isotropic microstructures in fe-cr alloys from atom probe field ion microscopy data. *Scripta Metallurgica et Materialia*, 24(7):1375–1380, 1990.

[82] J Szilard. Ultrasonic testing: Non-conventional testing techniques. *John Wiley & Sons, Inc., 605 Third Ave., New York, NY 10158, 1982, 640*, 1982.

[83] RB Schwarz and JF Vuorinen. Resonant ultrasound spectroscopy: applications, current status and limitations. *Journal of Alloys and Compounds*, 310(1-2):243–250, 2000.

[84] Malcolm R Howells, Tobias Beetz, Henry N Chapman, C Cui, JM Holton, CJ Jacobsen, J Kirz, Enju Lima, Stefano Marchesini, Huijie Miao, et al. An assessment of the resolution limitation due to radiation-damage in x-ray diffraction microscopy. *Journal of electron spectroscopy and related phenomena*, 170(1-3):4–12, 2009.

[85] S Joneliunas, L Pranevichius, and R Valatka. Surface acoustic waves in the study of ion implanted surface layers. *Nuclear Instruments and Methods*, 182:761–767, 1981.

[86] LW Kessler and DE Yuhas. Principles and analytical capabilities of the scanning laser acoustic microscope (slam). *Scanning Electron Microscopy*, 1:555, 1978.

[87] AC Wey and LW Kessler. Holographic scanning laser acoustic microscopy (holoslam): A new qnde tool. In *Review of Progress in Quantitative Non-destructive Evaluation*, pages 975–982. Springer, 1990.

[88] BT Khuri-Yakub. Scanning acoustic microscopy. *Ultrasonics*, 31(5):361–372, 1993.

[89] J Zuk, H Kiefte, and MJ Clouter. Investigation of ion-implanted gap layers by brillouin scattering. *Journal of applied physics*, 73(10):4951–4954, 1993.

[90] W Bras, GE Derbyshire, AJ Ryan, GR Mant, A Felton, RA Lewis, CJ Hall, and GN Greaves. Simultaneous time resolved saxs and waxs experiments using synchrotron radiation. *Nuclear Instruments and Methods in Physics Research Section A: Accelerators, Spectrometers, Detectors and Associated Equipment*, 326(3):587–591, 1993.

[91] Vandana Rathore. Positron annihilation spectroscopy: A review of applications in nanomaterials thin films and semiconductors.

[92] AG Every. Measurement of the near-surface elastic properties of solids and thin supported films. *Measurement Science and Technology*, 13(5):R21, 2002.

[93] M Szabadi, P Hess, AJ Kellock, H Coufal, and JEE Baglin. Elastic and mechanical properties of ion-implanted silicon determined by surface-acoustic-wave spectrometry. *Physical Review B*, 58(14):8941, 1998.

[94] F Hofmann, D Nguyen-Manh, MR Gilbert, CE Beck, JK Eliason, AA Maznev, W Liu, DEJ Armstrong, KA Nelson, and SL Dudarev. Lattice swelling and modulus change in a helium-implanted tungsten alloy: X-ray micro-diffraction, surface acoustic wave measurements, and multiscale modelling. *Acta Materialia*, 89:352–363, 2015.

[95] Jozefien Goossens, Philippe Leclaire, Xiaodong Xu, Christ Glorieux, Loic Martinez, Antonella Sola, Cristina Siligardi, Valeria Cannillo, Tom Van der Donck, and Jean-Pierre Celis. Surface acoustic wave depth profiling of a functionally graded material. *Journal of Applied Physics*, 102(5):053508, 2007.

[96] Naohiro Igata, Yutaka Kohno, and Jun-ichi Nishimura. Dislocation behavior in the swelling process of hvem irradiated stainless steel. In *Radiation-Induced Changes in Microstructure: 13th International Symposium (Part I)*. ASTM International, 1987.

[97] Mychailo B Toloczko, FA Garner, VN Voyevodin, VV Bryk, OV Borodin, VV Mel'Nychenko, and AS Kalchenko. Ion-induced swelling of ods ferritic alloy ma957 tubing to 500 dpa. *Journal of Nuclear Materials*, 453(1-3):323–333, 2014.

[98] Cody A. Dennett Michael P. Short. Private communication, 2019.

[99] Warren Carl Oliver and George Mathews Pharr. An improved technique for determining hardness and elastic modulus using load and displacement sensing indentation experiments. *Journal of materials research*, 7(6):1564–1583, 1992.

[100] Caitlin Huotilainen, Mykola Ivanchenko, Ulla Ehrnstén, and Pål Efsing. Electrochemical investigation of in-service thermal aging in two cf8m cast stainless steels. *Journal of Nuclear Materials*, 520:34–40, 2019.

[101] Geoffrey McLachlan and David Peel. *Finite mixture models*. John Wiley & Sons, 2004.

[102] Gideon Schwarz et al. Estimating the dimension of a model. *The annals of statistics*, 6(2):461–464, 1978.

[103] Konrad J Krakowiak, William Wilson, Simon James, Simone Musso, and Franz-Josef Ulm. Inference of the phase-to-mechanical property link via coupled x-ray spectrometry and indentation analysis: Application to cement-based materials. *Cement and Concrete Research*, 67:271–285, 2015.

[104] HM Ledbetter. Predicted monocrystal elastic constants of 304-type stainless steel. *Physica B+ C*, 128(1):1–4, 1985.

[105] Kamel Benyelloul and Hafid Aourag. Elastic constants of austenitic stainless steel: Investigation by the first-principles calculations and the artificial neural network approach. *Computational Materials Science*, 67:353–358, 2013.

[106] HM Ledbetter. Monocrystal-polycrystal elastic constants of a stainless steel. *Physica Status Solidi (a)*, 85(1):89–96, 1984.

[107] AbdulFattah A Al-Dajani. *Seismic reflection moveout for azimuthally anisotropic media*. PhD thesis, Massachusetts Institute of Technology, 2002.

[108] Yong-Sheng Li, Shu-Xiao Li, and Tong-Yi Zhang. Effect of dislocations on spinodal decomposition in fe–cr alloys. *Journal of nuclear materials*, 395(1-3):120–130, 2009.

[109] Arpan Das and Chandra Bhanu Basak. Fracture mechanisms of spinodal alloys. *Philosophical Magazine*, 98(33):3007–3033, 2018.

[110] Cem Örnek, MG Burke, T Hashimoto, and DL Engelberg. 748 k (475 c) embrittlement of duplex stainless steel: effect on microstructure and fracture behavior. *Metallurgical and Materials Transactions A*, 48(4):1653–1665, 2017.

[111] Yasufumi Miura and Masato Yamamoto. Effect of aging temperature on fracture toughness of cast austenitic stainless steel. In *ASME 2015 Pressure Vessels and Piping Conference*. American Society of Mechanical Engineers Digital Collection, 2015.

[112] Y. Nagai, T. Toyama, Y. Nishiyama, M. Suzuki, Z. Tang, and M. Hasegawa. Kinetics of irradiation-induced cu precipitation in nuclear reactor pressure vessel steels. *Appl. Phys. Lett.*, 87(26):261920, 2005.

[113] D. J. Sprouster, J. Sinsheimer, E. Dooryhee, S. K. Ghose, P. Wells, T. Stan, N. Almirall, G. R. Odette, and L. E. Ecker. Structural characterization of nanoscale intermetallic precipitates in highly neutron irradiated reactor pressure vessel steels. *Scripta Mater.*, 113:18–22, 2016.